UNIVERSITÀ DEGLI STUDI DI TRIESTE

XXXII CICLO DEL DOTTORATO DI RICERCA IN
NANOTECNOLOGIE

PO FRIULI VENEZIA GIULIA - FONDO SOCIALE EUROPEO 2014/2020

VO$_2$ A PROTOTYPICAL PHASE CHANGE MATERIAL: SPECTROSCOPIC STUDY OF THE ORBITAL CONTRIBUTION ACROSS THE METAL INSULATOR TRANSITION

Settore scientifico-disciplinare: **FIS/03**

DOTTORANDO
ALESSANDRO D'ELIA

COORDINATORE
PROF. ALBERTO MORGANTE

SUPERVISORE DI TESI
PROF. ALBERTO MORGANTE

CO-SUPERVISORE DI TESI
DR. MARCELLO CORENO

ANNO ACCADEMICO 2018/2019

“*If, in some cataclysm, all of scientific knowledge were to be destroyed, and only one sentence passed on to the next generation of creatures, what statement would contain the most information in the fewest words?* ***I believe it is the atomic hypothesis (or the atomic fact, or whatever you wish to call it) that all things are made of atoms - little particles that move around in perpetual motion, attracting each other when they are a little distance apart, but repelling upon being squeezed into one another. In that one sentence, you will see, there is an enormous amount of information about the world, if just a little imagination and thinking are applied.”***

R. Feynman

The Feynman Lectures on Physics (1964)

“Please remember the deadline of dd/mm/yy for submitting the quarterly report. Let me remind you that its submission is mandatory. Failing to do so, you will no longer be entitled to the funding and will have to return the scholarship received so far.”

Friendly deadline reminder

FSE secretariat

Index

Abstract

VO_2 is a fascinating $3d^1$ system undergoing a temperature triggered (67 °C) Metal Insulator Transition (MIT) coupled with a structural phase transition, from a low-temperature monoclinic insulator to a high-temperature tetragonal metal. Since its discovery, the MIT has been widely studied with a twofold interest: its applicative potential and its nature.

Different theoretical models have been proposed to explain the occurrence of the insulating phase of VO_2 like a structurally driven Peierls transition or a Mott-Hubbard transition triggered by electron mutual Coulomb repulsion. However, a clear theoretical picture is missing since VO_2 properties are determined by a complex interplay among lattice, orbital and electronic degrees of freedom. Therefore, in order to exploit the MIT features for technological application, a detailed study of the influence and interplay between the different degrees of freedom is of paramount importance.

With the aim of disentangling the lattice-orbital-electronic intrigue, in this thesis, four samples with different structural properties have been studied. Three thin strained films and one nanostructured disordered VO_2 film have been investigated using advanced spectroscopic techniques like X-ray absorption Near Edge Structure (XANES), Resonant Photoemission (ResPES) and Constant Initial State (CIS). The combination of these techniques allowed us to determine the strain influence over the multi-orbital contribution to the MIT. In addition, interesting features like the Fermi Level population can be modulated tuning the strain. In the disordered sample, in which the Peierls mechanism is quenched, it has been possible to observe the occurrence of a purely electronic transition, i.e. structural transition is not necessary to trigger the MIT.

Chapter 1.

Vanadium oxides and VO_2

In the last decades, technological advancements in the field of information processing, and storage have revolutionized our lifestyle. The advent of high performance computing, instantaneous worldwide range communication as well as fast storage of large dataset had irrevocably changed society. Computer assisted design of new products and simulations to predict functionalities, the ability to manage complex tasks like control of robotic manufacturing processes or handle supply chains on the global scale are just a few examples of the influence of the technology on our everyday life.

The key element of this technological advancement is silicon, which plays a major role in semiconductor-based electronics. The success of silicon is due to three main features: 1) its low cost and high abundance, 2) the modulation of flow of electrical charges applying an electric field, enabling storage, manipulation and amplification of electrical signals, 3) the conversion of optical into electric signal and vice versa.

The improvement of fabrication technologies led to the continuous miniaturization of silicon-based electronics and in particular of transistors in agreement with the Moore law[1]. The prediction to double the number of transistors per unit area every two years has been respected for at least 40 years, although a slow down has been observed since 2015 due to the increasing complexity of the miniaturization procedures and chips manufacturing costs[2].

The decreasing trend of the Moore law points out that the margin of the silicon based technologies improvement is vanishing, triggering the R&D of materials with novel properties and functionalities. In this framework, Transition Metal Oxides (TMO) are possible candidates. In ordinary semiconductors, the valence band is generated by the superposition of *s-p* orbitals while in TMO it is formed by *d* electrons, which provide new functional properties. Usually, in TMO there is a complex interplay between structural, orbital and electronic degrees of freedom, which give rise to unconventional and fascinating properties: the appearance of high-temperature superconductivity in complex cuprates[3] and the observation of giant magnetoresistance in manganites[4] are just few examples.

In contrast to middle and late TMOs, early TMOs are far less studied and in particular vanadium oxides disclose a huge applicative potential[5].

Vanadium ([Ar] $3d^3 4s^2$) is a very reactive element and different stoichiometric oxides (VO, V_2O_3, VO_2, and V_2O_5) characterized by different oxidation states such as V^{+2}, V^{+3}, V^{+4} and V^{+5} as well as mixed-valence oxides (Magneli and Wadsley series)[6] can be synthesized. This huge variety of oxides implies an equally large variety of structural and electronic properties, which can have different and powerful technological applications. As an example, because of their layered structure, both V_2O_5 and V_6O_{13} have been deeply investigated for possible applications as cathode materials in Li-ion batteries[7–9]. More importantly, this class of oxides bears the seed of a strong electronic correlation. VO_2, V_2O_3 and the mixed-valence V_nO_{2n-1} (n=3-6, 8, 9) systems all exhibit first-order metal-insulator transitions (MIT)[5,10].

One of the most studied oxides, the tetravalent oxide VO_2, undergoes a sharp, reversible, hysteretic, MIT coupled to a structural phase transition, passing from a high-temperature tetragonal metal to a low-temperature monoclinic insulator phase.

Vanadium dioxide MIT can be triggered by temperature (~67 °C in single crystals)[11], electric field[12] or photo-carrier doping[13], making VO_2 an extremely versatile and attractive prototype phase change material (PCM). The transition can be characterized in terms of amplitude (ΔA), width (ΔW), sharpness (ΔH) and critical temperature (T_c), which are dependent on the VO_2 structure at micro and nanoscale.

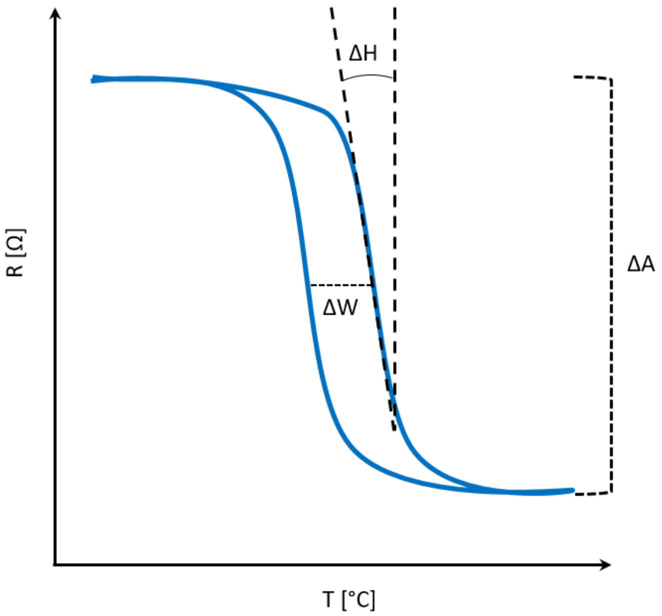

Figure 1.1: Qualitative representation of the hysteresis cycle of the resistance across the phase transition with the characteristics parameters that define the MIT features. ΔA is the amplitude of the transition, ΔW is the width and ΔH the sharpness or slope.

Narayan and Bhosle proposed a qualitative model based on the classical nucleation theory[14] which correlates ΔA, ΔW and ΔH (see Fig. 1.1) to samples microstructure being also able to rationalize results available in the literature[15–17]. They rely on the characterization of the phase transition in terms of the Gibbs free energy variation in adiabatic approximation:

$$\Delta G = \Delta T \Delta S \tag{1.1}$$

where ΔG, ΔT and ΔS are the variations of the free energy, the temperature and the entropy across the phase transition. According to the classical nucleation theory, the minimum radius necessary to an agglomerate to start the nucleation process (i.e., the critical radius) can be written as:

$$r_c = \frac{2\Omega}{\Delta G} \tag{1.2}$$

in which Ω is the interfacial energy. The main features of the Narayan-Bhosle semi-empirical model are listed in the following:

1. The sharpness of the transition ΔH is directly dependent on the defect density per unit of volume, including point defects, cluster impurities, and grain boundaries
   $$\Delta H = C\rho_d \tag{1.3}$$
   where C is a constant and ρ_d the density of defects. Usually, grain boundaries defects are not relevant respect to point defects, until the grain size decreases to the nanometer dimension. In this case, they will play a role in decreasing the sharpness of the transition[18].
2. ΔA is inversely proportional to defect density. High purity VO_2 exhibits a larger transition amplitude.

3. The finite temperature ΔT necessary for the phase transition is directly proportional to the hysteresis width ΔW. Therefore, a minimum hysteresis will always be present even in the purest sample.

$$\Delta W \propto \Delta T = \frac{2\Omega}{\Delta S r_c} \tag{1.4}$$

   Reducing the grain radius and increasing the interfacial energy, the hysteresis width increases. Therefore both sample morphology and dimension affect ΔW. Various studies on VO_2 nanoparticles clearly showed the increase of the transition width reducing the nanoparticle size[16,19,20]. The explanation of the ΔW dependence from the interfacial energy Ω can be found in grain boundaries. In synthesis, the interfacial energy is minimized when two adjacent grains are oriented within small angle respect to a fixed direction, hence the polycrystalline samples transition width is larger respect to single crystal[21].

Using this model is possible to predict the phase transition features for different complex morphologies. This is extremely important in order to synthesize VO_2 samples with the necessary properties to match the desired application. For example, for memory device applications a VO_2 sample with a large hysteresis is preferable, while for sensing applications, the highest efficiency is required and therefore a sharp phase transition with a large amplitude is preferred. In general, from the Narayan-Bhosle semi-empirical model some general trends can be extrapolated.

For high quality single crystals, i.e., big grains well oriented, the model predicts a sharp transition (small ΔH) with a large amplitude (ΔA) and a small width (small ΔW). Respect to single crystal, in randomly oriented polycrystalline films, the MIT will exhibit a smaller ΔA (because of the increased amount of defects) and a larger width caused by the mismatch of large grains orientation. In nanoparticles assembled films, the small grain size will contribute, in addition to the increase of the number of defects and to the random grain orientation, to the larger width and to smaller amplitude phase transition respect to polycrystalline films. In amorphous VO_2 samples, the phase transition is broad (large ΔH) because of the high concentration of defects while the amplitude is reduced. The width ΔW is also reduced because of the reduction of the grain boundaries[22,23]. In addition, epitaxial strain[24] and alloying[25] allow to increase or decrease the transition critical temperature

In this scenario, the VO_2 emerges as a prototypical PCM since its near room temperature phase transition is easily accessible and easy to manipulate. Consequently, different applications based on VO_2, MIT exploitation have been proposed in different technological areas.

In electronics, PCMs and in particular VO_2 have been proposed for neuromorphic computing[26,27], radiofrequency and electrical switches, augmented Field Effect Transistor (FET)[5] and coupled oscillators[28], though a physical model for the simulations of PCM based devices to calculate heat transport, Joule heating and MIT features has been addressed only recently[29]. The MIT in VO_2 can be controlled at the nanoscale using an atomic force microscope equipped with a biased conducting tip, suggesting applications in computing and memory devices[30].

VO_2 thin films, used as a window coating, have also been proposed as an energy-saving material with the ability to decrease the energy loss in buildings. Indeed, in the low-temperature insulating phase, VO_2 is almost transparent to infrared (IR) radiation. Rising the temperature, in the metallic phase, it is a highly IR reflecting material[31]. Lowering the MIT temperature upon

W doping [31], it is possible to use VO_2 coatings to modulate the infrared component of the radiation entering or leaving a building, therefore, controlling its thermal isolation.

Despite the attention received for its possible applications, since the first observation of the VO_2 phase transformation by Morin in 1959[11], the very nature of the MIT has been the argument of intense scientific debate. The abrupt jump in resistivity is accompanied at the same temperature by a crystalline transition, going from the low-temperature monoclinic phase to the high-temperature rutile structure. Different models have been proposed to explain the VO_2 Metal to Insulator Transition (MIT): a strong electron correlation driven Mott-Hubbard transition[32–34], a Peierls structural distortion driven MIT[35–37] or a cooperative Mott-Peierls mechanism[38].

The understanding of the mechanism at the origin of MIT is crucial in order to improve the phase transition. However, this is complicated by the coexistence of different driving forces. Because of the complex interplay between charge, lattice and orbital degree of freedom, an unambiguous theoretical or experimental explanation of the MIT is not yet available. To experimentally approach this long-standing problem, it is necessary to characterize across the phase transition a coherent set of samples with controlled properties, using techniques, which concurrently probe more than one degree of freedom.

In this thesis, two sets of VO_2 samples (three crystalline strained films and one disordered nanostructured films) have been characterized and studied using different experimental techniques. Thin and ultra-thin crystalline samples have been characterized using X-ray Photoelectron Spectroscopy (XPS, Appendix 1), Resonant Photoemission (ResPES, appendix 3.1) and X-rays Absorption Near Edge Structure (XANES, Appendix 2) acquiring two different Auger Channels O $KL_{23}L_{23}$ and V $L_3M_{23}M_{45}$. The nanostructured (NS) VO_2 samples have been characterized using XPS, Ultra Violet Photoelectron spectroscopy, Work function measurements, XANES in total electron yield and Transmission electron microscopy. The details of the samples' preparation and characterization are described in Chapter 2.

The phase transformation has been studied using XANES, ResPES and Constant initial state spectroscopy (CIS) in order to disentangle the orbital-structural-electronic contributions to MIT. The analysis and the obtained results are presented and discussed in Chapters 3 and 4.

1.1 The Metal-Insulator Transition theory

The phenomenological definition of a metal and an insulator is quite straightforward: a metal is a material capable to conduct electricity while an insulator does not. To have a more rigorous definition of the metallic and insulator state we had to wait until the early ’30s of 1900 when the band theory has been developed[39]. The first real breakthrough was the demonstration of the Bloch theorem, which explains the quantum-mechanical motions of electrons in a periodic lattice potential. The eigenvalues of the solution of the Schrödinger equation proposed by Bloch, are the energy bands shaped by the electron crystalline momentum k, and it can be seen as the solid-state analogue to the discrete energy levels in atoms. Within the band theory of solids, a metal is defined as a material with a partially filled valence band whereas an insulator exhibits a completely filled band. The classification of solid-state properties using band theory has been extremely successful. However, not all materials with a predicted partially filled band (in particular TMOs) show the conducting behaviour[40].

To understand this discrepancy, it is necessary to remember that band theory and the Bloch theorem have been developed within the independent particles approximation. As proposed by the Nobel prize N.F. Mott[41], introducing the Coulomb interaction among electrons we observe spatially localised electronic wave functions. Including a mutual electron repulsion, it is possible to explain the insulating behaviour of some oxides (e.g., NiO) and predict metals insulator transitions. However, electron correlation is not the only way in which an MIT can occur.

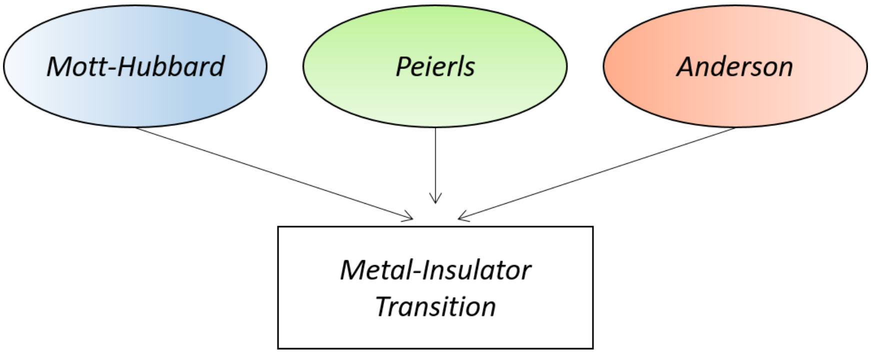

Figure 1.1.1: Three main mechanisms for a metal-insulator transition (MIT).

A complete theoretical description of the criteria that leads to MIT in solids is behind the purpose of this thesis and a rigorous treatment is available in the literature[42]. In the next sections, the three main MIT mechanisms will be described: the electron correlation induced Mott-Hubbard transition, the structurally driven Peierls transition and the disorder based Anderson localization.

1.1.1 Mott-Hubbard transition

Mott-Hubbard metal-insulator transition is a first-order transition generated by the strong mutual repulsion between electrons inside the solid. Transition metal oxides as well rare earths compounds can form crystalline solids with narrow d or f bands and therefore a narrow kinetic energy distribution. In certain cases, when the electron density is too high and the mutual

Coulomb interaction is higher than the kinetic energy dispersion there is an energy gain if the d or f wave functions are localized around the metal ion instead of being itinerant i.e. a bandgap is opened.

These classes of compounds are called Mott insulators. Mott proposed a general criterion (Mott criterion) according to which a conventional band metal actually behaves as an insulator when:

$$a_h N^{1/3} \lesssim 0.25 \tag{1.1.1}$$

where a_h is the effective Bohr radius of the valence electrons, and N is the electron density.

Mott suggested that the metallic state occurs in these materials as an excited state while the (Mott) insulator electronic structure is associated with electron-hole excitons[43]. An equivalent point of view is to consider that in strongly correlated systems the conduction happens through tunneling mechanism. Therefore, the presence of insulating or metallic states is determined by the relative magnitude of the mutual Coulomb repulsion between two electrons on the same site and the energy transfer integral.

Mott suggested that MIT should be sharp since as soon as electrons have enough kinetic energy to overcome the tunnel barrier, the system turns to metallic. Hubbard presented a more rigorous, but still semi-quantitative, description of the Mott transition introducing the effects of correlation in the Hamiltonian of interaction[34]. He formalized the second quantization Hamiltonian as composed of two terms: the first accounts for the hopping of one electron among different sites, and the second for the mutual electron-electron Coulomb interaction. The Hubbard model can be seen as an implementation of the tight-binding model in which also the on-site Coulomb repulsion is considered. Competition between the hopping energy and the Coulomb repulsion determines the physics described by the Hubbard model. The Hubbard Hamiltonian has been extremely successful since it predicts the existence of a Mott insulator when the Coulomb repulsion (U) dominates over the hopping term. However, the energy gap due to electronic correlation shrinks continuously as the ratio of electron bandwidth (W) to U increases and becomes zero at a critical ratio when the insulator to metal transition occurs. This is not a sharp transition as predicted by Mott and it is a consequence of neglecting the inter-atomic Coulomb term, which is responsible for the screening effects. Despite the great success of the Hubbard model, it only approximates the exact solutions. Even though theoretical methods moved forward there is not yet a general consensus on one specific model [33,35,38].

In synthesis, the Mott-Hubbard transition splits a valence band with metal character (*d*-band) in a bonding and anti-bonding contribution. Among the different experimental techniques, it can be detected using the optical conductivity while XANES investigates the collapse of the bandgap across the phase transition. At variance, the photoemission technique may discriminate between the coherent and incoherent quasi-particle excitations in the valence band. In this thesis, XANES coupled with ResPES has been used to monitor the closing of the bandgap and the Fermi Level (FL) population in order to find a correlation with the different structural properties of our strained samples.

1.1.2 Peierls transition

Peierls transition is a structural phase transition occurring in one-dimensional (1-D) systems. In an equally spaced atomic mono-dimensional system, the electron-phonon interaction is such to lead to the formation of atomic dimers doubling the lattice period. A bandgap at the FL is opened as a consequence of the change in periodicity, turning the system from conductive to insulating. Despite a pure 1-D system is an ideal model, Peierls transition is of extreme interest for materials, which possess 1-D-like features, e.g.: polymer chains, 3-D solids with a strongly directional orbital order or quasi 2-D layered materials, e.g., transition metal dichalcogenides, which exhibit a super-lattice distortion with the doubling of the lattice period.

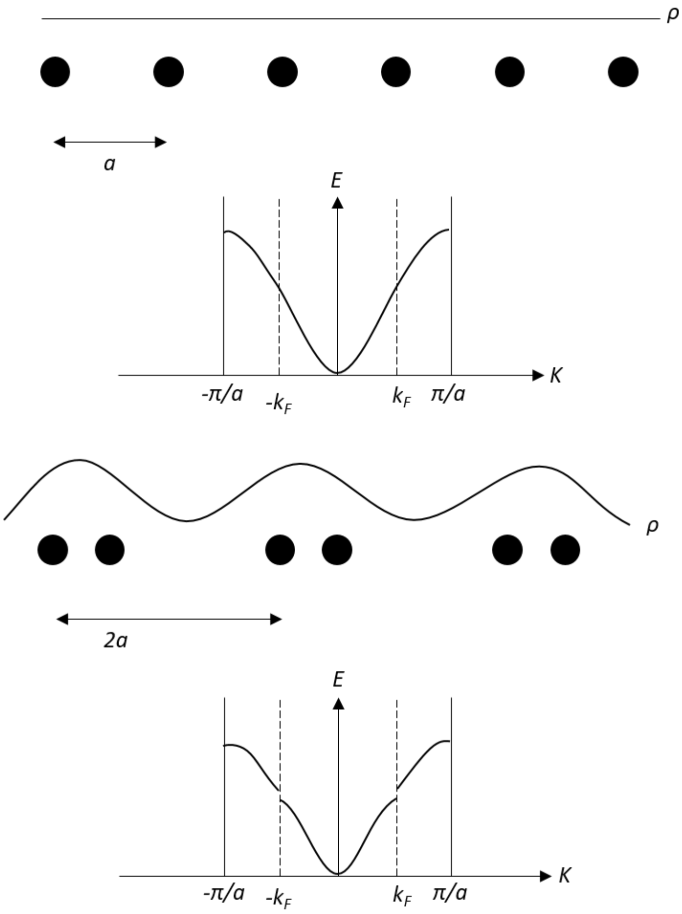

Figure 1.1.2: Schematic representation of the Peierls distortion. Top panel: 1-D chain of monovalent atoms along with the density of charge distribution (ρ) and the energy-crystalline momentum dispersion relation in the undistorted scenario. Bottom panel: atomic dimerization with the consequent modulation of the charge distribution and doubling of the lattice constant. In this distorted scenario, the bandgap opens at k_F.

Rudolf Peierls demonstrated this theorem in the 1930s when writing a section on one-dimensional models in an introductory solid-state textbook [37]. His theorem states that a one-dimensional (1-D) chain of monovalent atoms is unstable, but except in the book, he never published its description. Considering a 1-D atomic chain formed by N equally spaced atoms, the Hamiltonian describing the system can be written as the sum of the free electron Hamiltonian H_0 and V(x), a periodic lattice potential. Using the second-order perturbation theory to develop the periodic potential contributions it can be demonstrated that the minimum energy configuration is that corresponding to the dimerization of the atomic chain with the concurrent opening of the bandgap at k_F. In the lower panel of Figure 1.1.2, is reported the distorted configuration with the gap opening.

The pairs of atoms double the lattice period and create two different bond lengths. The opening of the bandgap in the single-particle excitation spectrum, push the electrons around k_f toward lower energy levels respect to the unperturbed case. The Peierls distortion is energetically favourable when the energy savings due to the band gaps opening outweighs the elastic energy necessary for ion rearrangements. In the distorted chain the electrons condensate forming electrons-holes pairs is characterized by a collective mode with wave vector $2k_f$ and the charge density distribution defined as [44]:

$$\rho(r) = \rho_0 + \rho_1 \cos(2k_f r + \varphi) \tag{1.1.2}$$

where ρ_0 is the unperturbed charge density (constant), ρ_1 is the amplitude of the oscillation and φ is the phase shift. The condensate is called Charge Density Wave and its formation is mainly a 1-D phenomenon, even if it has been observed also in 2-D and 3-D systems [44]. It is important to underline that the Peierls transition is mainly observed when thermal excitations are minimized, i.e. at low temperature. Increasing the temperature, the atomic chain may acquire enough vibrational energy to arrest the dimerization and therefore to close the bandgap. The Peierls distortion can be experimentally observed using all ~~those~~ techniques able to track, directly or indirectly, the atomic positions within a solid. X-ray diffraction (XRD), X-ray Absorption Fine Structure (XAFS) for bulk materials and Low Energy Electron Diffraction (LEED) for 2-D materials can directly probe the atomic pair formation and the doubling of the unit cell across the transition. Techniques like Raman spectroscopy and XANES can be also used to probe the transition from the spectroscopic signature (the vibrational mode and the empty band formation, respectively) following the atoms dimerization.

In this thesis, XANES spectroscopy has been used to investigate the empty band evolution across the VO_2 phase transition for samples with different structural properties. As will be explained in section 1.3.2, the Peierls distortion results in the spectroscopic fingerprint of the empty density of states, which evolution has been studied by means of XANES.

1.1.3 Anderson localization

In 1958 Philip Anderson published his seminal paper on how the presence of a critical amount of disorder can turn a metal into an insulator[45]. The conduction reduction is associated with the spatial localization around the lattice ion of the electronic wave function. Anderson localization can be understood as an interference phenomenon. In the original manuscript, a tight-binding model in which the electron can hop from a site to another via tunnel effect describes the model. Nevertheless, increasing the degree of disorder the forward propagation quantum amplitudes tend to zero because of the destructive interference, resulting in a localized wave function. An equivalent model has been proposed in the literature in which the incoming wave is scattered off from the disorder-generated potential. For a high enough disorder, the waves interfere destructively resulting in an exponential decay of the amplitude[46,47].

The main results of the Anderson analysis are two:

- in the case of one and two dimensions solid, an arbitrary degree of disorder results in the localization of the wave functions;
- in the case of three-dimensional solids exists a critical value of W above which the conduction is inhibited. W is the width of the stochastic distribution of the eigenvalues of the Anderson Hamiltonian.

W is usually as big as the mean Schrödinger equation eigenvalues energy, therefore a perturbative approach cannot be pursued. However, advanced numerical approaches are being developed in order to simulate and predict the disorder-induced degree of localization in solids. In the Anderson MIT, the FL occupation is coupled to the transition from disorder to order. The combination of experimental techniques sensitive to sample order and to FL occupation can be exploited to study the Anderson localization. In this thesis, we used the combination of XANES and ResPES to investigate the local order and the evolution of the metallicity of the VO_2 nanostructured disordered sample subjects to the heating treatment.

1.2 VO_2 structural properties

The crystalline structure of VO_2 is different in the metallic and insulating states. In the high-temperature metallic phase (above 67 °C in single crystal) VO_2 has a lattice structure belonging to the tetragonal symmetry. This phase is commonly referred to as rutile. The vanadium atoms are positioned at (0,0,0) and (½, ½, ½) with a_r=b_r=4.554 Å and c_r=2.851 Å [48,49]. According to the Pauling rules[50], vanadium atoms are surrounded by oxygen octahedra, which can be considered the basic coordination complex of the crystal structure. The octahedron sites share edges only along c_r (rutile c axis) which introduces a small orthorhombic distortion within the octahedron[36] generating two different V-O distances: equatorial end apical. The two apical oxygen have position ± (u, u, 0) while the four equatorial oxygen atoms ±(±(u-½), ∓(u-½); ½) where u=0.3001 at 360 K[48,49]. The equatorial distance is between the metal atom and the four neighboring oxygen atoms with $z = z_{metal} \pm ½$.

Apical and equatorial V-O bond lengths depend on the unit cell edges length, i.e. lattice parameters. In particular apical V-O (J_A) linearly depends on the a_r length:

$$J_{Apical} = J_A = \sqrt{u^2 a_r^2 + u^2 b_r^2} = \sqrt{2u^2 a_r^2} = \sqrt{2}\, u a_r \qquad (1.2.1)$$

The equatorial bond length (J_E) includes all the lattice parameters.

$$J_{Equatorial} = J_E = \sqrt{(u-\tfrac{1}{2})^2 a_r^2 + (u-\tfrac{1}{2})^2 b_r^2 + \tfrac{1}{4} c_r^2} = \sqrt{2(u-\tfrac{1}{2})^2 a_r^2 + \tfrac{1}{4} c_r^2} \qquad (1.2.2)$$

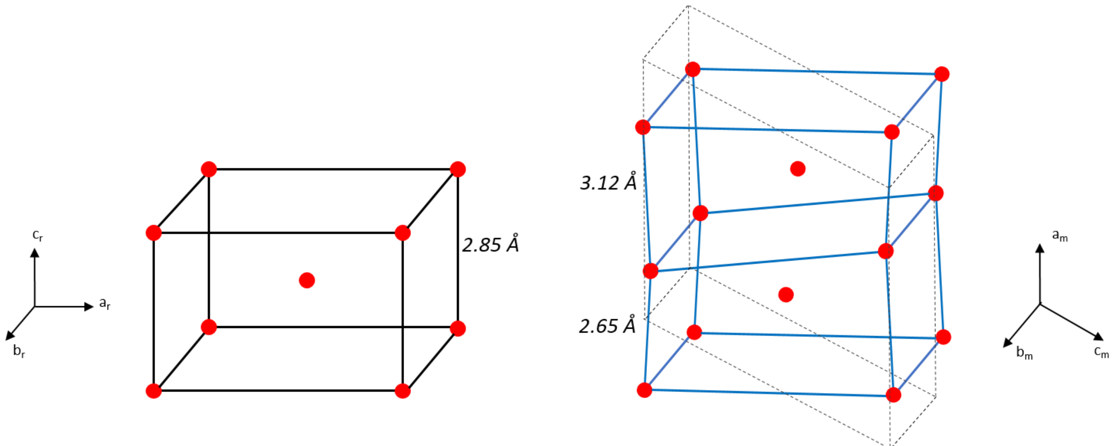

Tetragonal- HT

Monoclinic-LT

Figure 1.2.1: Schematic representation of the high temperature tetragonal (left) and low temperature monoclinic (right) unit cell. Only V atoms are depicted for clarity (red dots). In the low-temperature monoclinic phase, the unitary cell (dashed black line) is doubled respect to the tetragonal structure (continuous black line). The V-V dimerization and tilting results in the appearance of two V-V distances. The values are taken from[51]. *The doubling of the unit cell and the V-V dimerization are a fingerprint of a Peierls transition.*

The low-temperature phase is the distorted high-temperature structure and belongs to the monoclinic symmetry. Across the phase transformation, the vanadium atoms pairs ~~and~~ tilt along the rutile c axis. As can be seen in Figure 1.2.1 the unit cell doubles the size respect to the tetragonal phase and two different V-V lengths appear along the a_m (c_r) axis. The sum of the inter-pair and of the extra-pair distances is ≈ a_m ≈ $2c_r$, which is the fingerprint of the Peierls transition. The crystal structure parameters are: a_m=5.751 Å, b_m=4.537 Å, c_m=5.382 Å, β=122.646°[52].

This insulating phase is called M1. The structural phase transition is usually concomitant with the MIT. However the influence of external parameters like strain[53,54] or pressure[55], or studying the photo-induced transition on the ultra-fast timescale[13,56], MIT and Structural Phase Transition (SPT) can be separated, and different monoclinic distorted metastable phases can be observed e.g. M_2 and T[57]. M_2 phase is characterized by the existence of two sub-lattice of vanadium atoms: in the first, they are paired along the c_r axis but not tilted, in the second they are not paired but tilted perpendicularly to the c_r axis. The T phase is intermediate between the M_1 and M_2 in which part of the vanadium atoms are unpaired and part are tilted.

The existence of the metastable insulating phases of VO_2 can no longer be explained with the electron-phonon interaction, pointing out the important role of electron correlation in VO_2 MIT.

1.3 VO_2 Band structure

To have a deep insight into the MIT mechanism, it is necessary to understand how the band structure evolves when crossing the phase transition. Understanding how the orbital features are connected to the other degrees of freedom involved in the MIT is of crucial importance.

In VO_2 the band structure is the result of the respective arrangements of vanadium and oxygen atoms, electron correlation and O-V hybridization. In TMO the oxygen atoms have a complex influence on the energy levels of the TM atom. The first attempt made to explain the effect of the oxygen (or ligand) geometric arrangement on the transition metal orbitals has been made by Bethe and Van Vleck in the early years of 1930 [58,59] with the introduction of crystal field theory.

1.3.1 Crystal Field theory

Crystal field theory (CFT) describes the degeneracy breaking of the outer valence orbitals (in the case of study V *3d* orbitals) induced by an electrostatic negative charge distribution (anions or ligands). This theory has been often applied to describe TM coordination complexes, in which the central atom usually metallic (coordination centre) is surrounded by oxygen atoms or molecules with ligand character.

A brief overview of CFT highlighting its main characteristics is proposed in this section.

In CFT the coordination centre and the ligands are respectively considered as positive and negatives point charges. The theory defines the energy changes undergone by the outer *3d* manifold of TM atoms when surrounded by oxygen atoms. The interaction between the ligand and coordination centre orbitals are not taken into account in this theory. The proximity of the ligand atoms to the coordination centre, implies that the ligand is closer to certain *3d* orbitals and further to others, lifting the degeneracy. The details of the energy splitting are mostly dominated by:

- The nature of the ligands and of the metal atoms,
- The coordination of the central atoms, which determines the geometric arrangements of the ligands.

In vanadium oxides, the ligands dispose at the vertex of an octahedron with the vanadium atom in the middle [50]. The octahedral coordination is one of the most common in transition metals oxides; in addition, the other coordination geometries (tetrahedral, trigonal, etc.) can be described starting from the octahedral case. To understand how the degeneracy is removed by the octahedral crystal field, it is necessary to remember the orientation of the five *3d* orbitals.

Given a Cartesian frame of reference XYZ (see Figure 1.3.1a), the five *d* orbitals are directed toward different directions. The orbital d_{z^2} points toward the Z axes, $d_{x^2-y^2}$ toward the X and Y axes and d_{xy} d_{zx} and d_{yz} are directed along the bisector of the XY, ZX and YZ planes respectively. Assuming the presence of a spherically symmetric negative field surrounding the central atom, the atomic degenerate *3d* manifold is lifted in energy since al the orbitals feel the same electric field.

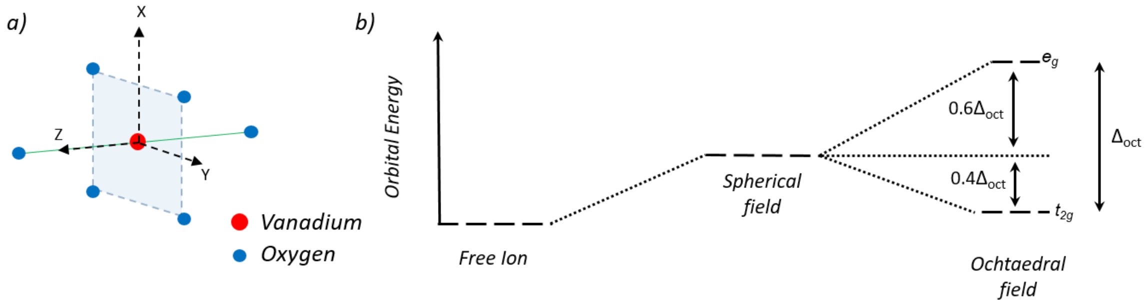

Figure 1.3.1: a) Vanadium (red) and oxygen (blue) atoms arrangement. The frame of reference XYZ is also depicted for clarity. b) Diagram of the energy level splitting in an octahedral crystal field

If 6 negatively charged ligands are placed: 2 along the Z-axis and 4 along the XY plane bisectors (as in figure 1.3.1a) the *3d* manifold is split as reported in Figure 1.3.1b. The orbitals d_{z^2} and d_{xy} which points directly along with the ligands, undergoes a higher repulsion by oxygen presence therefore they are lifted in energy. On the other hand, the orbital $d_{x^2-y^2}$, d_{zx} and d_{yz} pointing between the ligand atoms are less influenced. There is a loss of degeneracy that results in the splitting of the *3d* manifold in two groups of orbitals: d_{z^2}, d_{xy} and $d_{x^2-y^2}, d_{zx}$ and d_{yz}.

According to group theory, the octahedral symmetry belongs to the point group O_h. d_{z^2}, d_{xy} belong to the irreducible representation e_g whereas $d_{x^2-y^2}, d_{zx}$ and d_{yz} to the t_{2g}. The octahedral field has the effect of splitting the *3d* manifold in two high energy e_g and three low energy t_{2g} levels. The energy separating the two groups of orbitals Δ_{oct} (or often $10D_q$) is called crystal field splitting. Referring to the energy of the spherical field, the octahedron geometry lifts the e_g levels of $0.6\Delta_{oct}$ while lower the t_{2g} of $0.4\ \Delta_{oct}$.

The crystal field splitting can be measured through absorption spectroscopies (UV-VIS or XANES) and it is a direct measure of the order of the geometric arrangement of the ligands around the central atom. Distortion effects of the Jahn-Teller type can additionally split the energy levels and thus reduce Δ_{oct} allowing to extract information about the short-range order of the sample.

1.3.2 Ligand Field Theory

Ligand field theory (LFT) is the application of molecular orbital theory to transition metal complexes. The basic of LFT is the introduction of the interaction between the metal and ligand orbitals within the CFT framework. It has been developed at the end of 1950 by B. S. Griffith and L. Orgel [60] with the purpose to increase the accuracy of CFT.

Orbitals combination between metal and ligands are allowed only between states with the same symmetry. In an octahedral field, the oxygen atoms form σ bonds with the d_{z^2} and d_{xy} orbitals. In VO_2 the d_{zx} and d_{yz} forms π type bonds with the oxygen orbitals leaving $d_{x^2-y^2}$ non-bonding. The first description of the VO_2 band structure by LFT is due to J.B. Goodenough in 1971[36]. The Goodenough model collected a wide consensus in the scientific community and a schematic diagram is proposed in Figure 1.3.2.

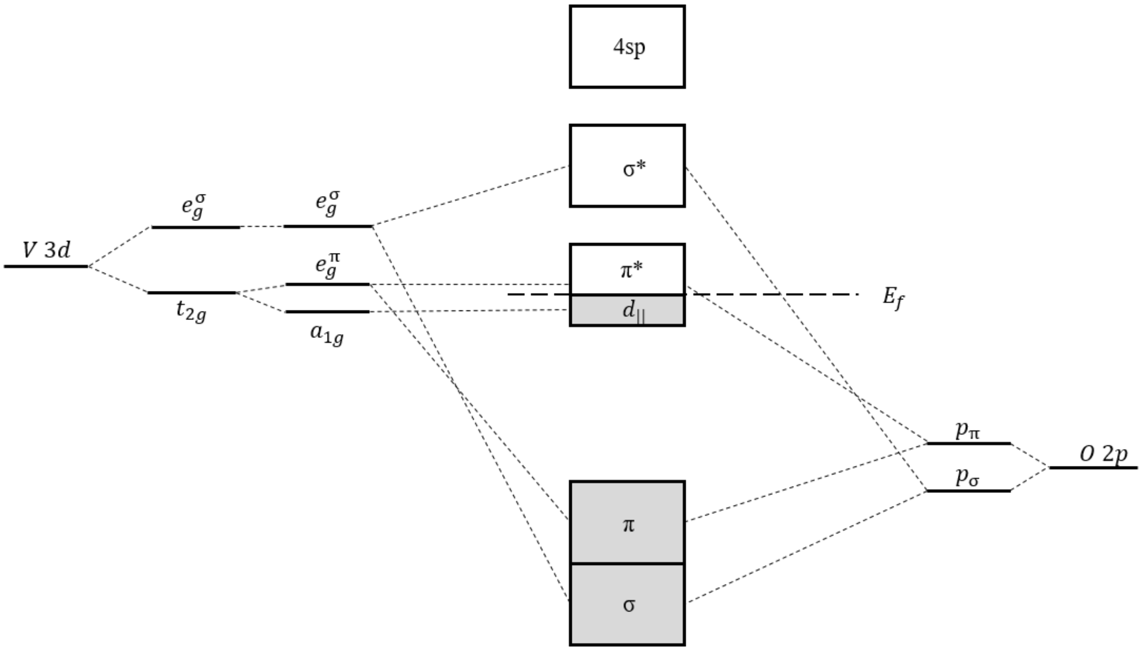

Figure 1.3.2: Oxygen-Vanadium orbital contribution to the VO_2 (metallic phase) band structure. The V t_{2g} orbitals are further split because of the orthorhombic distortion into one non-degenerate a_{1g} and twofold degenerate e_g. The grey-shaded orbitals are occupied by electrons, while the white orbitals indicate empty states. Only the V 3d and O 2p orbitals are depicted for clarity.

Crystal field-effect splits the degenerate *3d* manifold into 3 t_{2g} and 2 e^σ_g levels. The 2 degenerate e^σ_g overlap with oxygen p orbitals with σ character (p_σ). The bonding and anti-bonding combinations of the e^σ_g-p_σ bonds are labelled as σ and σ*. A small orthorhombic distortion directed along the c_r axis (X-axis in the XYZ frame of reference of Figure 1.2.1a), further splits the 3 t_{2g} levels in one not degenerate a_{1g} and twofold degenerate e^π_g states. The e^π_g orbitals hybridize with the π symmetric O *2p* orbitals (p_π) while the a_{1g} orbital is not involved in the V-O bonding. The e^π_g -p_π orbital admixture results in a bonding π band and in an anti-bonding π* band. The a_{1g} is formed by the $d_{x^2-y^2}$ orbital and is directed along the c_r (a_m) axis and is responsible for vanadium-vanadium intermetallic bonds. The latter orbital is historically called $d_{||}$.

The major spectral changes across the MIT occur at the Fermi Level (FL), in Figure 1.3.3 are depicted the detailed orbital evolution of the VO_2 band structure crossing the phase transformation.

In the metallic phase (Figure 1.3.3a) the $d_{||}$ and π* orbitals cross the FL and are partially degenerate. Their relative position (respect to the FL) and occupation depend on the hybridization between V *3d* and O *2p* orbitals and by the c_r/a_r ratio as will be explained in section 2.1.1. In bulk crystalline VO_2 π* is less occupied (or more empty) respect to $d_{||}$. For the occurrence of MIT the $d_{||}$ needs to be stabilized (lowered in energy) and π* destabilized (shifted to higher energy) respect to the FL. The structural distortion described in the previous section, pairs and tilts V atoms moving them away from the center of the octahedron.

In the insulating phase (Figure 1.3.3b) the dimerization of vanadium atoms increases the overlap of the $d_{||}$ orbital on different V sites, therefore, stabilizing to lower energy the $d_{||}$ orbital while creating the empty $d^*_{||}$ (t_{2g} character) band. The off-centre position of V atoms in the insulating state increases also the overlap between vanadium and oxygen atoms which results in increased stabilization of the π band and therefore the consequent destabilization of the π*, which is shifted above the FL [36].

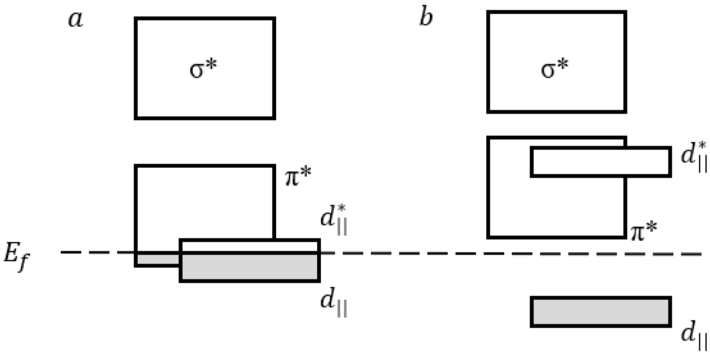

Figure 1.3.3: Band structure modifications across the MIT near the Fermi level. a) metallic phase, b) insulating phase. The grey-shaded orbitals are occupied by electrons, while the white orbitals indicate empty states.

In the insulating phase (Figure 1.3.3b) the dimerization of vanadium atoms increases the overlap of the $d_{||}$ orbital on different V sites, therefore, stabilizing to lower energy the $d_{||}$ orbital while creating the empty $d_{||}^*$ (t_{2g} character) band. The off-centre position of V atoms in the insulating state increases also the overlap between vanadium and oxygen atoms which results in increased stabilization of the π band and therefore the consequent destabilization of the π*, which is shifted above the FL [36]. The $d_{||}^*$ is directed along the c_r axis in the metallic phase and along the V-V dimer in the insulating phase and it is strictly related with the unidimensional V-V dimer chain formation in the monoclinic insulating phase [61], while the π* is more isotropic within the lattice [62]. The model proposed by Goodenough depicts a structurally driven phase transition triggered by V-V pairing and tilting. However, Zylbersztejn and Mott argued that the vanadium atoms dimerization is not necessary to the opening of the bandgap since M_2 and T phases, which have only half of the vanadium atoms paired are still insulating, pointing out the role of the electron-electron interaction [33]. In any case, it is evident the interplay of the structural orbital and the electronic degree of freedom in the MIT dynamics. In the next chapters will discuss how the lattice structure affects the orbital ordering. Three strained samples with different degrees of unit cell distortion and completely disordered samples (lack of long and short-range order) will be investigated. Their synthesis methods and structural properties are described in Chapter 2. The complex interplay among the different degrees of freedom will be discussed in Chapter 3 using advanced spectroscopic techniques like XANES and ResPES. There I will provide an insight into the FL occupation evolution and in the orbital dynamics across the MIT. Chapter 4 will present additional information about the orbital contribution to the MIT by means of the Constant Initial State (CIS) spectroscopy.

Chapter 2.

VO_2 thin film and nanostructured film synthesis

VO_2 MIT features (transition temperature, hysteresis width and amplitude) are deeply influenced by sample structure (single crystal, polycrystalline, disordered samples, etc.) [63].

In section 1.3.2 it has been shown the importance of vanadium and oxygen relative position to determine the electronic structure properties of VO_2. V-O arrangements can be controlled during the materials synthesis stage and, thus having the possibility to study the VO_2 electronic structure under different lattice conditions. The production of VO_2 films with different structural properties is therefore essential in order to understand the combined influence of electronic and lattice degrees of freedom on MIT.

Two main approaches have been adopted to modify vanadium and oxygen atoms disposition within the lattice: synthesis of strained samples and synthesis of NS samples.

In this chapter, a survey of the synthesis methods used to produce the samples discussed in this thesis is presented. Section 2.1 is devoted to a brief overview of Molecular Beam Epitaxy (MBE) technique, which allowed to synthesize strained crystalline samples. In Section 2.2 the use of Supersonic Cluster Beam Deposition (SCBD) method for NS VO_x films production is presented. This method allowed us to obtain disordered VO_2 films.

2.1 Thin and ultrathin strained samples synthesis: MBE

Lattice strain is an effective way to slightly modify in a controlled fashion the atoms' positions within a solid. Strain application relies on the ability to synthesize thin crystalline samples on a properly oriented substrate. The lattice mismatch between the sample and the substrate must not be too severe therefore the substrate needs to have the same lattice symmetry of the sample deposited but with different unit cell edges length. In the early stage of growth, the lattice of the deposited sample undergoes a strain (tensile or compressive depending on the substrate choice) in order to match the lattice parameters of the substrate. Increasing the sample thickness the lattice relaxes to its bulk value.

Strain control has been proven as an effective method to tune MIT features (critical temperature, orbital occupancy, etc.) in VO_2 [62,64,65]. The interest in developing a technique able to synthesize single-crystalline samples controlling their cell edges length is twofold: the MIT control and the understanding of its nature.

MBE matches all the latter requirements allowing the synthesis of samples of pure VO_2 with different degrees of strain.

Epitaxy refers to the discipline of growing crystalline materials on a crystalline substrate. Among the different deposition techniques developed to produce crystalline overlayers, MBE proved its importance in the synthesis of monocrystalline thin films of complex oxides [66].

MBE was developed by J. R. Arthur and Alfred Y. Cho in the late 60s at Bell laboratories [67,68] and it takes place in ultra-high-vacuum (UHV) conditions (10^{-10} mbar). In MBE the material of interest, usually a metal, is heated within a crucible placed inside the UHV deposition chamber. The heating process is carried on until the metal slowly begins the sublimation process. The UHV environment guarantees to the evaporated atoms a mean free path long enough to impact on the substrate surface where the condensation begins. Different elements can be evaporated at the same time, enabling the synthesis of complex compounds.

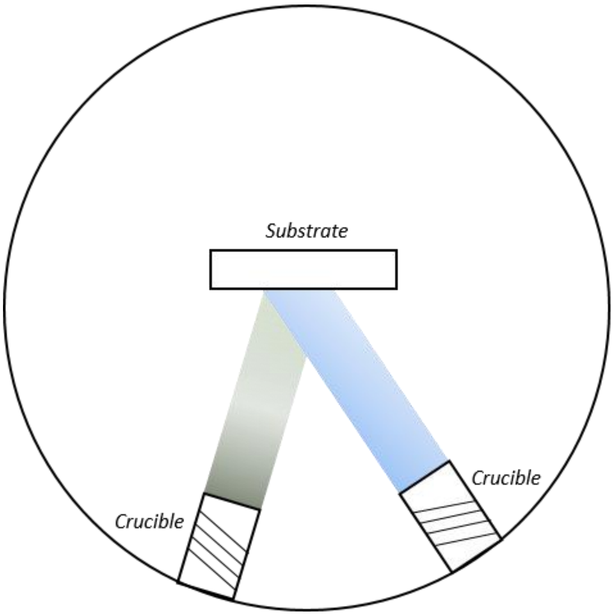

Figure 2.1.1: schematic representation of a MBE deposition apparatus.

The strength point of MBE is the constant deposition rate (typically of the order of 0.1 Å/s) that allows the films to grow epitaxially. The amount of heat supplied to the crucible defines the rate of the metals evaporation and the deposition rate on the substrate.

In order to produce single-crystal metal oxide thin films, it is necessary to introduce oxygen in the experimental chamber using a mass flow controller.

Radio Frequency (RF) assisted Oxide MBE is often performed. In this variant of the MBE process, an RF plasma source is used to provide reactive oxygen radicals that will interact with the metals atom at the moment of deposition.

In this thesis we investigated films of VO_2 with a thickness of 8, 16 and 32 nm deposited on a clean substrate of TiO_2 (001) by the RF-plasma assisted oxide-MBE instrument, working with a base pressure better than $4x10^{-9}$ mbar. At a constant growth rate of 0.1 Å/s, the thickness was controlled by adjusting the deposition time in a range from several unit cells to tens of nanometers. During the deposition, the substrate has been kept at 550 °C.

The interfacial cross-section has been investigated with a high-resolution scanning transmission electron microscope (STEM). High angle annular dark-field (HAADF) STEM images were taken on a JEM ARM200F with a probe aberration corrector, while the diffraction pattern was acquired on a JEM 2100 TEM. The complete details of the epitaxial film preparation and characterization performed at the University of Science and Technology (Hefei, P.R. China) are reported elsewhere [64,65].

The samples have been produced in China and moved to Elettra synchrotron radiation facility for ex-situ investigation.

In the following, the strain-induced modification of the VO_2 crystal structure is reported.

2.1.1 Strain influence on structural properties

The TiO_2 substrate has the rutile (tetragonal) lattice structure as the metallic phase of VO_2. For the rest of this section, most of the considerations are referred to as the rutile phase of VO_2.

TiO_2 substrate is oriented along the (001) surface, thus for the lattice mismatch calculation, the *a* and *b* structural parameters have to be addressed.

The in-plane lattice mismatch between sample and substrate can be calculated as:

$$M = \frac{a_s - a_f}{a_f} * 100 \tag{2.1.1}$$

Where a_s and a_f *are* the lengths of cell edges of the substrate and of the sample, respectively.

Between rutile TiO_2 (a=b=4.58 Å) and bulk VO_2 (a=b=4.55 Å) there is a lattice mismatch M=0.66%. Since titanium dioxide has larger unit cell edges, during the early stage of epitaxial grow, VO_2 film will undergo a tensile strain in order to match the substrate lattice. For a thin film, the net effect is that of an increase of a_r and b_r lattice constant and the consequent elastic compression of c_r [24,62,64]. Increasing the overlayer thickness, the influence of the substrate fades and the lattice constants relax to the bulk value.

For the samples analyzed in this thesis, the critical thickness above which the sample can be considered bulk-like is 25.5 nm [64].

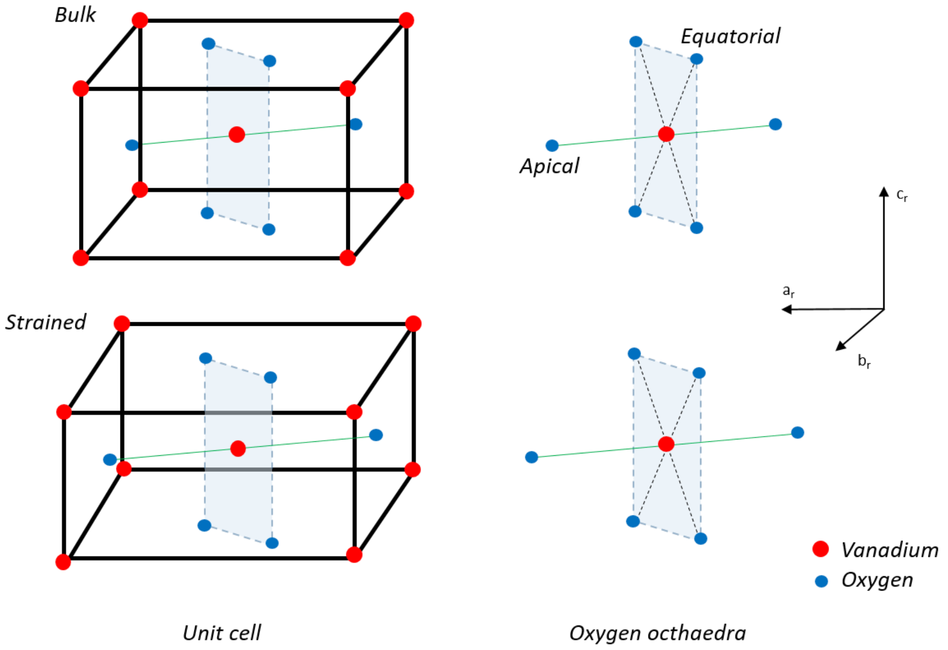

Figure 2.1.2: Schematic representation of the rutile metallic VO_2 unit cell (left) and oxygen octahedron surrounding vanadium atoms (right) for bulk and strained $VO_2/TiO_2(001)$. The oxygen octahedra are depicted to underline the orthorhombic distortion that allows differentiating between equatorial and apical oxygen. The mismatch between TiO_2 (a_r=b_r=4.58 Å) and VO_2 (a_r=b_r=4.55 Å) increases the a_r and b_r lattice parameter in the epitaxial film and thus decrease c_r. This results in an increase in the apical V-O bond length.

From equations 1.2.1-2 we can observe that J_a increases as a_r, i.e. the strain, increases, while J_e is more or less unchanged since the increase in a_r is compensated by the decrease of c_r [62].

The increase of the apical bond length reduces the overlap between oxygen and vanadium orbitals and therefore the *3d-2p* hybridization. The π* orbital is the most affected. The decrease in metal-ligand hybridization results in a decrease of the bonding-antibonding energy separation, consequently the π* orbital is downshifted in energy.

The $d_{||}^{*}$ experience the opposite situation, decreasing c_r increases the orbital overlap between vanadium atoms, upshifting the $d_{||}^{*}$.

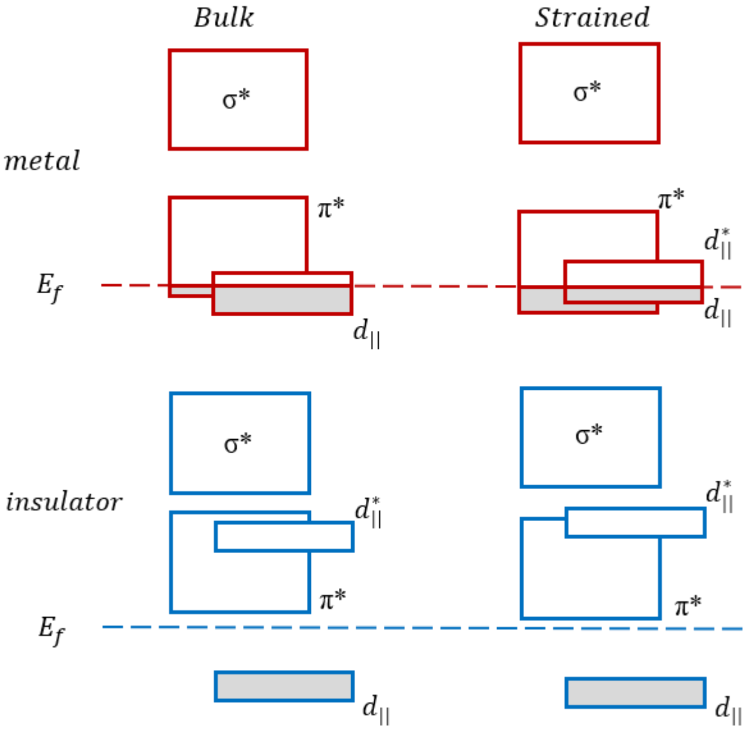

Figure 2.1.3: Orbital evolution as a function of strain for the metallic (top panel) and insulating phase (bottom panel).

In the metal phase the empty part of the $d_{||}$ band is referred to as $d_{||}^{*}$.

The control over the lattice degree of freedom is critical in order to tune the electronic properties of VO_2.

A detailed overview of the interplay between lattice and electronic structure is exposed in Chapters 3 and 4 where three epitaxial films of $VO_2/TiO_2(001)$ with thickness 8, 16 and 32 nm are investigated. The availability of different strained sample (from ultra-strained 8 nm film to bulk-like 32 nm film) is invaluable to understand the lattice influence over the MIT.

2.2 Nanostructured VO_x samples synthesis: Supersonic Cluster Beam Deposition

The class of NS includes solids whose constitutive elements have dimensions ranging from few, up to tens of nm. This definition stands for materials made of different building blocks e.g. nano-crystalline domains, nanoparticles or clusters, nm thin heterostructures, etc. In literature there is not a sharp difference between nanoparticles and clusters; however, there is a general tendency to consider clusters as a small aggregate of few atoms, while nanoparticles indicate an aggregate of at least $3*10^2$ atoms. In this thesis clusters and nanoparticles will be used as synonyms.

NS materials of great interest are those assembled by atomic clusters. These are an aggregation of atoms standing at midway between free atoms and bulk solids. The reduced dimensions guarantee a higher surface to volume (S/V) ratio respect to the bulk, increasing their chemical reactivity [69]. Moreover, their optical, structural and electronic properties depend on the number of constituent atoms [70–72]. In principle, precise control of the synthesis and knowledge of the aggregation properties could lead to the production of nanostructured materials, using clusters as “super-atoms”.

Accurate control over the synthesis parameter is particularly important for VO_x NS films due to the huge variety of oxidation state of vanadium [73].

Supersonic Cluster Beam Deposition (SCBD) has emerged as an invaluable tool for the synthesis of cluster assembled materials because of its high stability and intense cluster production [74]. In the next section the general principles of supersonic expansion, on which SCBD relies, will be presented.

2.2.1 Supersonic expansion of cluster beam

The basic thermodynamic considerations reported in this section have the purpose to highlight the main features of the supersonic expansion of the cluster beam. A complete thermodynamic description can be found in the literature [75,76].

A cluster beam, or more in general, a molecular beam, originates from the expansion of a gas from a high-pressure region P_0 to a low-pressure region P_b (usually high vacuum). The expansion between the two regions occurs through a low conductance nozzle. If P_0/P_b is high enough the expansion of the gas is not dependent on the background pressure and the molecular beam increases its velocity surpassing the sound velocity. The supersonic expansion generates a turbulence region called Mach disk which discriminates between the sub-sonic and the supersonic regime.

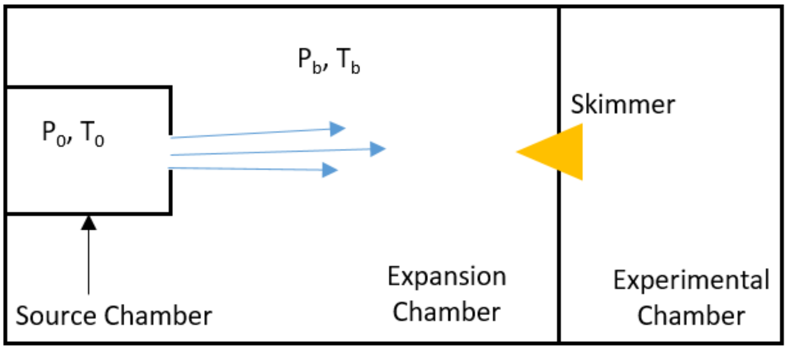

Figure 2.2.1: Schematic representation of an apparatus for molecular beam productions.

The produced beam is extracted from the expansion chamber and brought to the experimental chamber using a conical skimmer before the turbulence region induced by the Mach disc.

In general, if we consider a continuous flow of an ideal gas, the supersonic expansion can be considered isentropic neglecting viscosity and heat transfer effects. It is convenient for studying the system in terms of enthalpy. The stagnation enthalpy of the source chamber can be written as:

$$H_0 = c_p T_0 \tag{2.2.1}$$

Where H_0 is the stagnation enthalpy, c_p is the constant pressure molar specific heat and T_0 the initial temperature of the source. During the expansion because of energy conservation, part of the stagnation enthalpy is converted into kinetic energy.

$$H_0 = H + \frac{1}{2}mv^2 = c_p T + \frac{1}{2}mv^2 \tag{2.2.2}$$

In isentropic approximation, a supersonic expansion implies a cooling of the gas jet. In fact, equation 2.2.2 is valid only if $T_0 > T$, therefore part of the energy of the other degrees of freedom converts into translational energy.

If the expansion is efficient the residual enthalpy H tends to 0 ($T << T_0$) therefore the limit value of the kinetic energy is

$$\frac{1}{2}mv_t^2 = c_p T_0 \tag{2.2.3}$$

Where v_t is the terminal velocity. It is useful to remind that for an ideal gas, the following relations are valid:

$$c_v = \frac{1}{2} f R \tag{2.2.4}$$

$$c_p = c_v + R \tag{2.2.5}$$

$$\frac{c_p}{c_v} = \gamma \tag{2.2.6}$$

$$c_p = \frac{R\gamma}{\gamma - 1} \tag{2.2.7}$$

Where c_v is the constant volume specific heat, c_p is the constant pressure specific heat, R is the universal gas constant and *f* is the number of gas degrees of freedom.

Exploiting equations 2.2.4-7, the terminal velocity can be written as:

$$v_t = \sqrt{\frac{2}{m} T_0 R (1 + \frac{1}{2} f)} = \sqrt{\frac{2}{m} T_0 R \frac{\gamma}{\gamma - 1}} \tag{2.2.8}$$

Supersonic beams can also be pulsed i.e. the source is turned on for a short interval periodically in time. The main advantage of using a pulsed source is the peak intensity is higher respect to continuous sources. In fact, P_b is considerably lower since the background gas is pumped away while the source is turned off, allowing to gain up to a factor of 10^3 on the peak intensity.

The thermodynamic relations described in this section hold also in the case of small perturbation of the "ideal gas" hypothesis. When the molecular beam contains particles of different species, it is called a seeded beam. In SCBD an inert gas (or carrier gas) is seeded with a diluted quantity of clusters (1-10% of the total pressure) so that the seeded beam can be treated as a small perturbation of the pure gas case. The cluster beam is composed of different species (the carrier gas atoms and clusters with different masses). Therefore the specific heat, the terminal velocity, and the average mass need to be defined using a weighted average. Each element of mass m_i has energy:

$$E_i \approx \frac{m_i}{\bar{m}} T_0 \tag{2.2.9}$$

Where $\bar{m}$ is the average mass and m_i the mass of the i-th specie. In synthesis, a heavy species will be accelerated if diluted into a light carrier gas and vice versa. Taking into account the difference in mass between the carrier gas and the clusters is of fundamental importance for the definition of the NS film properties as will be explained in the next section.

2.2.2 Pulsed Micro-Plasma Cluster Source

Pulsed Micro-Plasma Cluster Source (PMCS) [74,77,78] is a pulsed cluster source which proved its importance in nanostructured materials synthesis [79–81] and clusters fundamental study [82,83].

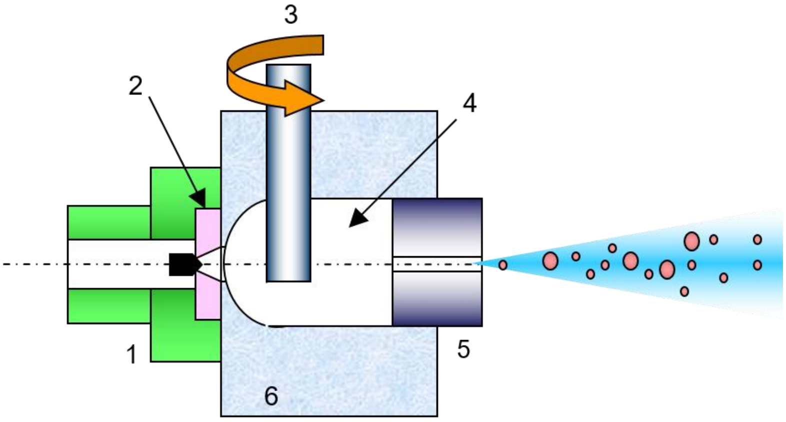

Figure 2.2.2: Schematic representation of the PMCS: 1) Pulsed valve; 2) Anode 3) Rotating cathode; 4) Thermalization cavity; 5) Aerodynamic lenses; 6) Ceramic body.

A schematic representation of the PMCS hardware is reported in Figure 2.2.2. A solenoid pulsed valve overlooks within the thermalization cavity. An electrode (anode) separates the ceramic body and the pulsed valve. The rotating cathode is inserted in a 6 mm hole that crosses the ceramic body perpendicularly to the cluster beam propagation direction. The PMCS works as follows: the pulsed valve injects the carrier gas within the ceramic body with an aperture of the order of hundreds of microseconds creating a region of higher gas density between the anode and the cathode. A pulsed potential difference (500-1000 V) is applied to the electrodes, with a delay of hundreds of microsecond respect to the valve aperture, triggering an intense electrical discharge (about 1000 A) with a duration of tens of microseconds. Consequently, between the electrodes, a plasma of ionized gas is generated, which will impinge the cathode ablating atoms from its surface. The cavity is now filled with an oversaturated gas mixture (carrier gas + ablated atoms) that undergoes a thermalization process starting clusters nucleation and condensation during the supersonic expansion of the beam. The aerodynamic lenses are necessary to improve clusters focusing (especially the small clusters) along the beam direction of propagation and, in addition, using the aerodynamic lenses increases the deposition rate [77,84].

One of the PMCS strengths is the ability to synthesize NS film minimizing clusters coalescence effects. To understand how it is possible, it is useful to study the cluster formation process and the critical parameters to take into account during the deposition stage.

The clusters formation in a seeded beam can be seen as the first stage of a phase transition, in particular, gas condensation. A complete theoretical description of the nucleation process [85–88] goes beyond the purpose of this thesis, however, a qualitative description of the classical nucleation theories is helpful to understand how clusters are generated.

In classical nucleation theory, the clusters' formation is treated as a gas-liquid phase transition [88]. The fundamental ansatz is to assume that the properties of the clusters can be extrapolated from those of a macroscopic quantity of the liquid phase, independently of cluster size. Therefore, a value of surface tension and chemical potential are assigned to the cluster, as it was a spherical droplet. The Gibbs free energy, i.e. the minimum work required to cluster formation has the qualitative trend shown in Figure 2.2.3.

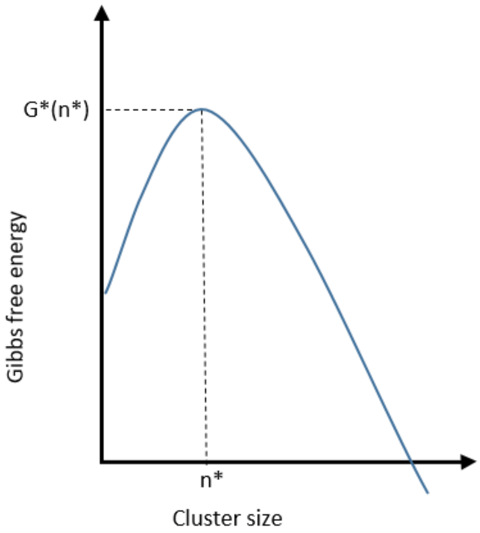

Figure 2.2.3: Qualitative representation of the Gibbs free energy trend as a function of cluster size.

The value n* is a critical point of the Gibbs free energy and defines two size regions. For n<n* the clusters grow increasing their free energy, this region is called embryos region. When n>n*the clusters growth is favoured by the decreasing of the free energy. Nucleation is a process in which the embryos clusters need to overcome an energy barrier defined by G*(n*) in order to grow until observable dimensions. To condensate the gas need to be oversaturated, i.e. for a given temperature, the pressure P must be higher than the vapour pressure P_v. In this model, the processes responsible for cluster formation are monomer addition and evaporation, which compete to reach a steady-state where the growth rate is constant.

This classical viewpoint is oversimplified and it cannot properly describe the process of cluster formation inside a seeded beam. To improve the model, it is necessary to consider that the clusters are diluted in the carrier gas and that the monomer addition cannot be the only growth channel available [89]. Nevertheless, the general considerations over free energy of classical nucleation theory are applicable also to supersonic cluster sources. In a supersonic source, during the first stages of expansion, the gas-cluster mixture is cooled down by particles' collisions. When a cluster reaches the size of n* the growth is then favoured by low energy monomer-cluster and cluster-cluster collisions. The mass distribution of the cluster is determined by the efficiency of these collisions, the geometry of the cluster source and the operational parameters [75].

After the nucleation process, the clusters beam is deposited on a substrate. The different deposition conditions are of paramount importance to determine the nanostructured material properties. The crucial parameter is the relative magnitude of the kinetic energy per atom E and the binding energy of an atom within the cluster ε. Upon landing, if E> ε the cluster will fragment and a strong coalescence is expected, while if E<ε clusters survive to the impact maintaining their individuality. In supersonic cluster sources usually, the value of E is in the range 0.1-1 eV/atom and considering the average binding energy of metal clusters [89], SCBD emerges as a low energy deposition technique. The different influence of cluster impact energy on nanostructured materials property has been widely studied in the literature using experimental and theoretical methods [90–93]. It has been shown that during the deposition of clusters with a kinetic energy per atom of the order of E≈1 eV fragmentation and coalescence may occur [91]. On the other hand, if E≈0.1 eV the impact with the substrate slightly perturb the cluster avoiding fragmentation and coalescence with other clusters. Therefore in order to synthesize NS samples that retain a memory of their gas-phase precursors, it is necessary to accurately control the kinetic energy at the moment of deposition.

Using equation 2.2.8 the terminal velocity of a cluster at the moment of deposition for a He seeded cluster beam and for an Ar seeded cluster beam can be estimated: v_t^{He}=1766 m/s and v_t^{Ar}=588.6 m/s.

The kinetic energy per atom have been calculated for vanadium clusters:

E^{He}=0.85 eV/atom

E^{Ar}=0.09 eV/atom

Using Ar or He as the carrier gas changes E of one order of magnitude. During this thesis, the samples have been synthesized, despite elsewhere specified, using Ar as the carrier gas in order to minimize fragmentation and coalescence. The synthesis of NS film with a memory of their cluster individuality will be experimentally demonstrated in section 2.2.6.

An additional strength of the PMCS is its extreme versatility: the ablation-by-discharge clusters synthesis is one of the few methods available to produce NS film of all kinds of metals, including refractory metals. The "classical" synthesis methods, like MBE, work mainly by evaporation of the metal of interest. This could constitute a technical problem when dealing with materials with a high melting point. In addition, often dedicated oven for different materials is necessary reducing the versatility of the evaporation methods. On the other hand, the only required condition to use a PMCS is to have a conductive cathode. Even semiconductors can be used as target materials, taking into account that heating of the cathode could be necessary.

Despite the enormous applicative potential, SCBD by mean of a PMCS has been mostly used to produce NS film of pure metal, carbon and transition metal oxide with the highest oxidation state [78,79,94,95]. The demonstration that NS film with controllable oxidation state can be produced during the synthesis and not just by air passivation, is still lacking.

During this thesis, we developed a procedure to oxidize the vanadium clusters during the early stage of their synthesis. To obtain homogeneously oxidized nanoparticles, we used Ar (high purity Ar: 99.9995%, SIAD) as carrier gas, mixed with a controlled amount of oxygen (Table 2.1) resulting in an Ar-O_2 gas mixture. To probe the oxidation state of the samples, we used X-ray Photoelectron Spectroscopy (XPS) as described in section 2.2.3.

The samples from section 2.2.3 to 2.2.6 have been synthesized in-situ under ultra-high vacuum (UHV) conditions (base pressure <2×10-9 mbar) by using the SCBD apparatus equipped with a PMCS which is available at Laboratory TASC-Analytical Division [96]. The PMCS was operated with a vanadium cathode (6 mm diam. rod, purity 99.9 %, EvoChem GmbH) generating a supersonic beam of vanadium metal or oxide cluster. The working parameters of the PMCS have been kept constant for all the samples synthesized (delay between gas injection and discharge firing = 0.6 ms; discharge operating voltage 0.925 kV; discharge duration 80 µs; pulsed-valve aperture driving signal duration time 157 µs; pulse repetition rate 3 Hz; Ar pressure 70 bar). The nanostructured film deposition rate measured by a quartz-crystal microbalance ranged from ~30 Å/s for pure Ar as the carrier gas, to ~5 Å /s for the highest oxygen concentration.

To probe the vanadium oxidation state, we deposited VO_x films with >300 nm thickness (measured using a quartz microbalance) on Si or Cu substrates. The typical size of all the samples is about 2 cm^2.

Table 2.1: Stoichiometry of the NS films synthesized at different oxygen partial pressure in the Ar-O_2 carrier gas mixture.

Oxygen partial pressure [mbar]	x in VO_x
15 ± 5	0.6 ± 0.02
40 ± 5	1.5 ± 0.02
50 ± 5	1.6 ± 0.02
60 ± 5	2.2 ± 0.02
70 ± 5	2.45 ± 0.02

The samples were deposited by landing the supersonic beam of nanoparticles onto clean substrates placed inside the sample-preparation chamber of the XPS characterization facility and transferred, maintaining UHV conditions, via a linear translation manipulator into the analysis chamber where pressure was kept below 5×10^{-10} mbar. Here they were characterized by X-ray

Photoemission Spectroscopy (XPS, section 2.2.3) using an Mg Kα lamp (1253.6 eV, not monochromatic) and studied by UPS using a He lamp (UPS, section 2.2.5, He I 21.22 eV) coupled to a hemispherical electron analyzer (PSP, 120 mm). The morphology and the size of the clusters have been analyzed by Transmission Electron Microscopy (TEM) by means of a field-emission TEM (JEM2100F-UHR, JEOL) operated with beam energy 200 KV.

2.2.3 Stoichiometry determination: XPS

Technological applications require precise control over materials properties. Synthesizing samples with the necessary features to match the desired applications is of enormous importance. Vanadium oxides exhibit a wide range of stoichiometric (VO, V_2O_3, VO_2 and V_2O_5) and mixed-valence oxides (Magneli and Wadsley series) [6]. The ability to select a specific VO_x stoichiometry during sample synthesis is crucial to exploit vanadium oxides' applicative potential.

To investigate the stoichiometry, *i.e.*, the ratio between oxygen and vanadium atoms, of the produced samples, we performed core-level XPS spectra of V *2p* and O *1s* electrons. A complete overview of XPS working principles is reported in Appendix 1. Quantitative information has been extracted by fitting simultaneously the line-shape of V *2p* and O *1s* core-levels which is a known indicator of the stoichiometry [97]. For each component (vanadium and oxygen) we used a pseudo-Voigt curve [98]. The ratio of the areas of V and O contributions, multiplied by the appropriate factors (cross-section, detector sensitivity and spin-orbit branching ration) result in the stoichiometric ratio x= [# of oxygen atoms]/[# of vanadium atoms]. From now on we use the stoichiometric ratio thus measured, in the range $0 \leq x \leq 2.5$ to identify VO_x samples since exists a one to one correspondence between x and a specific sample.

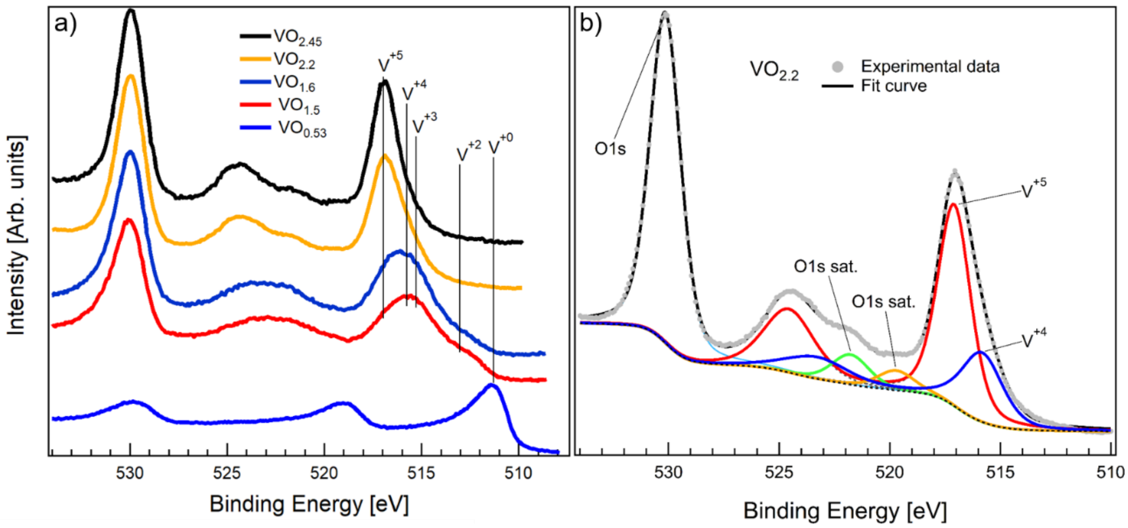

Figure 2.2.4: V 2p and O 1s spectra of vanadium and oxygen. a) V 2p and O 1s core-level spectra of all samples. Peak positions of the vanadium components for different oxidation states are highlighted by straight vertical lines; b) V 2p and O 1s core-level spectra and fit curve of $VO_{2.2}$. The individual fit components are shown as coloured curves. The label O 1s sat indicates the features generated by the Mg $K\alpha_3$ and Mg $K\alpha_4$ component of the radiation.

The core-level spectra of V *2p* and O *1s* electrons of different vanadium oxides synthesized by SCBD are shown in the left panel in Figure 2.2.4; the right panel shows the deconvolution of the experimental spectrum into its different fit components for a selected sample ($VO_{2.2}$). This result proves that the applied method may be used to synthesize VO_x films with controllable stoichiometry in the range $0.5<x<2.45$.

Films with stoichiometry $x<1$ ($VO_{0.53}$ in Figure 2.2.4) are called sub-oxides, i.e., oxides in which the electropositive element is more abundant than oxygen. Generally, only a severe temperature treatment (T>1000 K) under high vacuum allows obtaining vanadium sub-oxides [99,100] while using the SCBD method we are able to synthesize them at room temperature.

2.2.4 *3d* occupancy investigation: Auger $L_3M_{23}M_{45}$ spectroscopy

The stoichiometric vanadium oxides: VO, V_2O_3, VO_2 and V_2O_5 have nominally 3, 2, 1 and 0 *3d* unpaired electrons, respectively. Auger decays with one hole in the VB (i.e., of the form V $XYM_{4,5}$) probe the V *3d* partial density of states (DOS) and therefore can be linked to *3d* occupation number and to sample stoichiometry. The ideal Auger decay to probe the partial *3d* DOS is the V $L_3M_{45}M_{45}$, characterized by two holes in the valence band. Unfortunately, in vanadium oxides, this decay channel is obscured by the O K $L_{23}L_{23}$ Auger electrons, even for an extremely low amount of oxygen [101]. V $L_3M_{23}M_{45}$ Auger decay is experimentally observable and *3d* electrons give the main contribution to this channel [102,103].

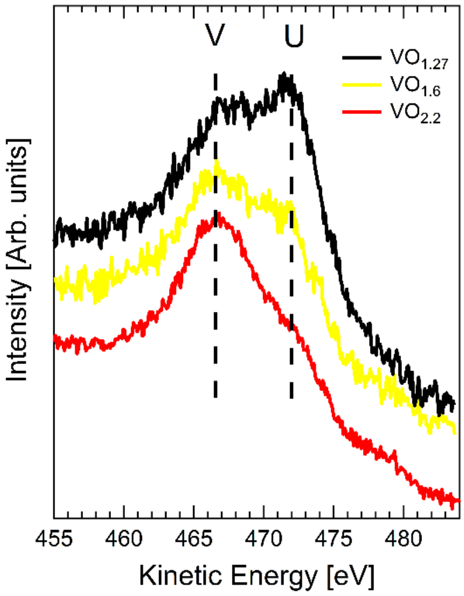

Figure 2.2.5: Comparison of Auger $L_3M_{23}M_{45}$ spectra of vanadium oxides NS films with stoichiometric ratio 1.27, 1.6 and 2.2 in the kinetic energy range 455-482 eV. The spectra are vertically shifted for clarity shifted in order to highlight the behaviour of features labelled U and V (see text).

As shown in Figure 2.2.5 the Auger $L_3M_{23}M_{45}$ of vanadium oxides exhibits two main features labelled V and U. As pointed out by Sawatzky and Post, these two components are correlated with the oxidation state[104]. Feature V becomes dominant as the oxidation state increases: it is related to V *3d* electrons covalently bound to O *2p* electrons. Feature U is associated with unpaired *3d* electrons. To extract quantitative information about the *3d* contribution in the VB, we fit the Auger V $L_3M_{23}M_{45}$ spectra using three pseudo-Voigt curves: one for feature V, one for feature U, and the last one for the small contribution from the O K L_1L_1 decay at ~477 eV. The background has been modelled using the Shirley curve. The Auger fraction (*U/(U+V)*) where *U* and *V* refer to the area of the two features), can be associated with the fraction of unpaired *3d* electrons relative to the total number of *3d* electrons. The behaviour of the Auger fraction vs. x is reported in Fig. 2.2.6 along with the best fit using a straight line.

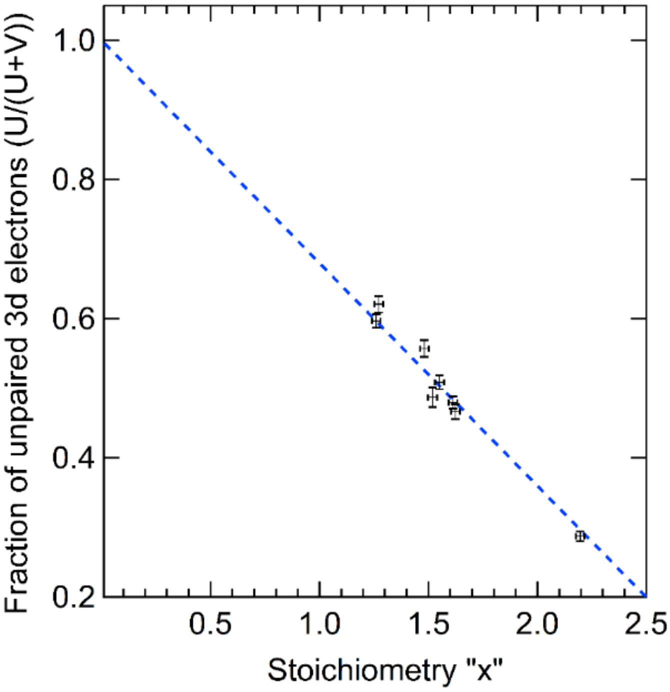

Figure 2.2.6: Correlation between stoichiometry and Auger fraction ($\frac{U}{U+V}$) as obtained by fitting the Auger $L_3M_{23}M_{45}$ spectra. The blue line is the best least-squares fit of the experimental data with a straight line of fixed intercept (at x=0 the fraction of unpaired electrons must be equal to 1). The best-fit slope is k = -0.320±0.005

In the pure metal, no oxygen atoms are available to form V-O bonds, thus $V = 0$ and $U/(U+V)=1$; accordingly, in the straight-line fit, the intercept is held at *1*. Likewise, in the maximum oxidation state (x=2.5) the fraction should be zero because no unpaired *3d* electrons are present and U=0. Actually, the extrapolated value for x=2.5 is different from zero: $U/(U+V)|_{2.5}=0.2\pm0.01$, denoting a partial *3d* occupancy. This is not unusual for $3d^0$ compounds because of the strong *3d-2p* hybridization in the specific case of V_2O_5, these results confirm previous published resonant photoemission (ResPES) experiments [105,106]. In Table 2.2 we report the number of unpaired *3d* electrons per vanadium atom equal to $3U/(U+V)$ under the above assumptions. They are not in good agreement with the occupation number calculated by Zimmerman and co-workers [107], suggesting that further theoretical investigations are necessary.

We would also like to underline here that using Auger spectroscopy, the investigated system, is the core-hole ionized system, and do not necessarily reflect neutral VO_x features. For example, while the extrapolated values are in good agreement with measured values of unpaired *3d* electrons for VO_2, suggesting that the core-hole effect in this oxide is negligible. On the other hand, the data for the V_2O_3 oxide suggest that only 1.56, instead of 2, *3d* electrons are unpaired. In this system, we point out the presence of a mixed band of *4s-3d* character near the Fermi level.

Table 2.2: Extrapolated values of the unpaired 3d electrons per vanadium atom.

Stoichiometric oxides (oxidation state)	# of unpaired *3d* electrons per V atoms (this work)	# of unpaired *3d* electrons per V atoms (Zimmerman et al.)	Nominal # of unpaired *3d* electrons per V atom
V_2O_5 (+5)	0.6 ± 0.04	1.3	0
VO_2 (+4)	1.08 ± 0.03	1.9	1
V_2O_3 (+3)	1.56 ± 0.02	2.6	2
VO (+2)	2.72 ± 0.02	-	3

However, for the V_2O_3 these results are not in agreement with Hard-X-Ray PES spectra which showed a VB with a pure *3d* character near the Fermi level and *4s* character centred at ~8 eV binding energy [108]. This suggests that in V_2O_3 the core-hole effect is relevant. For VO no data are available in the literature but a strong *4s-3d* hybridization is known to occur. To reproduce the VB features of this system using LCAO (Linear combination of atomic orbitals) and APW (Augmented Plan-Wave) computational methods, the electron configuration {V($3d^4 4s^1$) O($2p^4$)}, which implies a strong *4s-3d* hybridization [109–111], has to be considered. Moreover, in this case, the percentage of unpaired *3d* electrons has to be multiplied by four instead of three, obtaining the value of 2.72 ± 0.02 unpaired electrons.

2.2.5 Valence band study

Valence band spectra of vanadium oxides can be divided into two regions on the Binding Energy (BE) axis: the V *3d* (Fermi level - 2.5 eV BE, Figure 2.2.7 right panel,) and the O *2p* band (2.5 - 10 eV BE, Figure 2.2.7 left panel).

The V *3d* region is populated by unpaired *3d* electrons. The corresponding spectral feature shape and position depending on the oxygen amount present in the material, which determines the DOS via crystal field effects. The position of the V *3d* band highlights the metal character of sub-oxides, i.e., a finite DOS at the Fermi level. This characteristic points out that the amount of oxygen in these samples is not sufficient to break the degeneracy of *3d* levels [112] and for a theoretical band description the independent particle approximation is sufficient. V *3d* band of $VO_{1.27}$ clearly exhibits two features, one centered around 1.5 eV and a second at ~0.4 eV (indicated by arrows in Figure 4 right panel). These features can be correlated with the V^{3+} and V^{2+} components of the corresponding V *2p* core-level spectra. A small, but finite DOS at the Fermi level is also present, supporting the vanishing of the *3d* degeneracy. For higher values of the stoichiometric ratio, a decrease of the V *3d* band spectral weight is observed, which is transferred to the O *2p* band. An interesting case is represented by $VO_{2.45}$, a defective composition of V_2O_5, whose V *3d* band is populated due to oxygen vacancies. The latter generates V^{4+} ions, because of the large *3d-2p* hybridization [104,113].

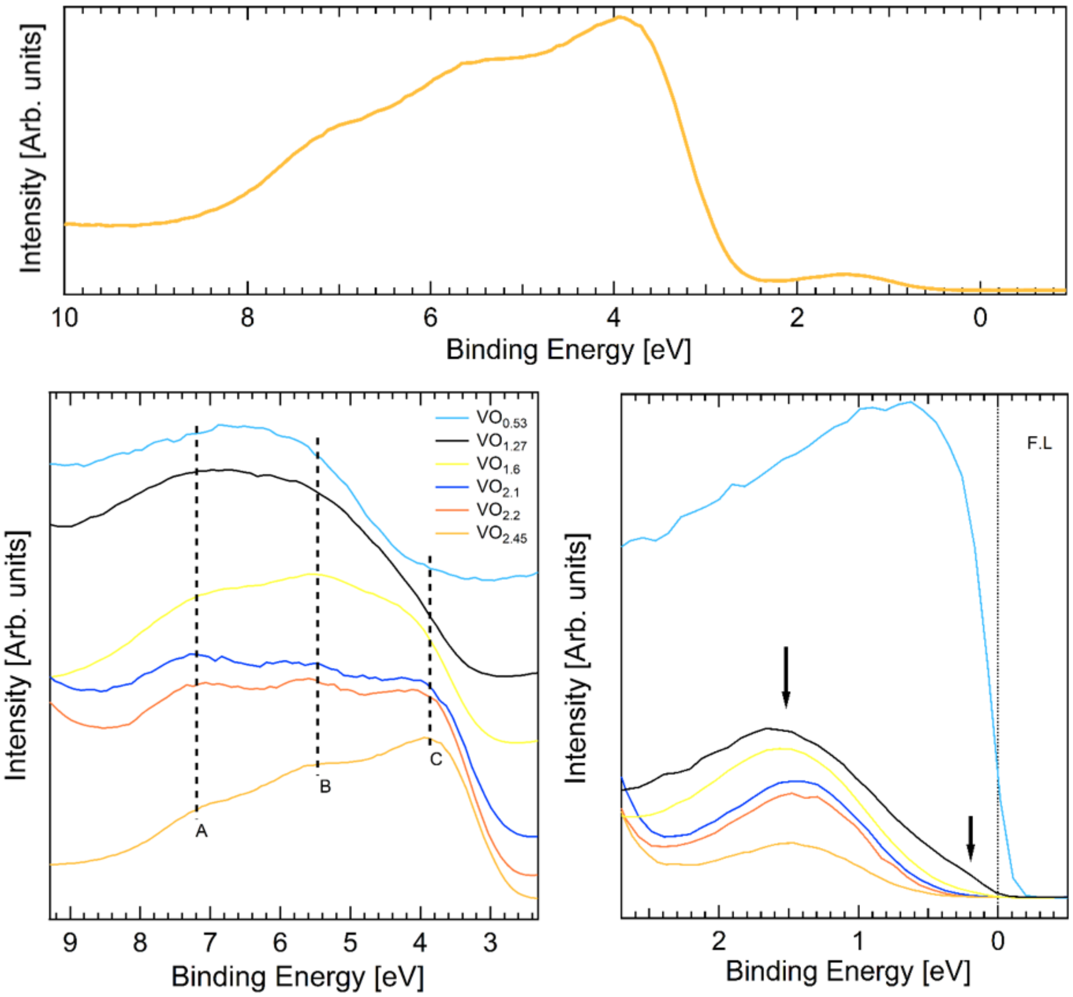

Figure 2.2.7: (Top) Representative full valence band spectrum of $VO_{2.45}$ in the BE region [0-10] eV. (Bottom) V 3d and O 2p regions of the valence band spectra for $VO_{0.53}$, $VO_{1.27}$, $VO_{1.6}$, $VO_{2.1}$, $VO_{2.2}$, and $VO_{2.45}$ oxides: (Left panel) Comparison of the spectra of the O 2p region. Spectra are vertically shifted in order to highlight the behaviour of the feature labelled A, B and C; (Right panel) comparison of the spectra in the so-called V 3d region, near the Fermi level (dotted line). The arrows point at $VO_{1.6}$ features. The intensity of the spectra is normalized to the maximum value of the O 2p region.

As shown in the left panel of Figure 2.2.7, the O *2p* region exhibits a fine structure due to the superposition of V *4s*, V *3d* and O *2p* orbitals. To describe qualitatively these VB features we use the LCAO band model terminology. For the high oxidation states, three features (labelled A, B and C) are clearly visible, which relative intensity evolves with the different stoichiometry. The A component is assigned to the superposition of V *4s* and O *2p* orbitals [108]. The DOS originating the B feature is dominated by the mixture of O *2p* and V *3d* orbitals, while the electron yield in the C region is dominated by the non-bonding O π* orbitals with a small contribution from V *3d* electrons [114,115]. For the samples with a lower oxidation state, the C feature decreases rapidly, while the relative intensities of A and B structures remain almost unchanged. For $x<1.6$, the π* contribution (C) is negligible and the spectral weight is centered on A and B with an inversion of their intensity ratio. This can be explained considering the behaviour of the atomic cross-sections and the number of V *3d* and O *2p* electrons. The only exception to the scenario described above is represented by the VB spectrum of the sub-oxide sample, which has its maximum between A and B and where no sign of the described features can be recognized. This intermediate feature could be pointing at a superposition of A and B, i.e. at a mixed *4s*-*3d* valence band.

Because of overlapping contributions from multiple orbitals [116], a quantitative analysis correlating VB spectral features to oxide stoichiometry is difficult. The fit of the spectral features with fixed line-shapes does not provide reliable quantities and their interpretation is questionable without a priori knowledge of the superposition degree of the contributing orbitals. To overcome this problem, we introduced a semi-empirical formula, which correlates the branching ratio of V *3d* and O *2p* bands with the stoichiometry.

The whole VB spectral intensity (O *2p* + V *3d*) can be decomposed as the sum of the partial intensities originating the A, B and C features, the contribution from unpaired V *3d* electrons, and the inelastic background. We write this sum as:

$$I_{O2p} + I_{V3d} = I_A + I_B + I_C + I_{V3d}^u + Bg \tag{2.2.10}$$

where $I_{O2p} + I_{V3d}$ is the numerical integration of the VB spectra in BE range from 0 to 10 eV, $I_{A/B/C}$ is the intensity of the features A, B, and C, I_{V3d}^u is the signal coming from unpaired *3d* electrons and Bg is the inelastic background.

As previously pointed out, each A, B and C features may represent multiple orbital contributions:

$$I_{O2p} + I_{V3d} = I_{V4s} + I_{O2p}^A + I_{V3d}^B + I_{O2p}^B + I_{O2p}^C + I_{V3d}^u + Bg \tag{2.2.11}$$

here I_{V4s} is the contribution given from V *4s* electrons to the overall intensity of the A feature and I_{V3d}^B is the intensity contribution supplied by V *3d* electrons to B peak. $I_{O2p}^A + I_{O2p}^B + I_{O2p}^C = I_{O2p}^t$ is the total signal generated by O *2p* electrons in the A, B and C features. Considering $I_{V3d}^B + I_{V3d}^u = I_{V3d}^t$ is the total signal associated with V *3d* electrons we may write:

$$I_{O2p} + I_{V3d} = I_{V3d}^t \left(1 + \frac{I_{O2p}^t}{I_{V3d}^t} + \frac{I_{V4s}}{I_{V3d}^t} + \frac{Bg}{I_{V3d}^t}\right) \tag{2.2.12}$$

Where the ratio $\frac{I_{O2p}^t}{I_{V3d}^t}$ is the ratio of the intensity generated by the total amount of O *2p* and V *3d* electrons. Assuming a constant efficiency of the analyser in the BE range of our interest, we can write [117]:

$I_{O2p}^t \; \alpha \; \sigma_{O2p} n_O$ and $I_{V3d}^t \; \alpha \; \sigma_{V3d} n_V$

where σ_{O2p} and σ_{V3d} are the cross-sections of O *2p* and V *3d* electrons, respectively and n_O and n_V are the atomic concentration of vanadium and oxygen in the sample. $\frac{I_{O2p}^t}{I_{V3d}^t}$ can be written as:

$$\frac{I_{O2p}^t}{I_{V3d}^t} = \frac{\sigma_{O2p}}{\sigma_{V3d}} x \tag{2.2.13}$$

in which $x = \frac{n_O}{n_V}$ is the stoichiometric ratio. The term $I_{O2p} + I_{V3d}$ becomes:

$$I_{O2p} + I_{V3d} = I_{V3d}^t \left(1 + \frac{\sigma_{O2p}}{\sigma_{V3d}} x + \frac{I_{V4s}}{I_{V3d}^t} + \frac{Bg}{I_{V3d}^t}\right) \tag{2.2.14}$$

the ratio $\frac{I_{V4s}}{I_{V3d}^t}$ is a numerical constant since:

$$\frac{I_{V4s}}{I_{V3d}^t} = \frac{\sigma_{V4s}}{\sigma_{V3d}} \frac{4s\ electrons}{3d\ electrons} = \frac{\sigma_{V4s}}{\sigma_{V3d}} \frac{2}{3} = 0.02104 = K_{sd} \tag{2.2.15}$$

σ_{V4s} is the cross-section of V *4s* electrons. Assuming a negligible background, in the V *3d* region of the VB spectra the only contribution comes from unpaired *3d* electrons, therefore we can write the outer-valence branching ratio as:

$$BR = \frac{I_{V3d}}{I_{O2p}+I_{V3d}} = \frac{P_{3d}}{\left(1+K_{sd}+\frac{\sigma_{O2p}}{\sigma_{V3d}}x+\frac{Bg}{I^{t}_{V3d}}\right)} \qquad (2.2.16)$$

$P_{3d} = \frac{I^{u}_{V3d}}{I^{t}_{V3d}}$ indicates the fraction of unpaired electrons in the film that we experimentally measure through Auger spectroscopy (see section 2.2.4).

$$P_{3d}(x) = 1 - 0{,}32x \qquad (2.2.17)$$

Therefore in the equation 2.2.18 the only unknown remaining variable is $\frac{Bg}{I^{t}_{V3d}}$. If we assume a linear dependence from the stoichiometry, of the form $ax + b$ we may write the new equation for the BR:

$$BR = \frac{I_{V3d}}{I_{O2p}+I_{V3d}} = \frac{1-0{,}32x}{\left(\frac{\sigma_{O2p}}{\sigma_{V3d}}+a\right)x+1+K_{sd}+b} \qquad (2.2.18)$$

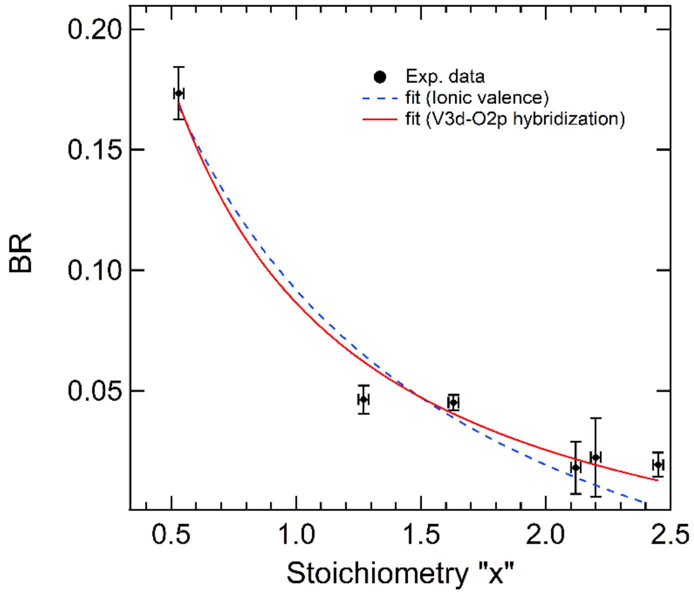

Figure 2.2.8: BR as a function of the stoichiometric ratio. The red curve is the fit obtained using the eq. 2.2.18 including the 3d-2p hybridization term; the blue dotted curve is obtained considering the ionic model of the valence band in which: $P_{3d}(x)=1$ for $x<1$ and $P_{3d}(x)=-0.6667x+1.6667$ for $x\geq1$.

BR experimental data have been extracted from the valence band spectra by integrating the V *3d* and the O *2p* regions to obtain I_{V3d} and I_{O2p} respectively. In Figure 2.2.8 the BR values from the full set of samples are displayed and compared with the best fit obtained from equation 1 (red curve) using a and b as free parameters (a= 4.5±0.7 and b= 0.5±0.6 in Figure 2.2.8). The good agreement among the experimental points and the fit supports the use of the proposed model for stoichiometry quantification using UPS and once more it underlines the failure of the ionic picture model to describe the valence features of vanadium oxides.

2.2.6 Vanadium oxides Work Function

In vanadium oxides, the WF values increase with the oxidation state ranging from 4.3 eV for pure vanadium up to ~7 eV for stoichiometric V_2O_5[118].

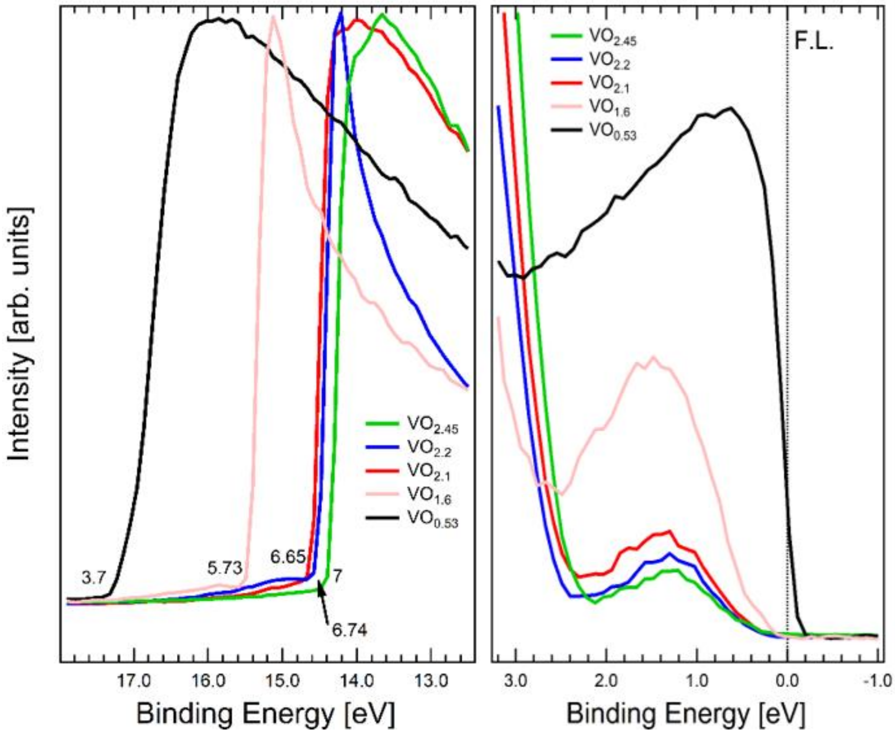

Figure 2.2.9: Left panel: comparison of the secondary electron onset collected with the He I (21.22 eV) discharge lamp for the following NS samples: $VO_{0.53}$, $VO_{1.6}$, $VO_{2.1}$, $VO_{2.2}$, and $VO_{2.45}$. For each film, the relative WF is also given. Right panel: VB feature near Fermi level (dotted vertical line). The spectra are normalized to the maximum of the secondary electron edge.

Despite during a photoemission experiment only the analyzer WF enters in the conservation of energy, carefully aligning the VB spectra it is possible to extract the sample WF (see Appendix 1 for more details). The measurements of the WF of these films have been performed measuring the VB spectra (see Figure 2.2.9) after negatively biasing the sample by ~-9 V to measure the secondary electron onset. The WF has been calculated as:

$$WF = hv_{He\ I} - BE_{So}$$

where BE_{So} is the binding energy corresponding to the secondary electron onset and $hv_{He\ I}$ is the photon energy of the helium lamp (21.22 eV).

The dependence of WF from stoichiometry in these NS vanadium oxides films is depicted in Figure 2.2.10.

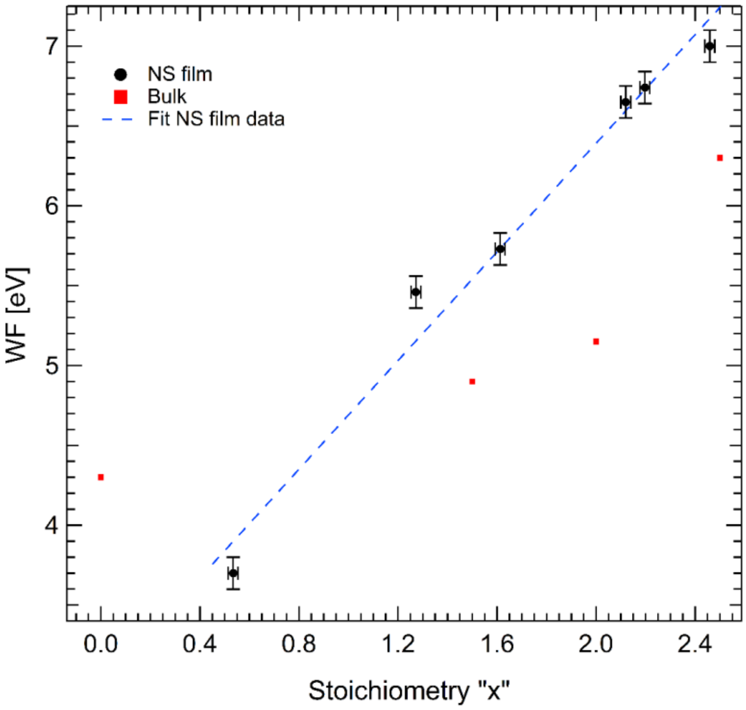

Figure 2.2.10: Comparison of the WF of VOx NS films (dots) with bulk data taken from the literature [118–121] *(squares) for the stoichiometric ratio x in the range 0.4-2.5. The broken line is the best fit for the NS films data.*

Data of NS films can be fitted by a straight line of the form:

$$WF = w_0 + w_1 x \tag{2.2.19}$$

Where the slope has a value of w_1=1.7±0.13 eV and the intercept is w_0=2.99±0.23 eV. For samples with x<0.76 the WF is smaller compared to the one of pure vanadium, most likely owing to the arrangements of vanadium and oxygen atoms in suboxides that determine a thin electron depletion layer on the surface of the sample. As demonstrated by Leung and co-workers, WF modifications induced by electronegative elements depend on the fine details of the electron density at the surface, which may lead to a decrease in the work function of metal oxides [122].

The low WF of suboxides could be extremely useful if they are used as an electron injection layer in Organic Semiconductor Devices, e.g. in Organic LED (OLED) the optimization of the cathode WF may increase the device efficiency [123]. Some experimental and extrapolated WF values are listed in Table 2.3, together with available data in the literature for bulk samples. Extrapolated and measured values of the WF of NS films are systematically larger respect to the bulk counterpart. This may be due to a size effect, which determines the enhancement of the electronic density by confinement within the nanostructure. It is well known since the 80's that the WF of small spherical nanoparticles is larger than that of bulk [124–127].

Table 2.3: WF values of NS films and reference bulk materials taken from the literature[112,119–121]. *The extrapolated values are labelled by *. The NP diameters have been obtained using the equation 2.2.20.*

Oxide	NS film WF [eV]	Bulk WF [eV]	NP diameter [nm]
$VO_{2.45}$	7±0.1	6.3[119]	1.54±1.2
$VO_{2.2}$	6.74±0.1	-	-
$VO_{2.1}$	6.65±0.1	-	-
VO_2	*6.39±0.33	5.15[121]	0.87±0.34

$VO_{1.6}$	5.73±0.1	4.65[120]	0.83±0.28
V_2O_3	*5.61±0.29	4.9[112]	1.71±1.15
$VO_{1.27}$	5.46±0.1	-	-
$VO_{0.53}$	3.7±0.1	-	-

Zhou and Zachariah deeply investigated the size dependence of the WF of aggregated NP [127]. They claimed that for assembled NP, the deviation respect to the bulk strongly depends on the size of the primary particles and weakly from the size of the aggregates. Assuming that the fundamental units of the nanoparticle-aggregates are spherically shaped, using the eq. 2.2.20 it is possible to estimate the average diameter of each element:

$$WF_{np} = WF_{bulk} + \frac{1.08}{D_{np}} \tag{2.2.20}$$

WF is expressed in eV and the diameter (D_{np}) in nm. Eq. 2.2.20 cannot provide an accurate size evaluation since the spherical shape approximation is too general and is not adequate to describe the complex shape-size relation. Indeed, a fractal-like nanostructured distribution is showed by in our samples (Figure 2.2.11). Still, the results of Eq. (2.2.20) can be indicative of the order of magnitude of the nanoparticles size. The diameters listed in Table 2.3, suggest that the main components have a size of the order of 1-2 nm, in agreement with the few nm particles observed in TEM images. In addition, the calculated diameters for different stoichiometries are similar, within the uncertainty. The result suggests that the nanoparticles nucleation conditions within the PMCS are not heavily affected by the small amount of oxygen present in the gas mixture, i.e. the size and shape are not depending by nanoparticles stoichiometry, as confirmed by TEM. The observation of such size effect in WF measurements, is an addtitional confirmation that that NS films synthetized with the SCBD grow without coalescence retaining the memory of the small size of their gas-phase precursors [80,91–93,128]. As a consequence of this "memory effect" SCBD allows to exploit quantum confinement to synthetize samples with a remarkably high WF and a low stoichiometry without any sputtering process or additional heating treatment.

An interesting case is that of suboxides. Despite the quantum confinement enhancement, for $x<0.76$ the WF of the films is smaller compared to the one of pure bulk vanadium, most likely owing to the arrangements of vanadium and oxygen atoms in suboxides that determine a thin electron depletion layer on the surface of the sample. As demonstrated by Leung and co-workers, WF modifications induced by electronegative elements depends from the fine details of the electron density at the surface, which may lead to a decrease of the work function of metal oxides [122].

The low WF of suboxides could be extremely useful if they are used as electron injection layer in an OSD, since as in OLED the optimization of the cathode WF may increase the efficiency [123,129]. We would like to point out that the straight line trend of Eq. 2.2.20 is not valid for $x=0$. Vanadium bulk WF is 4.3 eV, therefore, because of the above mentioned considerations on quantum confinement, for nanostructured vanadium we expect a WF>4.3 eV. This implies that exists a point $x*$ for which the WF will start to increase, reducing the stoichiometric ratio thus disobeying the linear relation of Eq. 2.2.20.

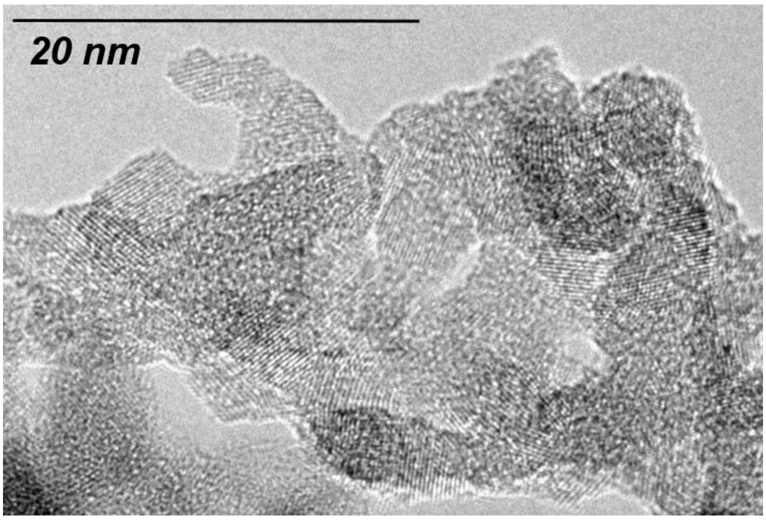

Figure 2.2.11: TEM image of the nanoparticle assembled nanostructured film for $VO_{2.2}$.

In order to investigate the morphology of nanoparticles deposited by SCBD, a deposition of 0.3 sec has been performed on a TEM grid with amorphous C supporting film. In Fig. 2.2.11 the TEM image is shown for $VO_{2.2}$. Even though the nanoparticles aggregate into nanoparticle agglomerates, it is still possible to clearly distinguish them. The intense agglomeration of nanoparticles even after few second deposition makes TEM images unsuitable for accurate size distribution analysis. Still, the size of the nanoparticles can be assessed in the range 3-6 nm for most of them. No large differences have been observed for samples with different deposition parameters.

2.2.7 Structural characterization: V $L_{2,3}$ and O K edge XANES

As mentioned in Chapter 1, structural properties are crucial in vanadium oxides based materials. Raman spectroscopy has been used to characterize the lattice order of the VO_2 NS sample produced with the PMCS. Unfortunately, the measurements have been inconclusive, most likely because for nanoparticles assembled films the Raman effect cross-section is extremely low[20]. The structure of the NS samples has been investigated by X-Rays Absorption Near Edge Structure (XANES) spectroscopy. An extended explanation of the XANES technique and of the different acquisition methods can be found in Appendix 2, in this section, a brief overview is proposed.

XANES concerns the electronic transitions from core shells to unoccupied states following a photo-absorption process.

To characterize the VO_x NS samples we studied XANES spectra of the V $L_{2,3}$ and O K edges acquired in Total Electron Yield (TEY).

The XANES measurements have been performed on the Circularly Polarized beamline of Elettra synchrotron radiation facility using the CryoAlp UHV experimental chamber[130]. To perform in-situ XANES measurements the experimental chamber has been coupled to the PMCS and equipped with an XYZ manipulator as depicted in Figure 2.2.12a. In this experimental scheme, the supersonic cluster beam produced by the PMCS is deposited in-situ on a copper plate which is electrically isolated from the rest of the experimental chamber. TEY spectra have been acquired measuring the drain current as shown in Figure 2.2.12b connecting to ground the sample through a Keithley 486 picoammeter. The angle between the incident photons and the sample surface was 45±5°; the base pressure of the experimental chamber was $1*10^{-9}$ mbar, operating the PMCS the pressure raised to $\sim5*10^{-9}$ mbar because of the carrier gas injected by the cluster source.

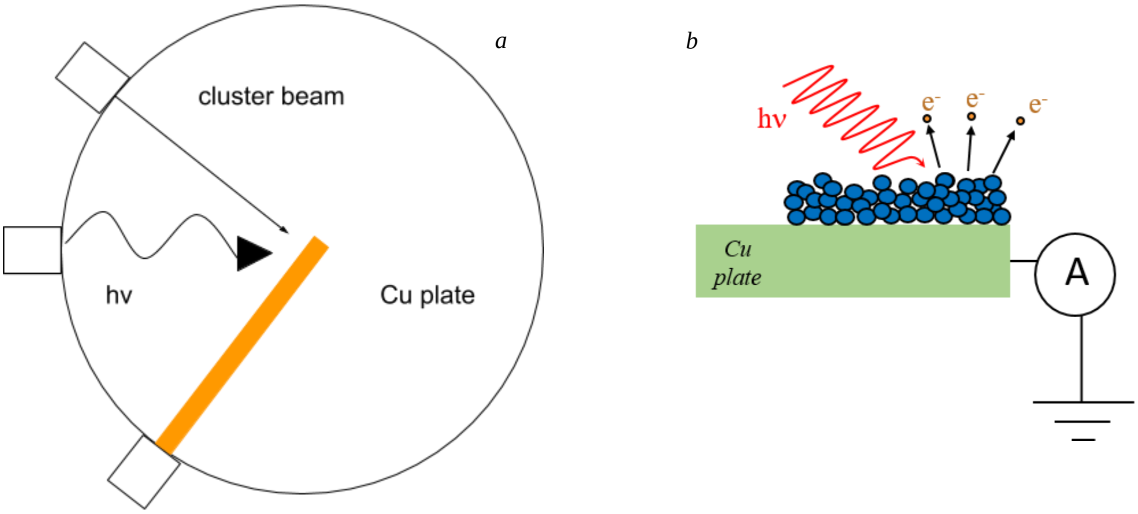

Figure 2.2.12: a) Schematic scheme of the experimental setup; b) TEY acquisition scheme

To synthesize samples with different stoichiometry, we fed the PMCS with an Ar-O_2 gas mixture with an O_2 molar percentage in the range of 0-1.25 %. The working parameters of the PMCS have been adjusted in order to maximize the deposition rate (delay between gas injection and discharge firing = 0.51-0.64 ms; discharge operating voltage 0.9 kV; discharge duration 60 µs despite elsewhere specified; pulsed-valve aperture driving signal duration time 196-220 µs; pulse repetition rate 3 Hz; Ar-O_2 pressure feeding the Parker valve 60 bar).

The XANES spectra acquired across the V $L_{2,3}$ and O K edges for different VO_x samples are depicted in Figure 2.2.13a. It is clearly observable the appearance and evolution of different features of the O K edge as x increases. Increasing the samples stoichiometry a blue shift of the L_3 maximum is also observed.

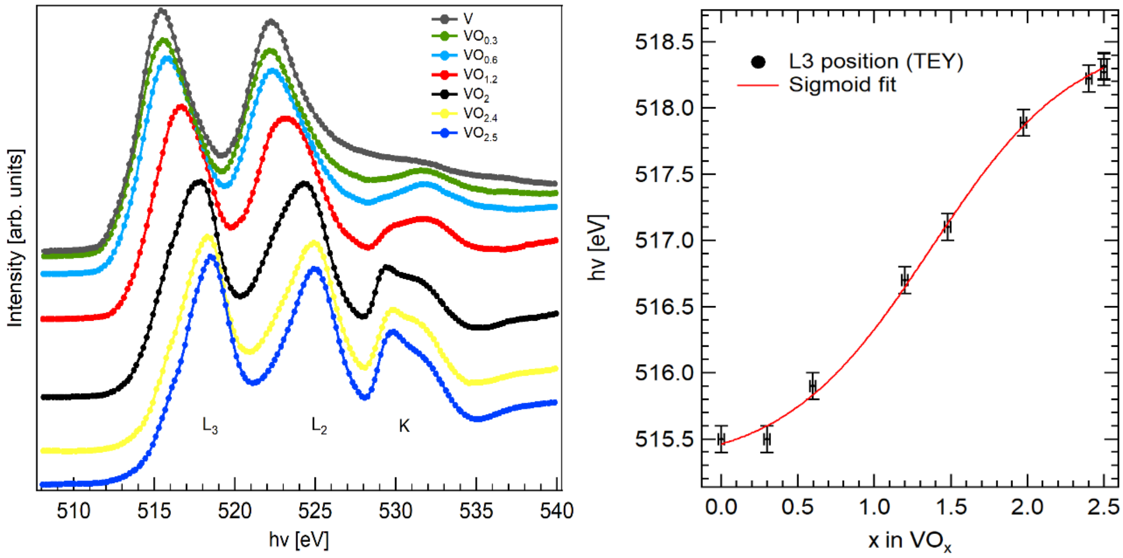

Figure 2.2.13: a) XANES spectra of V $L_{2,3}$ edges and O K edge for different VO_x samples in the photon energy range 508-540 eV. b) Dependence of the energy position of L_3 resonance as a function of stoichiometry (black dots), the continuous red line is the best fit of the data (sigmoid line shape).

The L_3 maximum position evolution as a function of the oxidation state has been previously observed and a linear relationship has been proposed in order to explicit the stoichiometry dependence of L_3 and L_2 edges[131]. However, the data depicted in Figure 2.2.13b are best fitted by a sigmoid function. The sigmoid used to fit the data is of the form:

$$f(x) = base + \frac{max}{(1+e^{\frac{-(x-x_0)}{r}})} \tag{2.2.21}$$

Where *base*=515.28 ± 0.15 eV, *max*=3.3 ± 0.27 eV, x_0=1.37± 0.06, *r*=0.47 ± 0.08.

The discrepancy with the linear trend reported in the literature [131] can be explained with the unique ability of the PMCS to synthesize sample with an ultra-fine control over stoichiometry. In fact, by coupling the PMCS with an experimental apparatus able to perform an *in-situ* investigation, it was possible to discriminate between pure vanadium and vanadium sub-oxide ($VO_{0.3}$). This allowed us to improve from the linear to the sigmoid dependence of the V L_3 energy position on stoichiometry, thus upgrading the oxidation state identification accuracy using XANES spectra. Further theoretical investigations are necessary in order to better understand the sigmoid behavior observed in our data.

In general, the shape of O K edge XANES features in transition metal oxides is mostly determined by hybridization, final state spin configuration and crystal field effects[132,133]. The O K edge evolution as a function of stoichiometry is extremely interesting in order to study the chemical environment surrounding vanadium atoms, in terms of crystal field splitting and metal-ligand hybridization. In VO_x, O atoms arrange in octahedral geometry around a vanadium centre generating cubic crystal field[134] which splits the degenerate *3d* manifold into 3 t_{2g} and 2 e_g levels. Because of the *3d-2p* hybridization, the energy levels are a superposition of *p* and *d* electrons, thus the contribution of the hybridized t_{2g} and e_g levels in the empty DOS can be observed in the O K edge XANES spectra. As can be seen in Figure 2.2.14 O K edge XANES exhibits two main contributions at~ 532 eV and ~529.6 eV which invert their intensity ratio increasing the oxidation state.

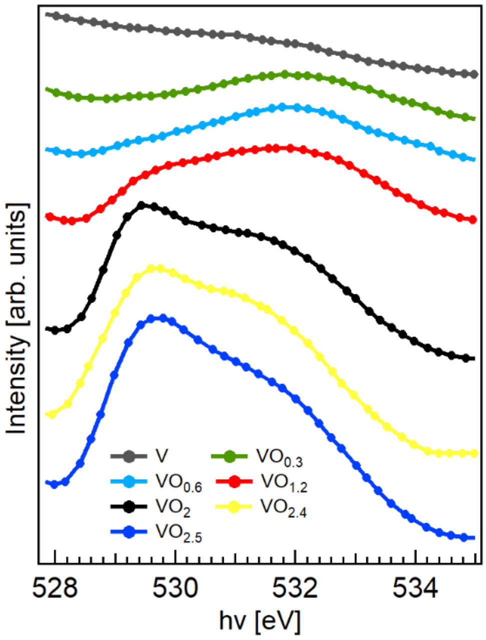

Figure 3.2.14: O K edge XANES spectra of VO_x samples in the hv region 528-534 eV.

The high energy feature can be linked to the e_g* level while the low energy feature to the t_{2g}*[133]. It is observable that a small amount of t_{2g} character due to hybridization with O-*2p* electrons is present in $VO_{0.6}$ (small feature at hv ≈ 529 eV) confirming our Auger investigation which predicts a mixed *4s-3d* valence band for sub-oxide. Increasing the oxygen content the t_{2g}-O*2p* hybridization increase with an inversion of the intensity for x~1.5[113,131–133].

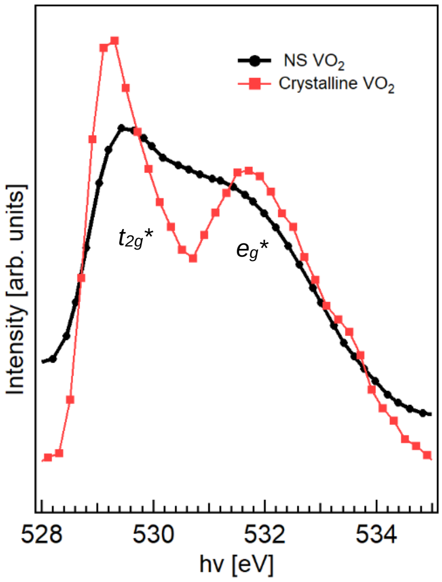

Figure 2.2.15: Comparison between the O K edge of the NS VO_2 sample and a crystalline sample of 16 nm thickness in the energy region 528-535 eV

As can be observed in Figure 2.2.15, there is a huge difference between the crystalline VO_2 and the NS sample O K edges. For the crystalline spectra, the t_{2g}* and e_g* contribution are well separated pointing out a strong crystal field effect, and therefore a well-ordered lattice. Also, the NS film exhibits t_{2g}* and e_g* features but they are broader and less separated. In comparison with the crystalline sample, the t_{2g}* contributions are shifted toward higher photon energies while the e_g* toward lower photon energies. This is strong evidence of a distortion of the oxygen octahedron surrounding the V atom compatible with the bending of two opposite vertex which lifts the t_{2g}* and lowers the e_g* energies[135,136] revealing that the NS samples are disordered. However, in high magnification TEM images a crystalline lattice is in some cases observed (see Fig. 2.2.11), which is ascribed to crystallization of amorphous material under the high energy TEM electron beam.

Additional information about the electronic structure of NS films can be extracted studying the L_3/L_2 branching ratio. In an ideal system, the L_3/L_2 branching ratio should be 2, but for early TM atoms, strong deviations from the expected value have been observed[137]. In XANES measurements at L edges the excitation *2p->3d* allows us to probe the *3d* partial unoccupied DOS. However, the *2p* core-hole (*2p*) effect over the valence band electron is not always negligible. A strong *2p-3d* interaction leads to deviation from the ideal XANES behaviour: e.g. apparent reduction of the spin-orbit coupling, deviation of the L_3/L_2 branching ratio from the statistical value etc.[137]. Moreover, in pure metallic isolated clusters, it has been demonstrated that particle size influences the valence electronic structure and therefore the core-hole screening ability, which results in a size-dependent L_3/L_2 branching ratio[138]. Since SCBD is a low kinetic energy deposition technique, the NS films grow without coalescence phenomena, therefore clusters retain their individuality (see section 2.2.2 and 2.2.6). As a consequence, a deviation in the L_3/L_2 branching ratio is expected in the XANES spectra of pure metallic NS film, which indeed has been observed in the L_3 and L_2 spectra of pure vanadium NS film (see Figure 2.2.16).

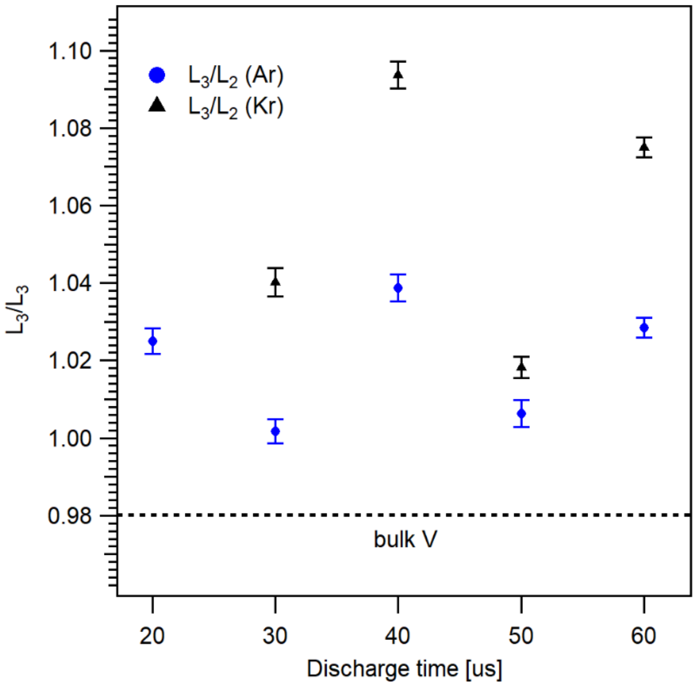

Figure 2.2.16: L_3/L_2 branching ratio for pure metallic NS films as a function of the discharge time and carrier gas type (Ar, Kr). The dashed lines represent the L_3/L_2 bulk value taken from [139].

In Figure 2.2.16 a deviation of L_3/L_2 respect to the bulk value[139] as a function of discharge time is clearly observable. The discharge time is the duration of the time interval of cathode ablation.

This directly affects the number of vaporized atoms within the ceramic cavity and therefore the number of atoms available to trigger the nucleation process. Changing the discharge time means modifying the nucleation conditions which may lead to the synthesis of clusters with different size-shape relations, and this can explain the modulation of the L_3/L_2 branching ratio. Another way to influence the synthesis condition is to choose a different carrier gas. The carrier gas substantially influences the residence time of ablated atoms within the ceramic cavity and the cluster terminal velocity.

In Figure 2.2.16 the measured L_3/L_2 branching ratio for nanostructure V synthesized using Ar (blue circle) and Kr (black triangle) as a function of the discharge time is shown.

The spectra acquired using Kr as carrier gas exhibits systematically higher L_3/L_2 branching ratio respect to the sample synthetized using Ar. This effect may be related to the difference residence time within the cluster source which can result in the production of clusters with different shape-size relation.

To understand the influence of the synthesis parameters over the clusters shape and size, screening ability and, finally, over the L_3/L_2 branching ratio, further theoretical and experimental investigation are necessary. However, measuring the L_3/L_2 branching ratio, it has been experimentally demonstrated that the NS films produced using SCBD retain a memory of their gas-phase precursors. Moreover, tuning the discharge time, to produce NS films with different screening abilities it is possible.

In conclusion, we demonstrated that to control the oxidation state of the NS VO_x film it is possible using a PMCS without further post-deposition treatment. Because of this, we could study the *3d* occupancy, VB branching ratio, and the WF as a function of stoichiometry.

3d occupancy yields a linear relation with stoichiometry, with evidence of strong *3d-2p* and *3d-4s* hybridization. VB branching ratio can be modeled applying a heuristic approach, underlying the failure of the ionic picture to describe the VB feature. Also, the WF exhibits a linear dependence from stoichiometry. Moreover, an increase in the WF respect to bulk samples due to quantum confinement is observed. This is strong evidence that the NS films are assembled by clusters that aggregate without coalescence confirming our previous considerations on the kinetic energy per atom (~0.1 eV) at the moment of deposition using Ar as the carrier gas.

Finally, we demonstrated that XANES spectra can be used to probe samples stoichiometry and that studying the O K edge XANES feature it is possible to extract important structural information. The VO_x samples produced by the PMCS are disordered without long-range periodicity. The ability to synthesize completely disordered samples is of fundamental importance in the study of the VO_2 MIT since it allows us to investigate a system in which the Peierls distortion mechanism is quenched and to observe only the electronic contribution to the MIT.

Chapter 3.

Electronic structure investigation of VO_2/TiO_2 thin films and VO_2 nanostructured films: Auger yield and ResPES

In this chapter, the VO_2 MIT will be studied in order to disentangle the different degrees of freedom contributions: orbital, lattice and electronic. With this aim, we studied four different samples: three crystalline samples of VO_2/TiO_2 (thickness 8, 16, 32 nm) and one sample of disordered nanostructured VO_2. By studying samples with different lattice parameters, it is possible to correlate the changes of the electronic properties (e.g. $d_{||}^{*}$ and π^{*} orbitals) with the sample structure. In order to extract detailed information on the electronic structure, the DOS, as well as the empty DOS, need to be investigated. ResPES and XANES are two invaluable tools, which probe with element selectivity the local chemical environment of the samples. The experiments were performed at the ANCHOR end-station of the ALOISA beamline [140] at Elettra synchrotron radiation facility. For XANES (acquired in Auger electron yield mode) and ResPES acquisitions, electrons were collected at normal emission with the photon beam linearly polarized in the scattering plane and impinging the sample at the magic angle (35°). A PSP Vacuum 120 mm electron analyser was used with a 2D delay line detector. Measurements were performed at constant pass energy (E_p=20 eV) with an overall resolution of 0.25 eV.

3.1 Auger Electron yield X-ray Absorption Spectroscopy

To probe the local structure and the empty DOS of our samples, we performed XANES measurements in Auger electron yield (AEY) mode collecting the V $L_3M_{23}M_{45}$ Auger electrons (kinetic energy= 464 eV) and the O $KL_{23}L_{23}$ Auger electrons (kinetic energy= 507 eV) which are shown in Figure 3.1.1.

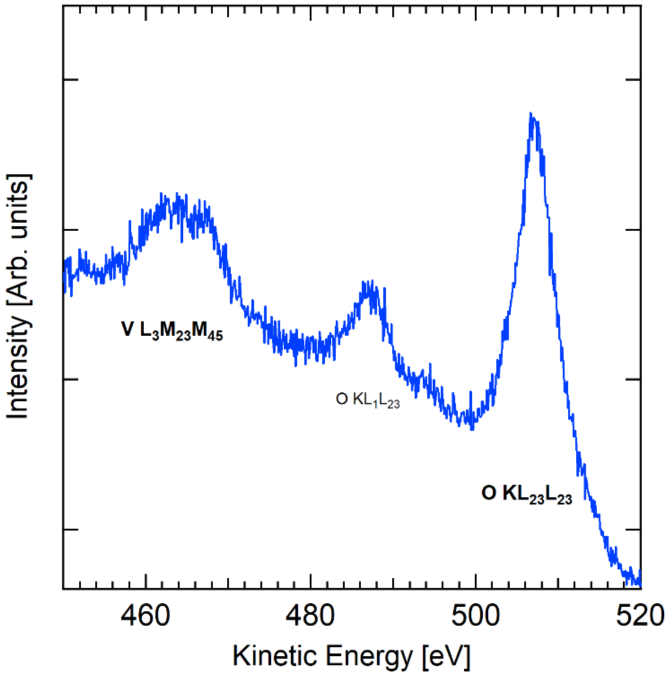

Figure 3.1.1: Auger electrons of the NS sample (90°C) in the kinetic energy range 450-520 eV. The spectrum has been acquired at hv=650 eV.

This choice guarantees to probe the sample with improved chemical and surface sensitivity with respect to other methods[141]. Although the Auger Electron Yield technique has the smallest signal rate, it offers the largest S/N ratio among all electron-yield techniques [142]. As will be discussed in the next section, the V $L_3M_{23}M_{45}$ Auger is most suitable to study the vanadium $L_{2,3}$ edges while O $KL_{23}L_{23}$ Auger yield gives more information about the oxygen K edge [142].

3.1.1 Auger Yield O $KL_{23}L_{23}$

MIT is described as passing from the insulating to the metallic phase. The XANES spectra of the insulating phase have been acquired at 30°C while those in the metallic phase at 90°C.

Crystal field effects, V *3d*-O *2p* hybridization, and Peierls distortion mostly define empty DOS and DOS features of VO_2. The 3 t_{2g} and 2 e_g levels orbitals recombine with the O *2p* orbitals creating the O *2p* and V *3d* region of the valence band in the DOS (see section 2.2.5) and the empty bands π*, $d_{||}^*$(t_{2g} character) and σ * (e_g character) in the empty DOS. The $d_{||}^*$ is directed along the c_r axis in the metallic phase, and along the V-V dimer in the insulating phase and it is strictly related to the unidimensional V-V dimers chain formation in the monoclinic insulating phase[61], while the π* is more isotropic within the lattice[62].

Across the MIT the π*and $d_{||}^*$ collapse to the Fermi level closing the bandgap. Since π*, $d_{||}^*$ and σ* orbitals have mostly *3d* character, the changes on the electronic structure can be characterized by the V L edges (V *2p* -> *3d*). Nevertheless because of the strong hybridization between V *3d* and O *2p* electrons, probing the π*, $d_{||}^*$ and σ* bands is also possible by measuring the O K edge[135,142,143]. As vanadium L edges (~512-527 eV) and oxygen K edge (~530 eV) are extremely close in photon energy, there is no doubt that the shape of the O K edge is affected by the tail of the L_2 (see Figure 2.2.13). As reported in Figure 3.1.2 using the Auger yield (O $KL_{23}L_{23}$) we managed to minimize the vanadium contribution enhancing in the XANES spectra the signal from the oxygen.

Respect to TEY spectra, the oxygen signal is ~ 4 times more intense respect to the V L edges signal, minimizing the shape distortion due to the presence of L_2, allowing a better analysis of the changes occurred across the MIT. The V L edges signal in Figure 3.1.2 is generated by the Auger decay V $L_3M_{45}M_{45}$ which is much less intense than but unfortunately very close in energy (about 4 eV) to O $KL_{23}L_{23}$ decay [101,104]. The spectra are normalized respect to the maximum intensity of the σ* feature at 532.2 eV.

The 8, 16 and 32 nm films show intense and well-separated π* and σ* resonances at about 529.8 and 532.2 eV respectively which strongly confirm the local ordering of these films [135]. The $d_{||}^*$ band is not clearly visible but it appears to be positioned between 530.5 and 531 eV [135,143,144].

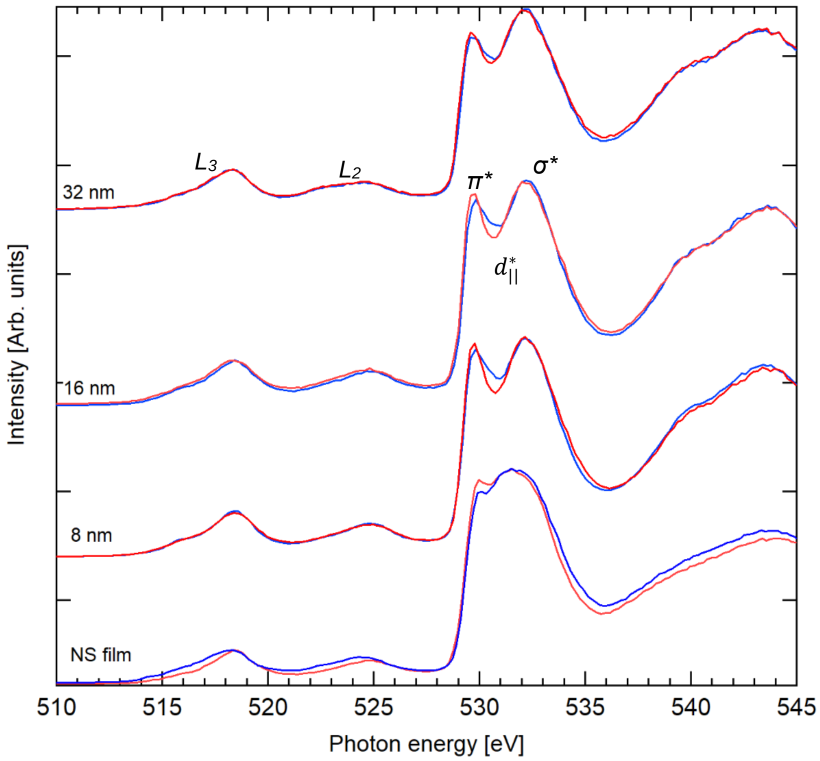

Figure 3.1.2: XANES spectra collected by Auger yield (O K $L_{2,3}L_{2,3}$) at the V L2,3 edges and at O K edge of VO_2 crystalline films of 32, 16 and 8 nm and of the nanostructured disordered film for both metallic (red, 90°C) and insulating (blue, 30°C) phases.

Across the MIT a slight increase of the π* intensity is observed (see Figure 3.1.3) concurrent with a depletion of the valley between π* and σ* which is compatible with the collapse at the FL of the $d^*_{||}$ band passing from the monoclinic to the rutile phase.

Coherently to what showed in Chapter 2, the nanostructured films do not exhibit a well-defined separation between π* and σ* resonances, in agreement with the disordered nature of the samples [135,136]. This is also supported by the shift toward lower energy by ~1 eV of the σ* band, which relative position respect to π* is directly related to the 10Dq crystal field intensity [145] and therefore to the structural order. Nevertheless across the MIT, spectral changes are observed.

Passing from the low temperature to the high-temperature phase, an increase of the intensity in the region of π* and partially of $d^*_{||}$ is observed for the disordered sample. The changes observed in Figure 3.1.3 are in the t_{2g}* energy region pointing out that, the main spectral changes across the MIT influence empty orbitals with t_{2g} character.

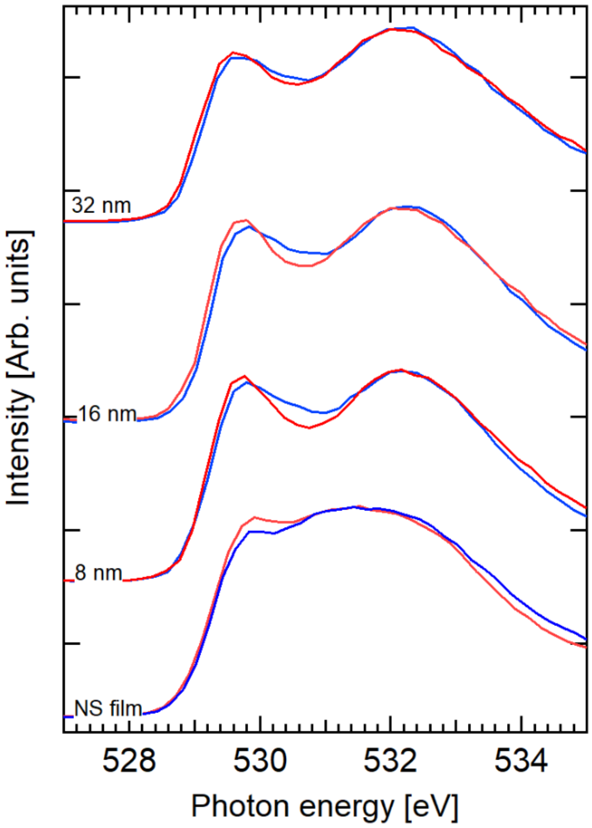

Figure 3.1.3: Comparison of the O K edge XANES (527-535 eV) of VO_2 *crystalline film of 32, 16 and 8 nm and the NS disordered film acquired in Auger yield (O K* $L_{2,3}L_{2,3}$*) for metallic (red) and insulating (blue) phases.*

For the strained samples, it is also observable that the deepness of the $d_{||}^{*}$ valley across the MIT increases decreasing the thickness. This could be related to modulations of the relative position of the π* and $d_{||}^{*}$ levels induced by the uniaxial strain along the c_r axis [62,64]. Because of this, in the insulating phase π* and $d_{||}^{*}$ tend to increase their splitting, with π* shifting towards lower photon energy as well as $d_{||}^{*}$ shifts towards higher photon energy. In the metallic phase, strain induces an inversion of the relative occupation of π* and $d_{||}^{*}$ at the Fermi Level. $d_{||}^{*}$ in the metallic phase refers to the empty part of the partially occupied $d_{||}$ band (see Figure 2.1.3). In bulk VO_2 the occupation of Fermi level is mostly $d_{||}^{*}$ with a small fraction of π*, while for strained and ultra-strained film the situation is reversed (see Figure 3.1.4) [62].

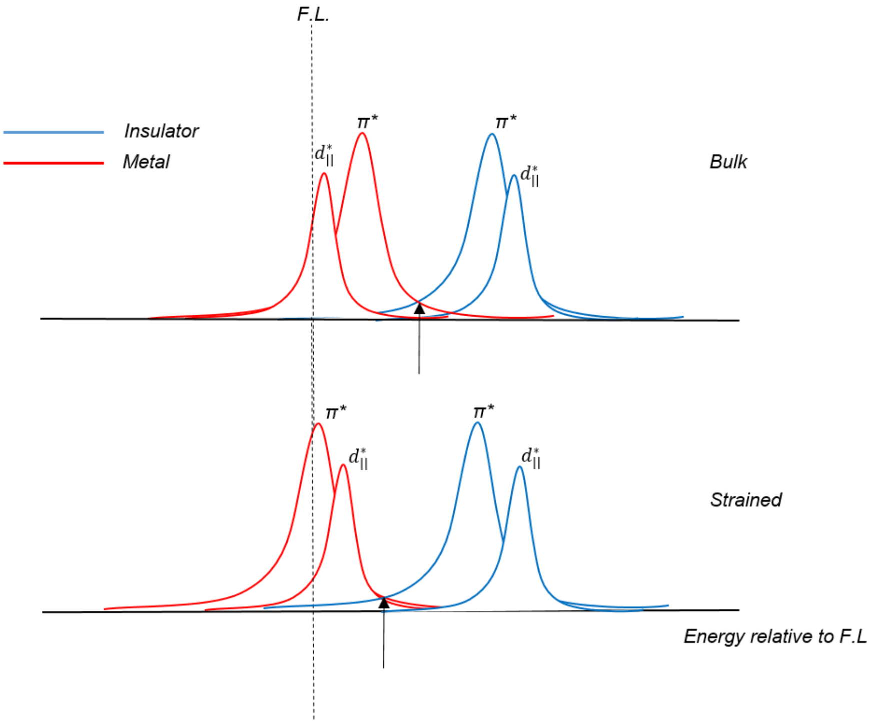

Figure 3.1.4 Schematic empty band model for bulk (top) and strained (bottom) VO_2 in the insulator (blue line) and metal (red line) phases. The intersection point (marked by arrows) between the insulator and metal empty DOS shifts toward lower energy for strained sample, because of the concurrent π^*, $d^*_{||}$ separation in the insulating phase and π^*, $d^*_{||}$ inversion in the metallic phase.

To investigate this strain modulated empty DOS evolution we studied the difference of the XANES spectra between the insulating and metallic phases.

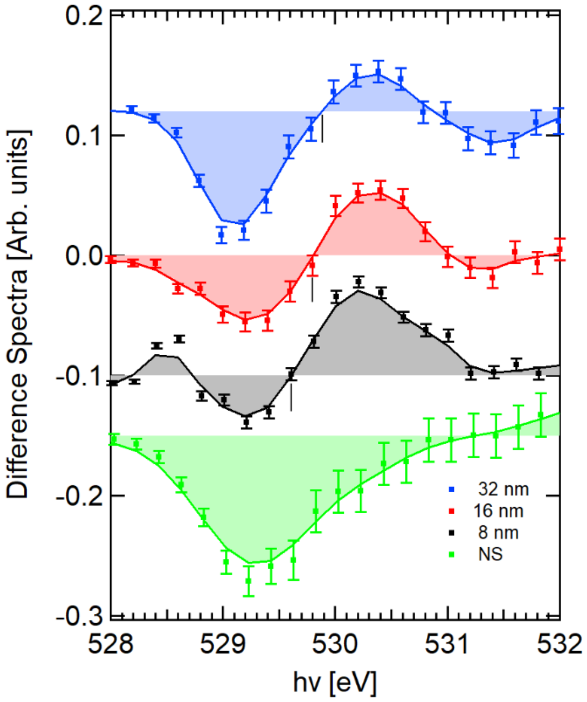

Figure 3.1.5: Comparison of the difference in the Intensity of the XANES spectra showed in Fig. 3.1.3 in the range hv: 528-532 eV. The dots represent the experimental points while the continuous line is the smoothed curve of the experimental points (binomial algorithm), which is used as a guide for the eye. From top to bottom: films of 32, 16

and 8 nm and the NS film. The black vertical lines indicate the turning point of the difference from negative to positive contribution. The spectra are vertically shifted for sake of clarity.

The differences among the XANES spectra are shown in Figure 3.1.5 and have been calculated as:

$$I_{ins} - I_{met} \propto uDOS_{ins} - uDOS_{met} \tag{3.1.1}$$

where I_{ins} and I_{met} are the intensity of the XANES spectra of the insulating and metallic phases and $uDOS_{ins}$ and $uDOS_{met}$ are the empty DOS, respectively. Using the Eq. 3.1.1 a negative contribution is expected in the spectral region in which the metallic empty DOS is more intense and vice versa, whereas a turning point (TP) from negative to positive contribution is expected where the metallic and the insulating empty DOS coincide. Some trends are evident for the spectral difference of the strained samples. As the strain increases the positive contribution in the hν range 530-531 eV grows with an asymmetry toward high photon energy, the negative contribution in the 528-529.7 eV also increases the TP shifts toward lower photon energy. The latter is a fingerprint of the shrinking of the metal empty DOS and a widening of the insulating phase empty DOS, therefore they will cross at lower photon energy. This is in agreement with the band description of Figure 3.1.4 and with the strain dynamics of π^*-$d_{||}^*$ bands in both insulating and metallic phases. This is further confirmed from the growing asymmetry in the positive contribution at 530-531 eV, which is compatible with the picture of the strain-induced increased separation between $\pi^*$and $d_{||}^*$ in the insulating phase. Also, the negative contribution decreases, increasing the strain, in agreement with the band model described before since the π^* band, which is almost empty in the metallic bulk phase but is heavily occupied in the strained films in our acquisition condition is more intense of the $d_{||}^*$.

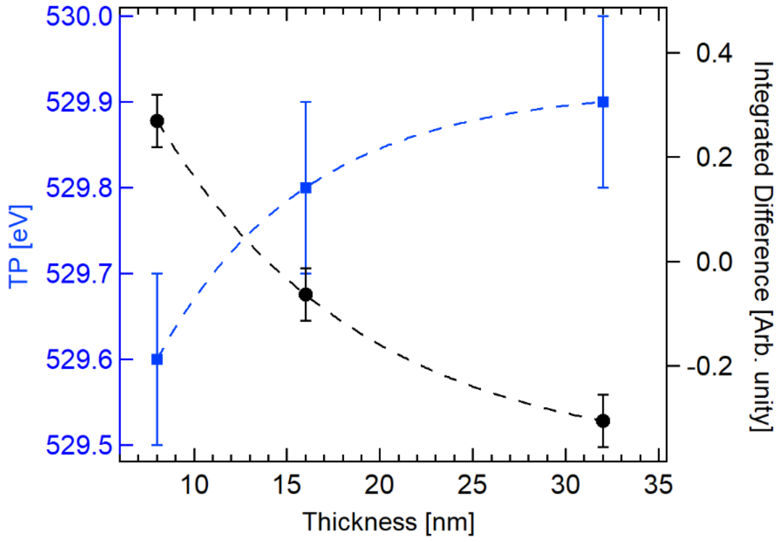

Figure 3.1.6: The Turning Point (TP) and Integrated differences as a function of the film thickness. The Integration of the differences has been performed using a trapezoidal algorithm and in the photon energy range 528-531 eV. The dashed lines are a guide for the eye.

The difference spectra changes and TP shift described above have been quantified as a function of sample thickness and reported in Figure 3.1.6. The black circles represent the integral of the difference spectra in the hν range (528-531 eV), the blue squares are the hν position of the TP. The Integrated difference trend is compatible with previous investigation of the empty DOS of strained VO_2 [62]. Nevertheless, the interpretation of the curves reported in figure 3.1.6 is not straightforward. By the way, TP and Integrated differences have a similar trend as a function of thickness, suggesting that these two quantities are correlated.

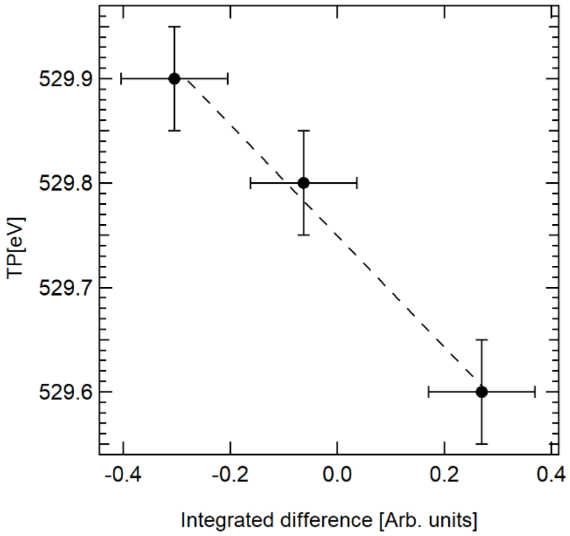

Figure 3.1.7: Correlation between Integrated intensity (x) and TP position (y). The data re best fitted by a linear relation of the form y=a+bx with a=529.75±0.01 and b=0.52±0.05.

From figure 3.1.7 it is observable that between TP shift and Integrated difference elapses a linear relation, pointing out that these two quantities are clearly commensurate. Further investigation is necessary to clarify this point.

Regarding the spectral difference of the NS film, it is evident the negative contribution whose minimum is aligned with the strained samples. Its intensity suggests a stronger dynamics of the π* band. This can be understood considering a partial Mott-melting of the π* band across the MIT in agreement with the literature,[13,38] suggesting the strong electron-electron repulsion as the MIT driving force in disordered samples [23,63,146,147].

3.1.2 Auger yield V $L_3M_{23}M_{45}$

As across the phase transition the most significant spectral changes occur around the Fermi level, it is important to have a selective probe with the ability to probe only *3d* electrons. As shown in section 2.2.4 Auger V $L_3M_{23}M_{45}$ can be used to probe the outer *3d* shell in vanadium oxides. Therefore using AEY and collecting the decay channel V $L_3M_{23}M_{45}$ is a good option to study the MIT [142]. The XANES spectra of the strained samples 32, 16 and 8 nm thick and the NS disordered sample are compared in Figure 3.1.8.

The spectral shape is similar for TEY spectra in which V L edges and O K edge intensities are comparable. This is due to the nature of the V $L_3M_{23}M_{45}$ Auger decay that probes unpaired ~~and~~ O *2p* hybridized *3d* electrons.

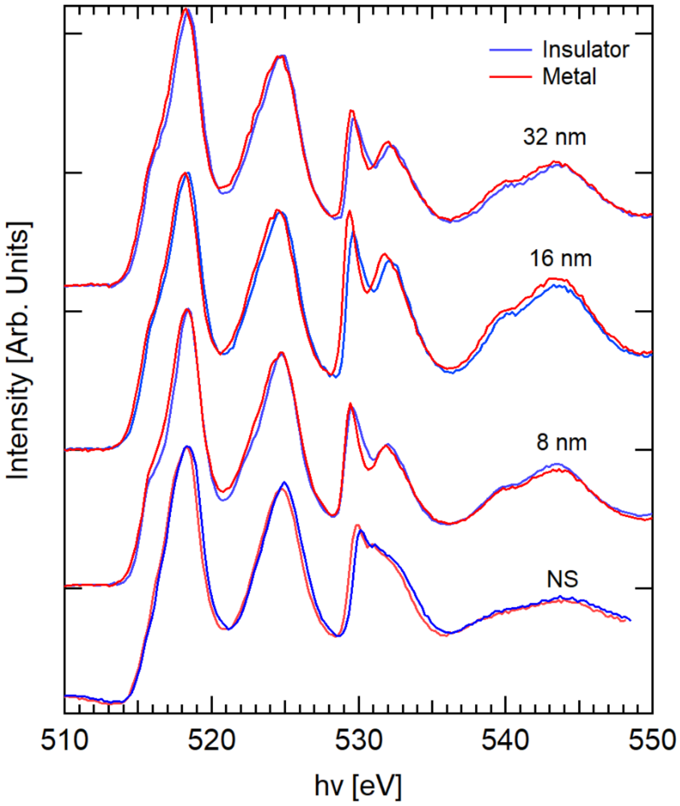

Figure 3.1.8: XANES spectra (Auger V $L_3M_{23}M_{45}$, 464 eV) in the hv range (510-550 eV) of the insulating (blue) and metallic (red) phase of different VO_2 samples. From top to bottom: strained samples of 32, 16, 8 nm and NS sample. The spectra have been normalized to the photon energy and to the L_3 intensity maximum

However, as discussed in section 3.1.1, the O K edge shape is modified by the V L_2 thus this decay channel is most suitable to study the behavior of the V L_3 and L_2 edges across the MIT. However, the interpretation of the L edges shape is not as straightforward as at the O K edge. The L_3 edge is more structured respect to the L_2 and, more, in general, the L_3 and L_2 spectra differ because of the multiplet effect in the final state [148]. In the VO_2 case, the multiplet contribution is not so important, whereas the presence of the strong Coster–Kronig decay (V $L_2L_3M_{4,5}$) [104] severely reduces the lifetime of the excited state $2p^1{}_{1\backslash 2}$ $3d^{n+1}$ and broadens the L_2 XANES line shape making hard to distinguish among the different features. Because of this, we will devote our attention to the L_3 edge features.

From the comparison of Figure 3.1.9 with Figure 3.1.3 it is clear that there is no correlation between the L_3 edge and O K edge shape despite they should probe the same empty DOS region because of the V *3d*-O *2p* hybridization. This can be understood considering the general features of the L_3 edge spectra: in the L_3 and L_2 XANES there is a transfer of spectral weight away from threshold (L_3 maximum intensity at 518.4 eV), apparent reduction of Spin-Orbit splitting (6.4 eV from XANES spectra, 7.3 eV from XPS) and a deviation from statistic intensity branching ratio: $I(L_3)/I(L_2)=2$. All of these features can be explained considering the strong interaction between the *2p* (core hole) and the *3d* electrons in the final state. In vanadium oxides *2p*-*3d* interaction is of the same order of magnitude of the S-O splitting, inducing a severe redistribution of spectral weight across the entire spectrum [143,149].

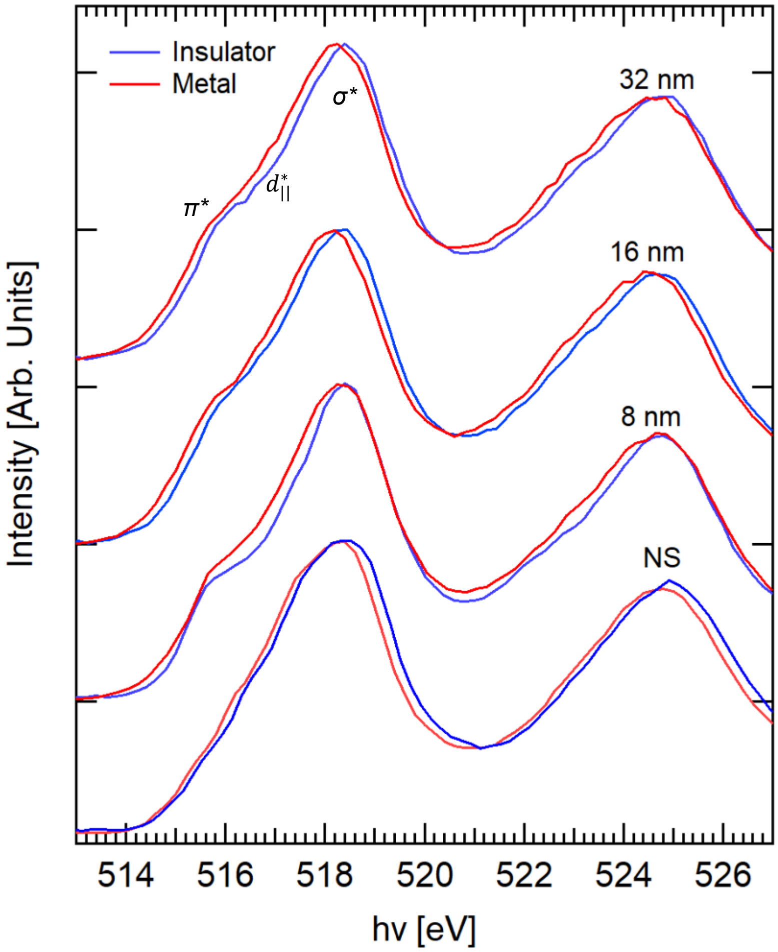

Figure 3.1.9: XANES spectra (Auger V $L_3M_{23}M_{45}$, 464 eV) in the hv range (513.5-526.5 eV) of the insulating (blue) and metallic (red) phase of different VO_2 samples. From top to bottom: strained samples of 32, 16, 8 nm and NS sample.

In Figure 3.1.9 are depicted the L_3 and L_2 edges of VO_2 samples of 32, 16, 8 nm thickness and of the NS film. Across the phase transition, a shift of 0.2 eV toward lower photon energy of the metallic phase spectra is observed. The major shape changes can be observed in the spectral region 514-516.5 eV where π^* and $d^*_{||}$ lie [61,62,150]. It is observable that in the insulating phase as the strain increase, the π^* feature becomes more evident because of the increasing π^*-$d^*_{||}$ splitting. The NS sample does not show prominent features in the L_3 pre-edge zone, in agreement with the results of chapter 2 and with what can be found in the literature for disordered samples [135].

The difference spectra calculated using Eq. 3.1.1 are reported in Figure 3.1.10.

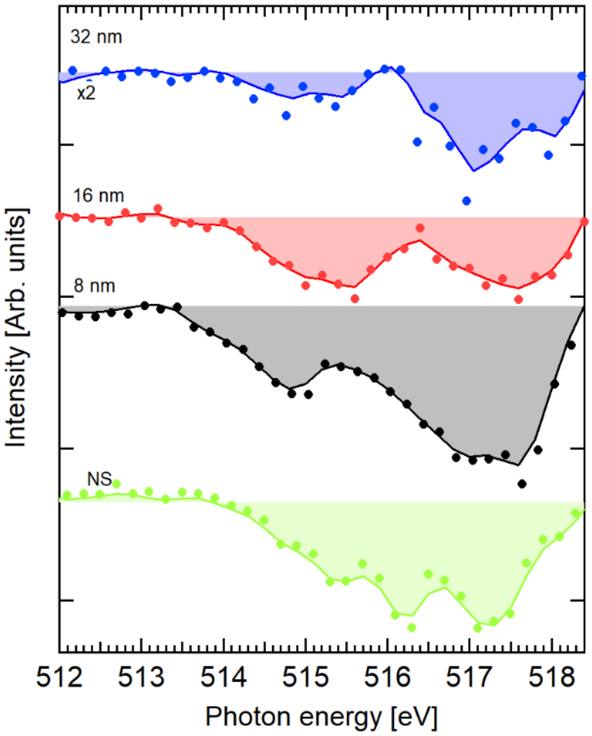

Figure 3.1.10: Difference of the Intensity of the XANES spectra showed in Fig. 3.8 in the range hv: 512-518.4 eV. The dots represent the experimental points while the continuous line is the smoothed curve of the experimental points (binomial algorithm) used as a guide for the eye. From top to bottom: samples of 32, 16 and 8 nm and NS film. The spectra are vertically shifted for sake of clarity. The difference spectrum of the 32 nm sample is multiplied by 2.

The interpretation of the difference spectra of the L edges is not straightforward to understand as in the case of O K edge. The V L edge difference spectra do not show positive contribution due to the lower photon energy shift of the metallic phase. Moreover, the tail of the intense contribution of the σ* band could influence the difference spectra. For strained samples, two main contributions can be identified at ~515 and 517.5 eV. The meaning of the position and the number of the different features within these contributions is still in progress for all samples (strained and NS).

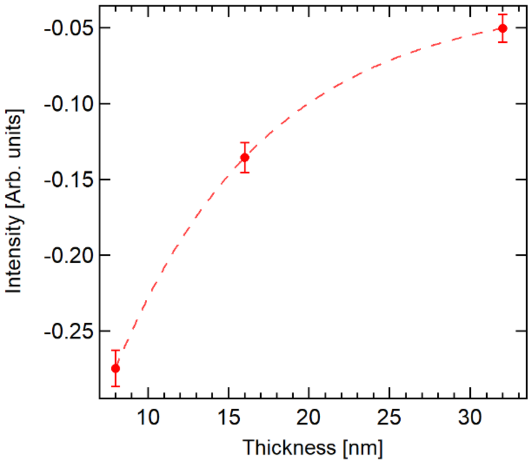

Figure 3.1.11: Integrated differences as a function of the film thickness. The Integration of the differences has been performed using a trapezoidal algorithm and in the photon energy range 512-518.4 eV. The dashed line is a guide for the eye.

However, integrating the difference spectra between 512-518.4 eV we observe a similar trend as those shown in Figure 3.1.6. This suggests that, even if the interpretation is not straightforward, the physics behind the difference at the V L edge and at the O K edge is the same.

3.2 Resonant photoemission

A powerful technique to extract detailed information about electronic-structure from a correlated *3d* electron system is resonant photoemission spectroscopy. A complete description of the theoretical principles of the ResPES can be found in Appendix 3, in this chapter will be reported a brief overview for the sake of clarity. ResPES working principles are the same as XPS or UPS but the photon energy is tuned in order to sweep across a core-level absorption threshold. In this way, important Auger-like decay channels are opened in which the core hole is filled by an electron from the final-state shell (in the case of study, *3d* shell) and another electron is ejected into the continuum. The Auger-like decay will interfere with the direct photoemission leading to a modulation of the finale state photoemission spectra features. ResPES

A ResPES map is usually acquired varying the photon energy and the electron kinetic energy range at the same time in order to maintain constant the binding energy range of interest.

To underline some of the general features of VO_2 ResPES map we will use the 16 nm thick sample (insulating phase, 30 °C) as an example. The ResPES map acquired sweeping the hv range across the L_3 and L_2 edges, is reported in Figure 3.2.1.

It is evident how the intensity of the VB spectra is modulated as a function of the photon energy because of the interference of the direct and photo-absorption channel. The maximum of the intensity is observed in concomitance of the maximum of the L_3 edge (518.4 eV). The arrows identify the Auger dispersion which in the ResPES map plotted against BE appear as inclined features since their kinetic energy is constant. The hv range is below the absorption threshold of the O K edge, we can identify the Auger as belonging to the V atoms. In particular, the two arrows identify the Auger decay:

A1=V $L_3M^d_{45}M^d_{45}$

A2= V $L_3M^p_{45}M^d_{45}$

Where M^d_{45} indicates the unpaired *3d* electrons whereas M^p_{45} the O *2p* - *3d* hybridized electrons.

Considering the kinetic energy of an Auger electron of the form XYZ as:

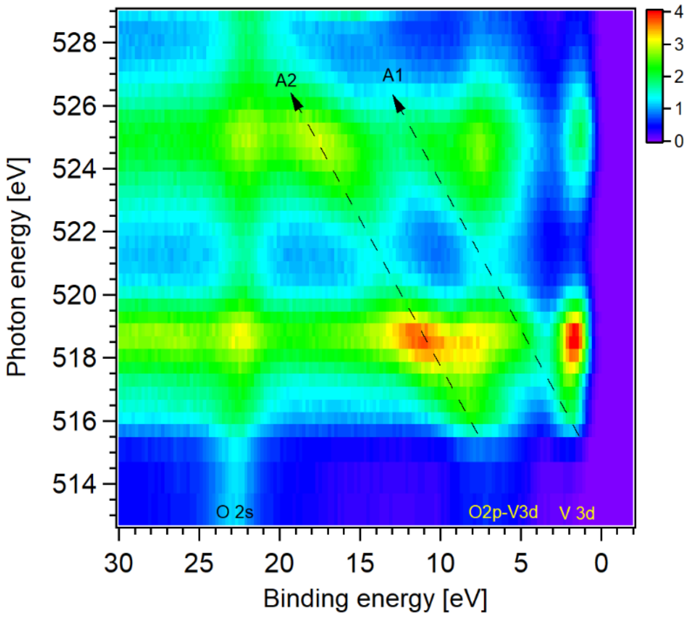

Figure 3.2.1: ResPES map of the VO_2 sample of 16 nm thickness in the BE range [-2, 30] eV (step of 0.2 eV) and in the hv range [513.2, 529] eV (0.4 eV step). Labels highlight the main contribution to the valence band: unpaired 3d electrons (1-2eV), hybridized 3d-2p band (5-8 eV) and O 2s electrons (22-23 eV). Arrows identify auger electrons dispersion.

$E_{Auger} = E_X - E_Y - E_Z$

Where E_X, stands for the Binding Energy of the core hole electron, E_Y is the BE of the electron that decay in the core-hole and E_Z represent the BE the Auger electron had inside the solid. For A1 and A2 is valid:

$$A2 - A1 = E_{3d\text{-}2p} - E_{3d} \sim 5\text{eV} \tag{3.2.3}$$

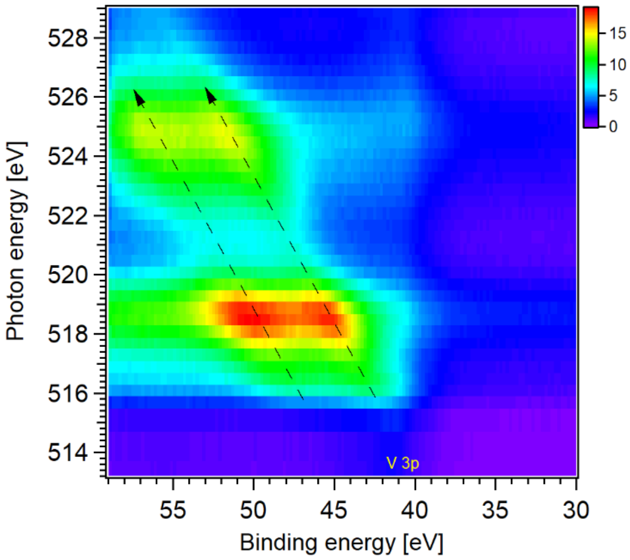

Figure 3.2.2: ResPES map of the VO_2 sample of 16 nm thickness in the BE range [30;59] eV (step of 0.2 eV) and in the hv range [513.2, 529] eV (0.4 eV step). Labels highlight the V3p electrons (40-41 eV) and arrows identify Auger $VL_3M_{23}M_{45}$ electrons dispersion.

Auger electrons of the form V L_2XY cannot be identified confirming the existence of a strong Coster-Kronig (CK) decay (V L_2L_3X) that quenches or drastically reduces the intensity of all the other decays with a hole in the V $2p_{1/2}$ core-level.

In Figure 3.2.2 is reported the ResPES map of the sample of 16 nm in the insulating phase in the region of V 3p electrons. The two arrows highlight the two lobes of the Auger V $L_3M_{23}M_{45}$: $L_3M_{23}M^{d}_{45}$ and $L_3M_{23}M^{p}_{45}$ (see Chapter 2).

By moving the photon energy through the O K edge the features of the ResPES map change dramatically since the oxygen Auger is so intense to cover all the other features (see arrows labelled A, B, C in Figure 3.2.3).

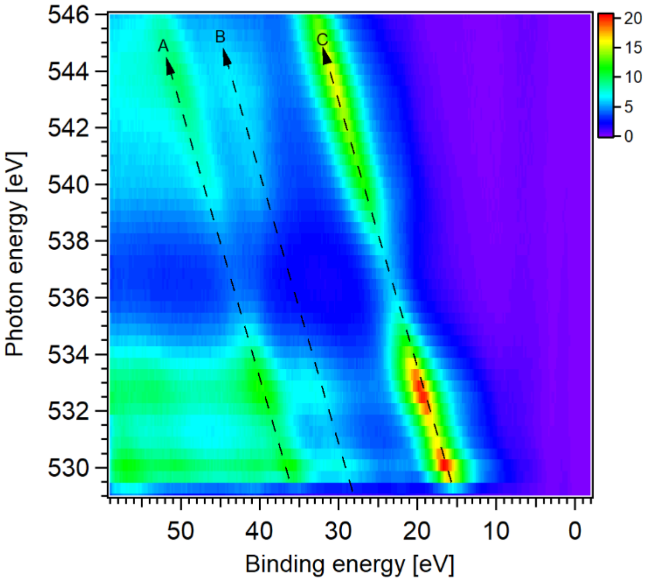

Figure 3.2.3: ResPES map of the VO_2 sample of 16 nm thickness in the BE range [-2;59] eV (step of 0.2 eV) and in the hν range [529, 546] eV (0.4 eV step). Labels and arrows identify Auger electrons dispersion.

The decay labelled A and C are compatible with the O KL_1L_{23} (KE=493.4 eV) and O $KL_{23}L_{23}$ (KE=507 eV) respectively[104]. The B feature is not compatible with any of the allowed O KXY decay channels (KL_1L_1, KL_1L_{23} and $KL_{23}L_{23}$) and it is not observed in pure V sample [104,151], therefore it must originate from oxygen. The energy distance between A and B is 7.2 eV, which is not compatible with a dynamic of the type described from Eq. 3.2.3 pointing out a final state effect as the cause of the B feature. A possible explanation is proposed:

For the decay KL_1L_{23}, the spin-singlet forming the O $2s^2$ is broken to fill the O 1s core hole of the Auger emission process. The metastable state ($2s^1$ $2p^6$) state can, therefore, have two possible spin orientations up or down, that will couple, aligning or anti-aligning, with the total spin of the unpaired *3d* electron in the valence band. The proposed mechanism is similar to the final state splitting observed for other decays channel involving an intermediate ns hole (e.g. $L_3M_1M_{23}$) [151] and for direct photoemission of 3s electron in vanadium oxides [107]. Moreover, for V_2O_5 in which there are no unpaired *3d* electrons in the valence band, the B feature is not observed [104] confirming our interpretation. In addition, no visible resonant enhancement in the BE region of the V *3d* electron is observable, pointing out that the amount of V *3d* - O*2p* hybridization for the unpaired *3d* electron is small respect to the *3d* character.

In Figure 3.2.4-6 a series of individual photoemission spectra are acquired tuning the photon energy across the V L edges for the sample of 32, 16 and 8 nm thickness.

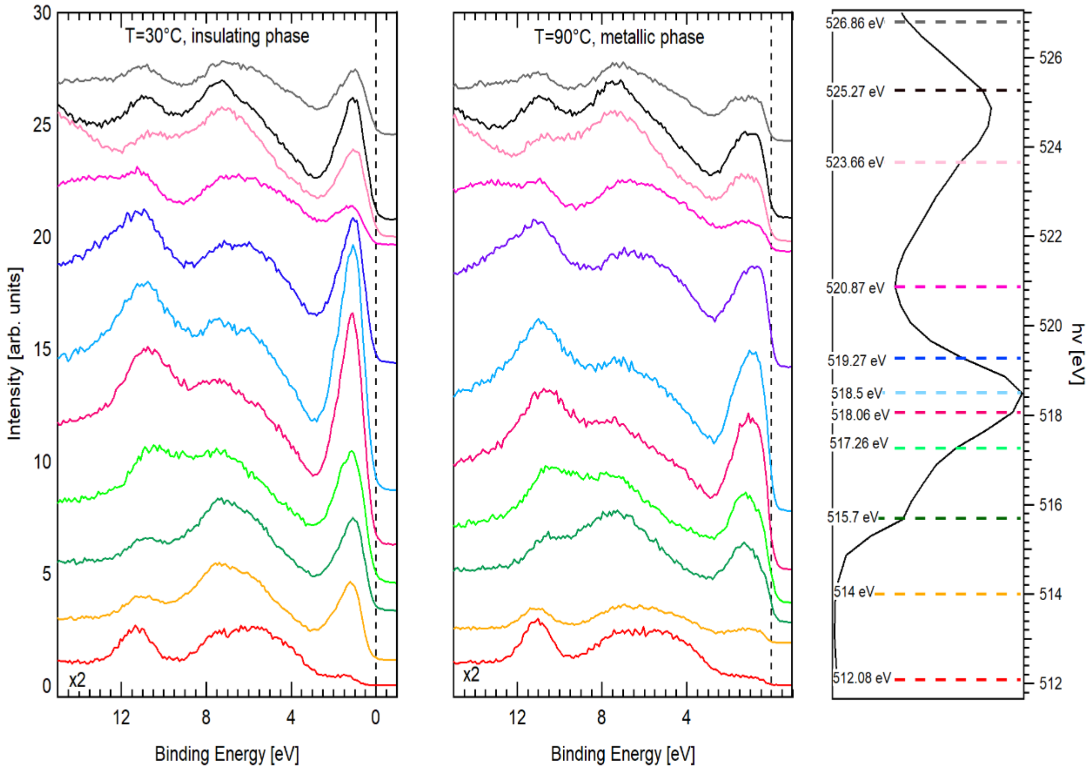

Figure 3.2.4: Comparison of ResPES spectra for the 32 nm VO_2 film in the binding energy range (15,-1 eV). Spectra have been collected at different photon energies both in the insulating (T=30 °C, left) and in the metallic phase (T=90 °C, centre). In the right panel is shown the XANES spectrum of the insulating phase (Auger yield at 464 eV). The spectra collected at 512 eV have been magnified (x2). The spectra are normalized to the incident photon flux.

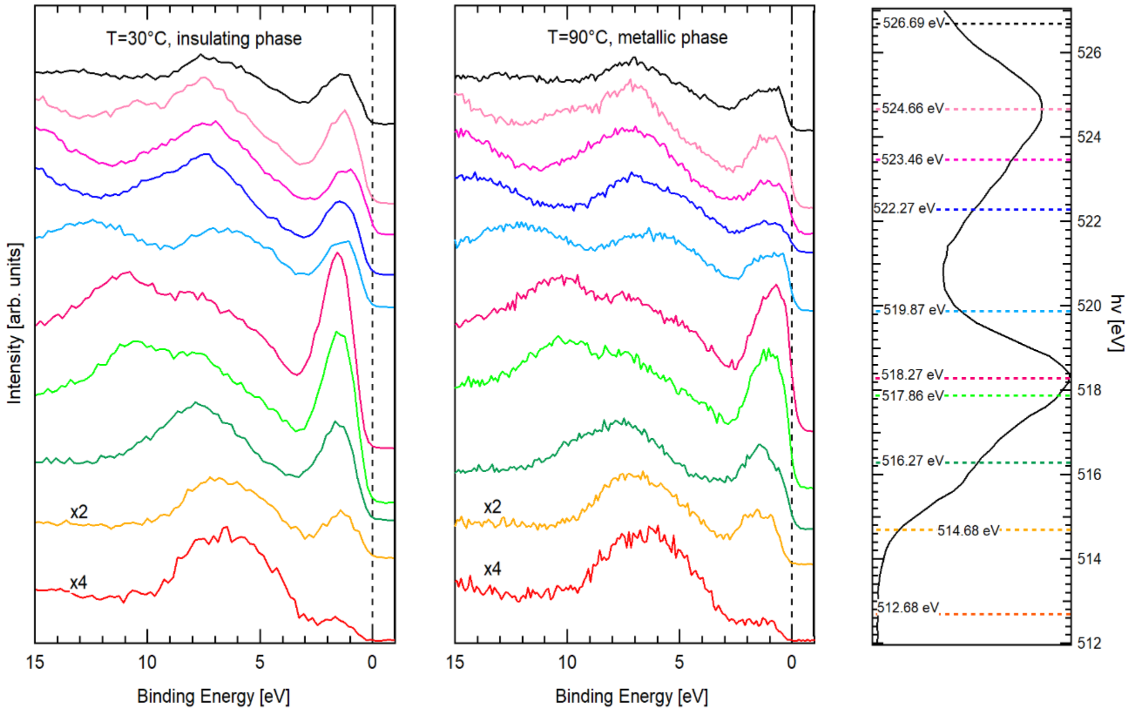

Figure 3.2.5: Comparison of ResPES spectra for the 16 nm VO_2 film in the binding energy range (15,-1 eV). Spectra have been collected at different photon energies both in the insulating (T=30 °C, left) and in the metallic phase (T=90 °C, centre). In the right panel is shown the XANES spectrum of the insulating phase (Auger yield at 464 eV), horizontal dashed lines highlight the photon energies used to acquire the spectra. The spectra collected at 512.68 eV and 514.68 eV have been magnified (x4 and x2 respectively). The spectra are normalized to the incident photon flux.

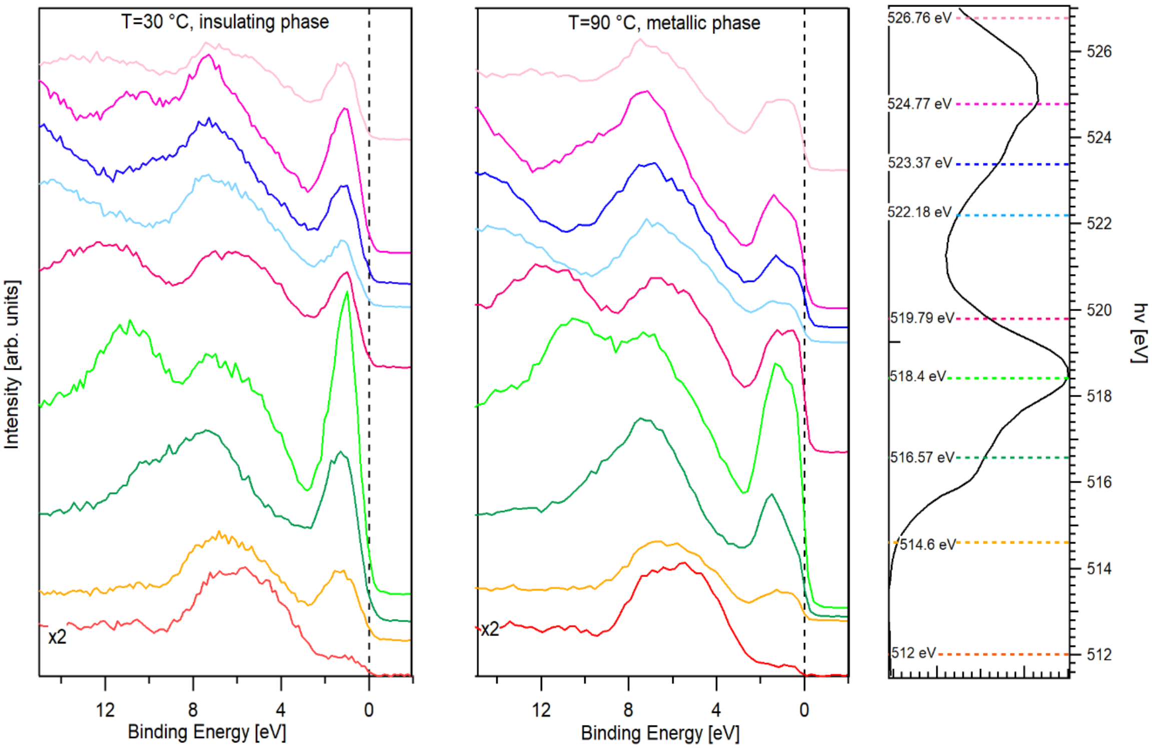

Figure 3.2.6: Comparison of ResPES spectra for the 8 nm VO_2 film in the binding energy range (15,-2 eV). Spectra have been collected at different photon energies both in the insulating (T=30 °C, left) and in the metallic phase (T=90 °C, centre). In the right panel is shown the XANES spectrum of the insulating phase (Auger yield at 464 eV), horizontal dashed lines highlight the photon energies used to acquire the spectra. The spectra collected at 512 eV have been magnified by a factor 2 for clarity. The spectra are normalized to the incident photon flux.

The standard features of vanadium oxide VB spectra are observed (as discussed in section 2.2.5), in addition, a peak in the 32 nm sample spectra is observable around 11 eV which can be linked to oxygen vacancies[119]. For the entire set of samples, the metallic state is characterized by the appearance of a Fermi edge. The off-resonance spectra are quite similar to a standard VB spectrum of VO_2 [119,120,152] while, as the photon energy span through a resonance, the emission from the resonating state is modulated similarly to what reported by Eguchi et al. for VO_2 thin film [153]. The comparison of these photoemission spectra collected at different excitation energies clearly shows the enhancement of the V *3d* unpaired electrons feature in the insulating (30° C) and the metallic state (90° C). In fact, the V *3d* states strongly resonate at ~1.5 eV due to the interference between the direct and the photo-absorption channel. In particular, as discussed before and confirming a previous ResPES investigation [151], the unpaired V *3d* electrons resonate with the V $L_3M^d{}_{45}M^d{}_{45}$ decay. The maximum of the *3d* signal enhancement is observed in the range 518.4±0.1 eV, in agreement with the maximum of the XANES spectra (see Figure 3.1.9), confirming the strong *3d* nature of the 1-2 eV peak.

In the metallic phase, the *3d* electrons peak exhibits two features centered at about ~1.5 and ~0.5 eV (see Figure 3.2.7). The appearance of two contributions near the Fermi level is the fingerprint of the strong electron-electron interaction (U) in Mott-Hubbard metals [154]. For historical reasons, the low BE feature has been called coherent peak since it is obtained by band structure calculations in the framework of the independent particle approximation neglecting the many-body effects, while the high BE feature is the incoherent peak [154]. The existence of a coherent and incoherent contribution to the excitation spectra has been widely considered for different strongly correlated materials as the marker of the MIT [108,114,153,155–157].

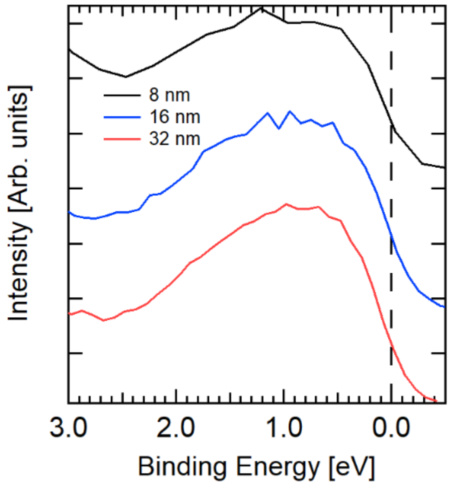

Figure 3.2.7: VB spectra of the unpaired 3d electrons band in the BE range (-0.5; 3) eV for the sample of 8, 16 and 32 nm thickness (metallic phase). The peaks' shape suggests the existence of two contributions centred at ~1.5 and ~0.5 eV.

The coherent peak is also called the quasiparticle peak and it is generated by the itinerant *3d* band states. The quasiparticle and the incoherent peak can be assigned to two different final states in which two screening mechanisms operate. After the photoemission of a *3d* electron, the initial $3d^1$ configuration is formally left in the $3d^0$ state. According to Mossanek and Abbate, the $3d^0$ finale state is poorly screened by the surrounding atoms while the features near the Fermi Level are well-screened configurations [158].

In the VO_2 metallic phase, the most favorable final configurations are $3d^1\underline{C}$ (coherent hole) and $3d^1\underline{L}$ (ligand hole) [158]. The $\underline{C}$ state accounts for a non-local screening channel of the photo-hole provided by the surrounding vanadium atoms. In the $\underline{L}$ configuration, the nearest oxygen atom provides the screening electron (Figure 3.2.8).

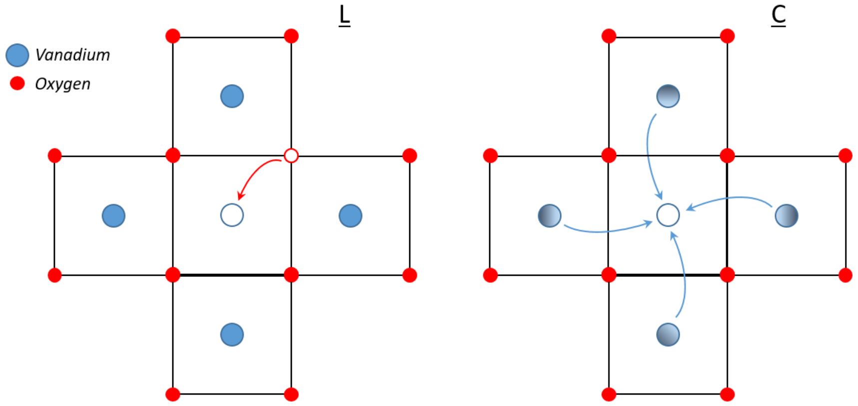

Figure 3.2.8: Schematic representation of the $\underline{L}$ and screening channels. Left panel, the photo-hole is screened by transfer of an oxygen electron (L); right panel, the photo-hole is cooperatively screened by itinerant valence electrons (c).

In the Insulating state, the *3d* orbitals are directed along the V-V dimer direction. The intra-dimer screening is not possible, while the inter-dimer and $\underline{L}$ mechanisms are available. According to theoretical calculation, the insulating phase peak around 1 eV of binding energy can be assigned to the $3d^1\underline{L}$ configuration, matching the Lower Hubbard Band (LHB) [153,158].

The presence of different screening properties in the insulating and metallic phases can be probed experimentally using ResPES. In fact, ResPES can be used as a probe of the metallicity of a sample [159–161]. The intensity (normalized for the photon flux) of the resonant photoemission spectra can be linked to the screening parameter by Eq. 3.2.4 [159–161].

$$\frac{I}{I_0} \alpha \frac{1}{L_S} \tag{3.2.4}$$

Where I is the ResPES peak intensity, I_0 the incident photon flux and L_s the material screening parameter (inverse of the Thomas-Fermi screening length[161]). This can be qualitatively understood as follow: in an insulating material, L_s is small, the core-hole generated by the ResPES process is poorly screened allowing the excited state described in Eq. 3.2.2 to properly decay in order to interfere with the direct photoemission. On the other hand, the delocalized electron inside a metal (higher L_s) will quickly screen the photo-hole partially quenching the valence-to-core decay of the excited state (Eq. 3.2.2), which is at the basis of the resonant enhancement.

Table 3.1: $L_{metal}/L_{insulator}$ for the different samples

Sample	$L_{metal}/L_{insulator}$
8 nm	1.44±0.01
16 nm	1.73±0.01
32 nm	1.93±0.01
NS film	1.06±0.01

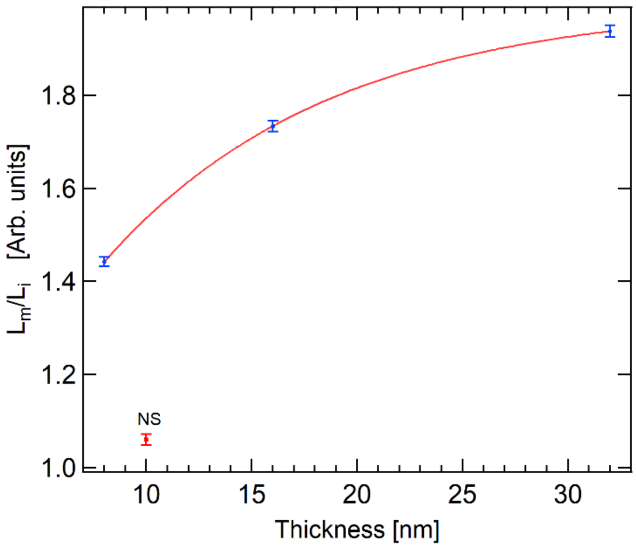

Figure 3.2.9: Ratio between the screening length of the metallic and insulating phase as a function of sample thickness. The X position of the NS point has been arbitrarily chosen.

The ResPES data confirm this model as can be seen from Figure 3.2.4-6. In fact, tuning the photon energy hv at the maximum of the L_3 threshold, the insulating *3d* peak is always more intense respect to the metallic counterpart. Applying Eq. 3.2.4 to our data and making the ratio between the insulating and metal ResPES intensities, $L_{metal}/L_{insulator}$ can be calculated and plotted as a function of sample thickness (Figure 3.2.9).

The theoretical value of L_m/L_i can be estimated considering that the screening parameter is the inverse of the Debye screening length:

$$L_s = \frac{1}{\lambda_D} = \sqrt{\frac{e^2 n}{\varepsilon k_b T}} \tag{3.2.5}$$

Where λ_D is the Debye screening length, *e* is the carrier charge, *n* is the carrier density, $\varepsilon = \varepsilon_0\varepsilon_r$ is the average dielectric constant, k_b the Boltzmann constant and T the temperature. L_m/L_i is, therefore:

$$\frac{L_m}{L_i} = \sqrt{\frac{n_m \varepsilon_i T_i}{n_i \varepsilon_m T_m}} \tag{3.2.6}$$

For the ResPES measurements T_i=30°C=303.15 K and T_m=90°C=363.15 K. Using the values of dielectric constant reported by Zheng and coworker [162] ($\varepsilon_i=\varepsilon_r$(300 K)=40 and $\varepsilon_m=\varepsilon_r$(360K)=$10^4$) and as carrier concentration $n_i=1.9*10^{19}cm^{-3}$ $n_m=1.9*10^{23}cm^{-3}$[163] a value of $L_m/L_i \approx 5.7$ is obtained for bulk VO_2. This value is in fairly good agreement with the L_m/L_i reported in Table 3.1. despite the Debye model cannot properly evaluate L_m. In fact, it is necessary to consider that at high-temperature VO_2 is a “poor” metal in which electron correlation effects are of primary importance over transport properties. In fact, metallic vanadium dioxide violates the Ioffe-Regel-Mott criterion i.e. in a metal electron mean free path cannot be less than the lattice spacing [164], implying that Boltzmann statistic cannot be used to describe VO_2 properties and therefore making equation 3.2.5 an approximation of the metallic screening parameter.

It is also observable that $L_{metal}/L_{insulator}$ decrease as a function of sample thickness with a trend which is very similar to what observed from the XANES spectra analysis of the previous sections suggesting a correlation between screening parameter and orbital occupancy.

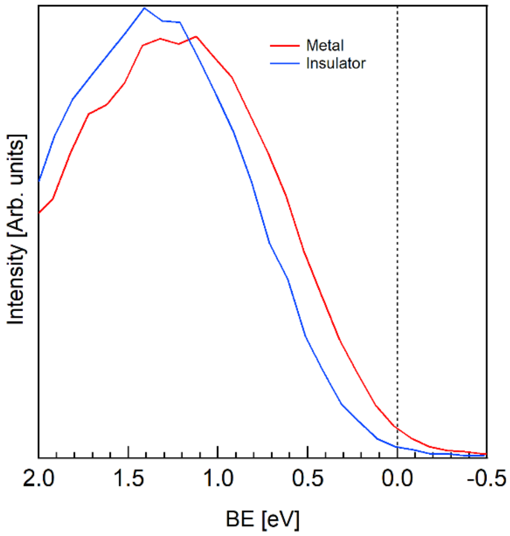

Figure 3.2.10: VB spectra of the NS sample acquired at 30 °C (blue curve) and 90°C (red curve) in the BE range -0.5-2 eV acquired with hv=518.4 eV.

For the NS sample the value of $L_{metal}/L_{insulator}$ >1 points out an increase of metallicity from 30 to 90 °C, this is also confirmed by the appearance of a small but finite DOS at FL in the high-temperature spectra of the VB (Figure 3.2.10). These results combined with the previous XANES analysis, identify a collapse of the bands in the π* energy region i.e. a collapse of an empty band with t_{2g} character, to the FL as the cause of the insulating gap closure. A proposed band model for the Mott-Hubbard transition in disordered VO_2 is proposed in Figure 3.2.11.

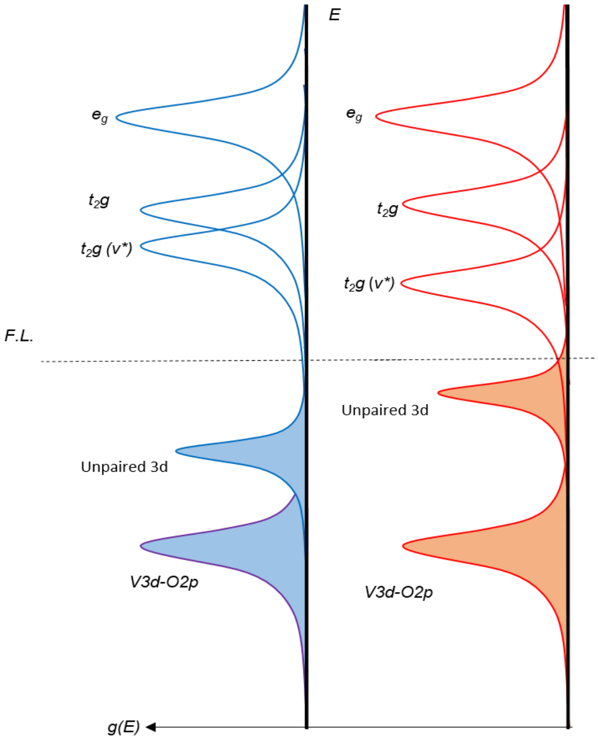

Figure 3.2.11: Schematic representation of the insulating bandgap closure dynamics in the NS sample. Left panel: insulating phase DOS and empty DOS; right panel: metallic phase DOS and empty DOS.

Coulomb repulsion makes one of the t_{2g} empty orbitals not degenerate with the others (labeled as t_{2g}(v*) in Figure 3.2.11). Heating the sample the localized electrons have enough kinetic energy to overcome the Coulomb repulsion with the subsequent collapse of the t_{2g}(v*) band and population of FL, generating a conductive state.

Since the Peierls distortion in the NS sample is quenched and an Anderson localization process can be excluded (the NS samples are disordered before and after the MIT), the transition has to be driven by mutual electron interactions, revealing a Mott-Hubbard mechanism as driving force of the MIT. However, the FL is poorly populated with respect to the crystalline samples. This suggests that a cooperative mechanism between Peierls and Mott-Hubbard mechanism is necessary to increase the FL occupation in the metallic phase, and in general to tune the properties of the MIT.

Chapter 4.

***Orbital contribution to the MIT studied by CIS spectroscopy*.**

In the previous chapter XANES spectroscopy and resonant photoemission have been exploited to understand the orbital dynamic across the MIT in VO_2 with different structural properties.

ResPES takes advantage of the possibility to change the photon energy to look for a resonating behaviour of a core-level. The emission from the resonating final state is modulated because of the interference between the direct photoemission channel and the photoabsorption Auger-like channel. Two acquisition methods have been introduced in order to study the resonance effect: Constant Final State (CFS) and Constant Initial State (CIS). [130] A spectrum is acquired in CFS when the incident photon energy hν is varied while the detected electron kinetic energy is fixed[141,165,166]. Actually, the Auger yield is a particular kind of CFS acquisition. CFS measurements essentially return the photo-absorption spectrum of the sample across the resonance. As shown in chapter 3, the strength of CFS spectroscopy relies on the possibility to choose the fittest Auger channel (or in general the fittest final state) to investigate the system. Selecting the Auger V $L_3M_{23}M_{45}$ or the O $KL_{23}L_{23}$ it is possible to optimize the collection of the vanadium L edges or of the oxygen K edge in the absorption spectra vanadium oxides.

A CIS acquisition is characterized by the simultaneous variation of the photon energy and electron kinetic energy (K_e) in order to maintain constant the ionization energy $IE = h\nu - K_e$ [141,165,166]. ResPES spectra are collected using the CIS mode in order to probe the same Binding Energy region for every photon energy, therefore this acquisition method measures the ResPES cross-section lineshape. CIS spectroscopy allows studying the resonant enhancement of the cross-section of valence band electron when the photon energy moves through a core resonance. In synthesis, CIS and CFS are two detection methods, which allow acquiring an absorption spectrum exploiting different (partial) electron yield channels. At variance as in the previous chapter focused on CFS absorption spectra (Auger yield XANES), here I'll focus on CIS absorption spectra of *3d* and 3p electrons. Spanning the photon energy through the *2p* core resonance, different possible decays of the excited state have been measured [167].

In this case the absorption process results in the excitation

$$2p^6 3d^n + h\nu \rightarrow 2p^5 3d^{n+1} \tag{4.1}$$

which can decay via Coulomb interaction in two configurations with the emission of one electron from different orbitals:

$$2p^5 3d^{n+1} \rightarrow 2p^6 3d^{n-1} + e_d^- \tag{4.2}$$

$$2p^5 3d^{n+1} \rightarrow 2p^6 3p^5 3d^n + e_p^- \tag{4.3}$$

The processes described by 4.2 and 4.3 emit a *3d* and a 3p electron, respectively and in the ResPES experiment they will constructively interfere with the *3d* and 3p direct photoemission channel. The samples studied were three ordered thin and ultra-thin VO_2 films (8, 16 and 32 nm thick, respectively) and one nanostructured disordered sample.

The V *3d* CIS and V *3p* CIS spectra of the strained films have been investigated across the phase transition and are discussed in section 4.1 and 4.2, respectively. In section 4.3 the V *3d* and V 3p CIS spectra of the nanostructured disordered sample are presented. The CIS spectra have been collected using the same experimental parameters used for the ResPES experiments described in chapter 3.

4.1 V *3d* CIS spectroscopy of VO_2 thin films.

The major spectral changes across the MIT in VO_2 occur around the Fermi level involving mainly V *3d* electrons. Formally, the VO_2 is a $3d^1$ electron system whose unpaired electrons form intermetallic bonds localized in the binding energy region between 2.5 eV and the FL. To understand CIS data, a deeper understanding of the related photoemission spectra is necessary. The VB photoemission spectral features of the VO_2 can be described in terms of final state configurations. In the insulating phase, the V *3d* peak is centred at ~1.5 eV. Its nature can be explained assuming that the oxygen atoms contribute to locally screen the V *3d* photo-hole. Therefore, the final state is depicted as the $3d^1\underline{L}$ (ligand hole)[158]. In the metallic state, we assist to the population of the FL. Since the electrons are free to move within the solid an additional screening mechanism and therefore an additional final state is available in this phase and observable in the VB: the $3d^1\underline{C}$ (coherent hole). This is generated by a non-local screening channel of the photo-hole provided by the surrounding vanadium atoms and it is centered at ~0.4 eV [158].

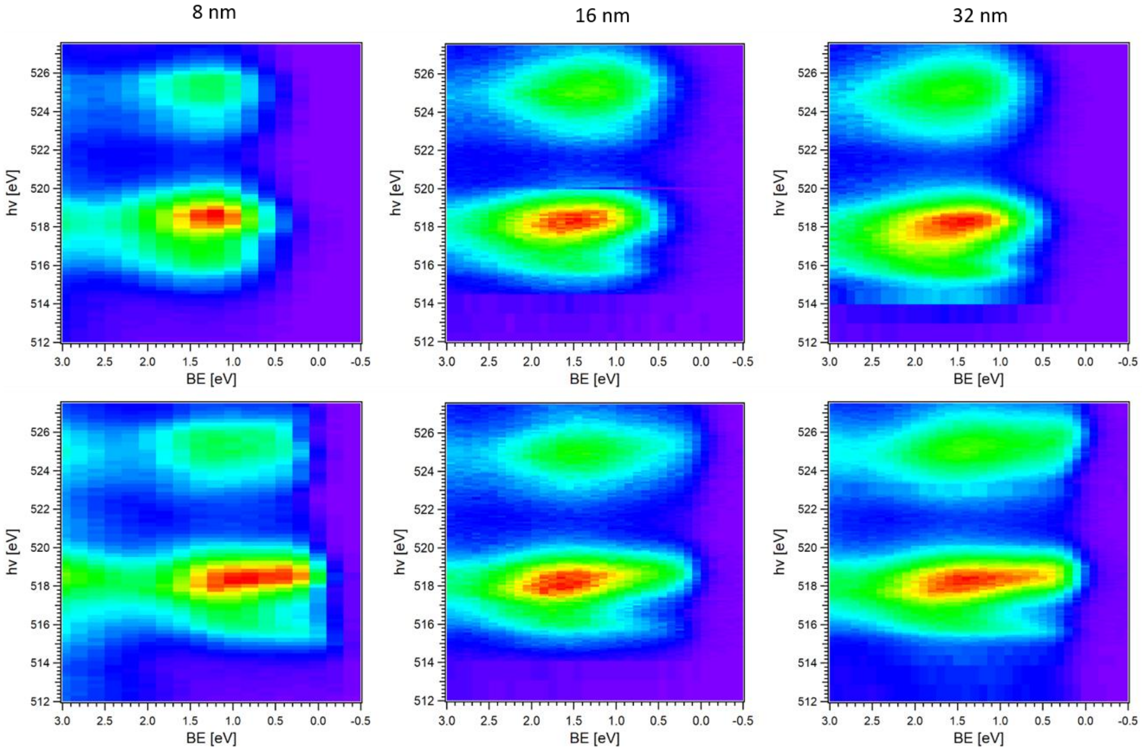

Figure 4.1.1: ResPES maps of the V 3d electrons (BE region -0.5; 3 eV) across the L_3 and L_2 resonances hv [512-527.5] eV collected with step 0.1 eV. The maps of each sample (8, 16 and 32 nm) are vertically aligned: top panels, insulating phase; bottom panels, metallic phase. The 8 nm sample maps have been collected with a BE step of 0.25 eV while the 16 and 32 nm maps with a BE step of 0.1 eV.

Since $\underline{C}$ and $\underline{L}$ VB features are generated by two different screening mechanisms, they will couple differently with the resonant excited state and exhibit a different CIS line shape.

The acquisition of a CIS spectrum corresponds to one vertical energy scan of the ResPES map, i.e., to probe the intensity variation of one fixed BE feature as a function of the photon energy. The ResPES maps of the V *3d* electrons obtained tuning the photon energy across the V L edges for the samples of 8, 16, 32 nm thickness are compared in Figure 4.1.1. For the metallic phases (bottom panels) it is easily recognized the appearance of the FL at BE=0 eV. The maximum of the resonance is located between the photon energies of 518 and 519 eV. At hv ~516 eV a weaker resonant enhancement is also observed. The photon energy dependence of the V *3d* electrons is more pronounced across the L_3 edge with respect to the L_2 because of the presence of the Coster–Kronig decay (V $L_2L_3M_{4,5}$)[104]. Therefore the study of the spectral changes is limited to the L_3 edge.

Using the CIS spectroscopy it has been possible to probe that the unpaired V *3d* electrons are poorly hybridized with oxygen. This can be obtained by looking at the line shape of the V *3d* CIS spectrum, in the photon energy range of the O K edge. As an example, in figure 4.1.2 is showed the CIS spectra of the V *3d* electrons of the 16 nm sample in the photon energy across the V L edges and the O K edge. Despite elsewhere specified, XANES spectra acquired with the Auger yield (V $L_3M_{23}M_{45}$) will be referred to as XANES for sake of brevity.

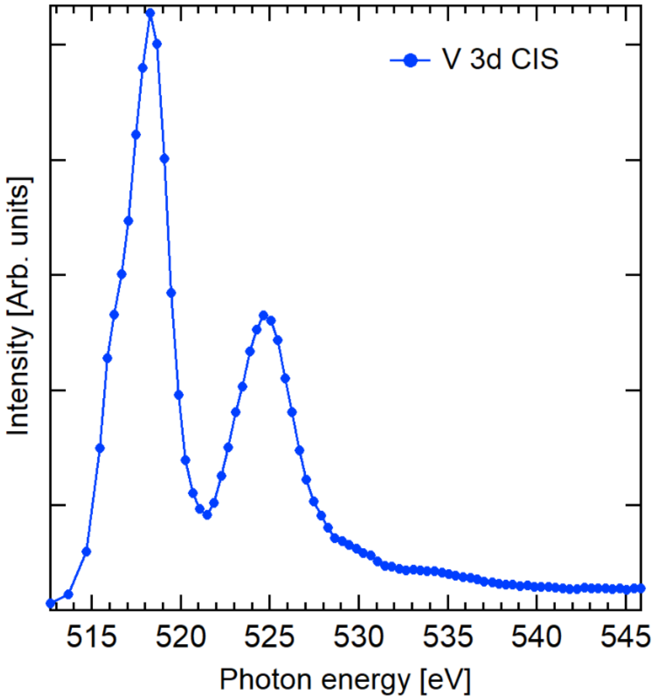

Figure 4.1.2: CIS spectrum of V 3d electrons for the sample of 16 nm in the insulating phase (30° C) in the photon energy range [512.68; 545.85] eV collected with a step of 0.4 eV. The intensity of each point of the spectrum has been obtained averaging the intensity in the BE range [0;3] eV.

The shape of V *3d* CIS spectrum resembles that of VO_2 XANES. V L_3 and L_2 resonances are clearly observable at ~518 and 525 eV, respectively, while only small oscillations are visible in correspondence of the O K edge (at ~530 eV) pointing out the negligible V *3d*-O *2p* hybridization.

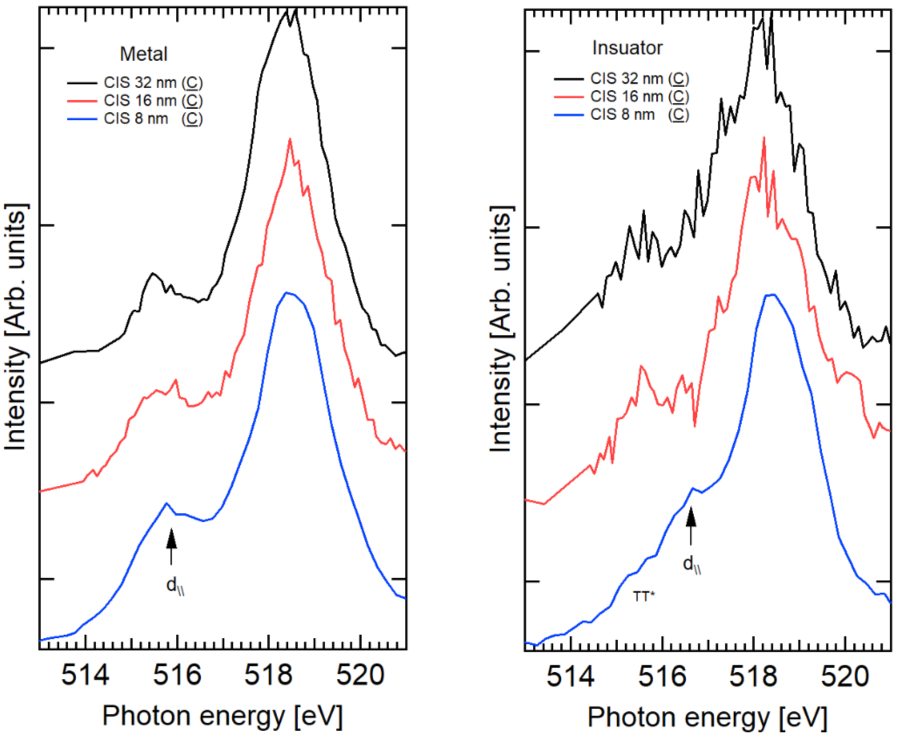

Figure 4.1.3: CIS spectra of the C valence band feature (0.4 eV) in the metallic (left panel) and in the insulating phase (right) for the 32, 16 and 8 nm films in the energy range: 513-521 eV for 0.1 eV (32 and 16 nm) and 0.2 eV (8 nm) step.

The CIS spectra of the C valence band feature are depicted in Figure 4.1.3. All CIS spectra in this chapter have been normalized to the incident photon flux and to the maximum of the L_3 resonance intensity. The signal of the 32 and 16 nm samples is noisier respect to the 8 nm due to the appearance of undesired electrical noise which cause have not been understood. Respect to XANES spectra, CIS spectra of the C feature are those which exhibit the largest changes in the line shape. In the metallic phase, two main features are observable, the σ^* resonance around 518.4 eV and the small pre-edge peak centred at ~516 eV. To understand the nature of the pre-edge peak, it is necessary to monitor its evolution as a function of the sample thickness (i.e., the strain). Increasing the strain (i.e., decreasing the sample thickness) the pre-edge peak increases in intensity relative to the σ^* resonance, and concurrently the valley amongst them decreases its deepness. In addition, the broadening of the pre-edge peak width occurs. In the metallic phase of the VO_2, π^* and $d_{||}^*$ are partially degenerate at the FL and hence are both populated, although their occupation is different. In bulk VO_2 because of the strong V-O hybridization, the FL is mostly occupied by the $d_{||}^*$ band with a component of π^* (see figure 3.1.4). As explained in the previous sections, strain influences the relative vanadium and oxygen positions, as a consequence the overlap between metal and ligand wave functions and in addition the energetic position of the orbitals. With the strain the apical V-O distance increases, decreasing the overlap among V *3d* and O *2p* orbitals. This leads to a destabilization of π^*, which is lowered in energy respect to $d_{||}^*$ changing the orbital occupation at the FL. In strained samples the $d_{||}^*$ band is emptier respect to the π^* band opposite to bulk samples. As a consequence, in the metallic phase, it is possible to assign the pre-edge peak of the C CIS spectra to the $d_{||}^*$ band (516 eV). In fact, its intensity and width increase with the strain pointing out an increase of the empty states compatible with the strain-induced orbital dynamics described above. In addition, spectral features linked to the π^* band are lacking within our experimental resolution.

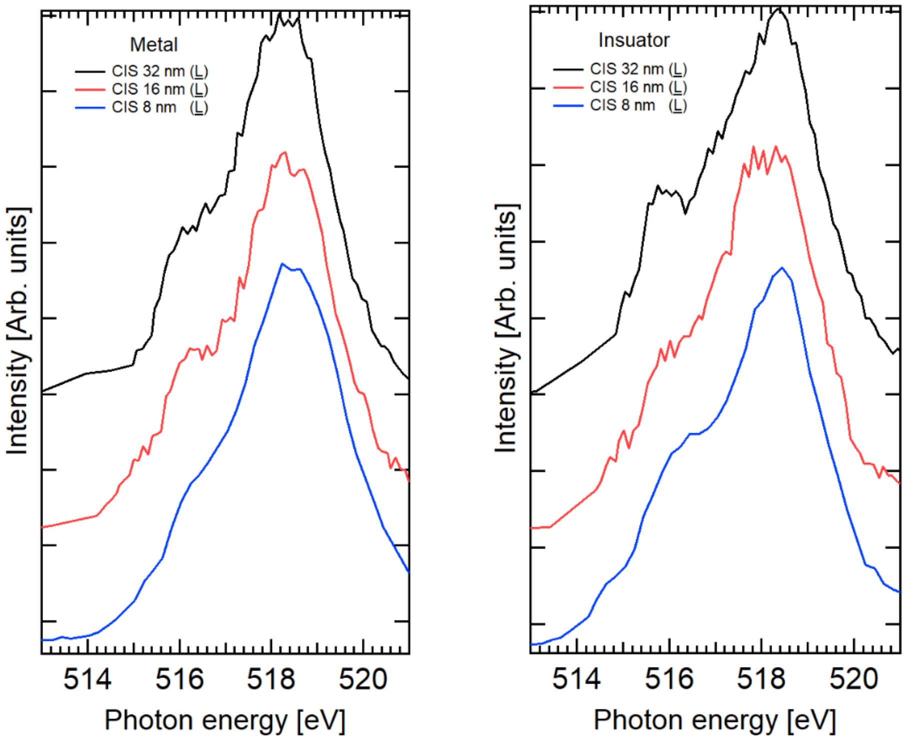

Figure 4.1.4: Comparison of CIS spectra of the L valence band feature (1.5 eV) in the metallic (left panel) and in the insulating phase (right) for the 32, 16 and 8 nm films in the photon energy range 513-521 eV for 0.1 eV (32 and 16 nm) and 0.2 eV (8 nm) step.

In the insulating phase, the C screening channel should be absent. However, a fraction of thermally excited electrons is available at ~0.4 eV and a small CIS signal can be detected (see figure 4.1.3, right panel). The 32 and 16 nm samples spectra are quite noisy. While for the 8 nm sample the signal is good enough to observe two pre-edge features centred around 515-515.5 and 516.1-516.3 eV. In the insulating phase $d_{||}^{*}$ and π* are both empty, with π* positioned closer to the FL (see Figure 3.1.4). The pre-edge feature located at 515-515.5 eV is assigned to π* while the second one to $d_{||}^{*}$ in good agreement with XANES results [61]. The σ* feature is centred at 518.4 eV.

The CIS spectra of the L valence band feature (BE=1.5 eV) are reported in Figure 4.1.4. The overall line shape is broader respect to the C CIS spectra and the individual orbital contributions are not distinguishable. In the metallic phase, a feature centred at ~516 eV can be observed. Increasing the strain, its intensity tends to decrease. This trend is compatible with the increased population (depletion of the empty states) of the π* band as a function of strain, which suggests the increased π* sensitivity respect to the CIS spectra of the C feature.

In the insulating phase, the feature around 515.5 eV can be assigned to the π* band. The $d_{||}^{*}$ band is not detectable probably because of the broadening of the σ* features, which might cover the weak signal.

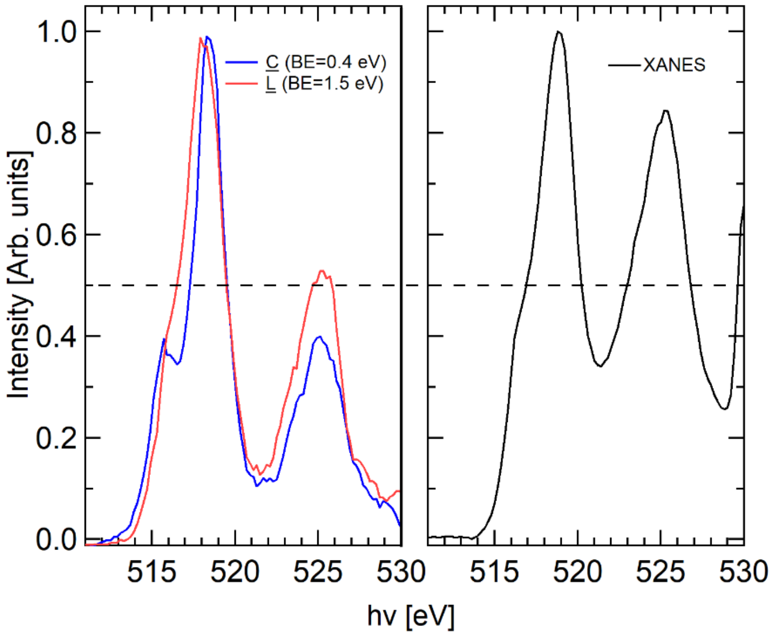

Figure 4.1.5: Left panel: CIS spectra of the L (red line) and C C (blue line) valence band features of the metallic phase of the 8 nm film in the photon energy range 511-530 eV. Right panel: XANES spectra of the 8 nm sample (metallic phase).

The selective sensitivity to different empty bands for the C and L partial electron yield can be explained considering their nature. The C final state is generated by the cooperative screening of the *3d* photo hole by the nearest vanadium atoms. In metallic vanadium dioxide, the $d^*_{||}$ band is directed along the rutile c axis i.e., along the V-V bonds. The intermetallic bonds are the same involved in the non-local screening mechanism of the C final state, therefore, it is very likely that the core-hole excited state $2p^5 3d^2$ wave function (where the extra *3d* electron is in the $d^*_{||}$ band) have greater overlap with the $3d^1$C final state wave function. The same consideration can be applied to understand the higher sensitivity of the L CIS spectra to the π^* empty band. In the L final state, the *3d* photo hole is locally screened by the oxygen atoms of the coordination octahedron. Since the π* band is formed by the V *3d* electrons, which form bonds with π character with oxygen atoms, an excited electron placed in the π* band is more likely to be spatially close to oxygen atoms. The Auger transition of the excited state with an extra electron in the π* band into the L final state may be therefore favoured. However, further theoretical and experimental investigations are necessary to support this interpretation.

An interesting difference between CIS and XANES spectra is the L_3/L_2 branching ratio. Statistically $L_3/L_2=2$, but because of the poor screening of the photo-excited core-hole, many systems show deviation from the ideal value[143,149]. In figure 4.1.5 are compared the CIS spectra of the C and L valence band feature and the XANES spectra of the 8 nm film in the metallic phase. It is evident how the L_3/L_2 ratio of CIS spectra is much closer to the statistical value due to the nature of CIS spectroscopy. Indeed, the intensity of the CIS spectra is the outcome of the constructive interference of direct photoemission and the photoabsorption channel. The direct photoemission of V *3d* electrons does not suffer the core-hole influence, as a consequence, only those *3d* electrons, which are generated by the Auger-like decay in which the *2p* core hole is well screened will interfere constructively with the direct photoemission. CIS spectroscopy of V *3d* electrons is a natural way to minimize the core hole contribution making simpler the line shape interpretation.

The C and L CIS channels exhibit a different L_3/L_2 branching ratio and in particular, the C spectrum intensity at the L_2 resonance appears suppressed. Probably because the excited state, which resonates with the C feature has longer lifetime respect to that resonating with the L channel. At the resonance with the V L_2 edge, the Coster-Kronig decay channel is opened. If the lifetime of the core-hole excited state is short enough, the CK decay does not heavily affect the *3d* electron yield (as for the L CIS spectra). On the other hand, a long-lived excited state increases the probability to relax trough the CK mechanism as for the C spectra at the L_2 resonance. Since the intensity of the CIS spectra (C) in resonance with the L_2 is about 0.4 instead of 0.5, it is possible to estimate that ~20 % of C electrons are lost because of the CK decay. The hypothesis of the different excitation lifetime is confirmed by the broadness of the CIS spectra. The C spectrum exhibit quite sharp features, a fingerprint of the longer excited state, whereas the L spectrum features are wider pointing out a shorter excited state. No significant L_3/L_2branching ratio variation is detected across the phase transition.

4.2 V 3p CIS spectroscopy of VO_2 thin films.

In the previous section, the CIS spectroscopy of two valence band features (C and L) have been discussed across the phase transition. In this section, the resonating behaviour of the V $3p_{1/2}$ and $3p_{3/2}$ electrons across the V L edges have been investigated.

V 3p electrons can be found at ~41 eV of BE (see Figure 4.2.1). The lineshape is quite broad since the multiplet effect splits the V 3p levels into two components: V $3p_{1/2}$ and $3p_{3/2}$ similar to the V *2p* electrons. In this case, however, the spin-orbit splitting is quite small and the fitting procedure based on the same criteria discussed in Chapter 2 is necessary to separate the two components. The V $3p_{1/2}$ and $3p_{3/2}$ components have been modelled using a pseudo-Voigt curve[98] fixing their intensity ratio to 0.5, while for the background we used the Shirley curve. The fit returns the V $3p_{1/2}$ component at BE=43.6 eV and the $3p_{3/2}$ at BE=41.2 eV. The Spin-Orbit splitting (2.4 eV) is higher respect to the value of 1 eV estimated by Zimmerman and co-workers[107].

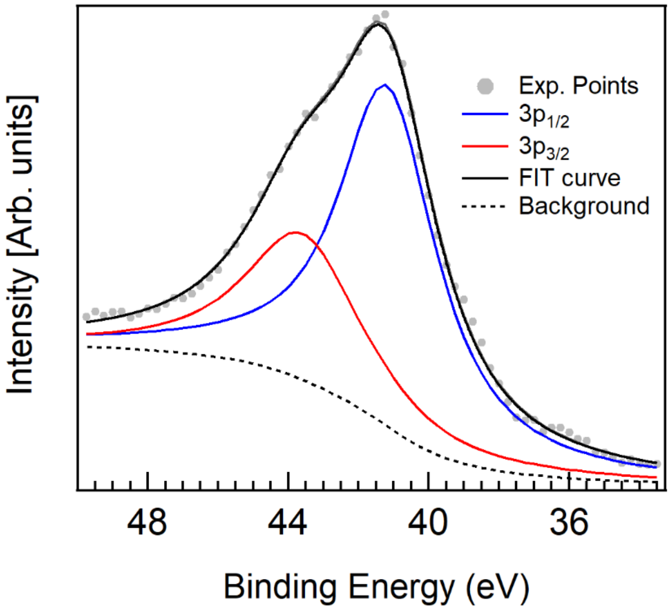

Figure 4.2.1: V 3p XPS spectrum of the 8 nm (-24 °C) films collected with hv=510 eV. The experimental points (grey dots) are compared to the fit (blue $3p_{1/2}$) and (red $3p_{3/2}$) and the continuous black line. Spectra acquired using hv=510 eV.

Exploiting these results, the CIS spectra of the $3p_{1/2}$ (BE=43.6 eV) and $3p_{3/2}$ (BE=41.2 eV) features have been obtained. For sake of brevity, the CIS spectra of the $3p_{1/2}$ and $3p_{3/2}$ components will be called $CIS_{1/2}$ and $CIS_{3/2}$ respectively. The $CIS_{3/2}$ spectra are depicted in Figure 4.2.2.

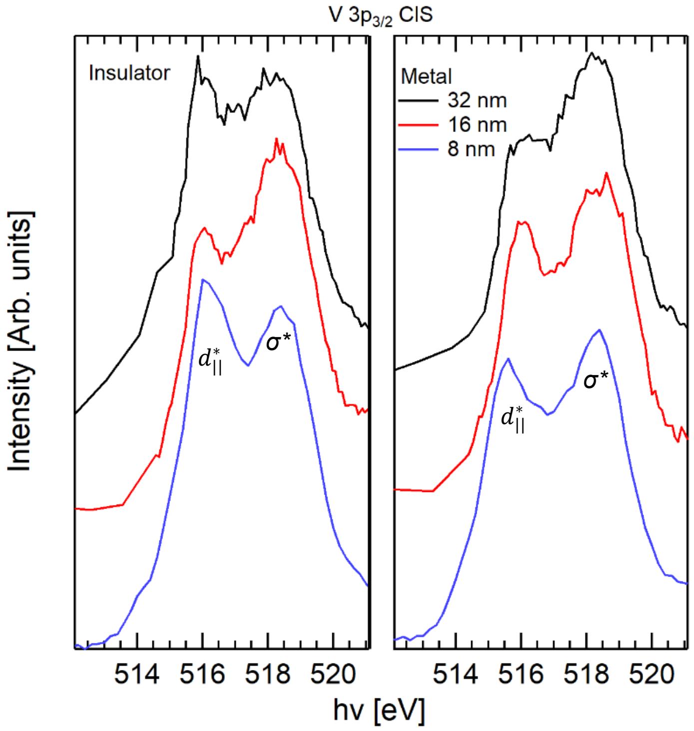

Figure 4.2.2: CIS$_{3/2}$ spectra (BE=41.2 eV) in the photon energy range 512.1-521.1 eV for the 32, 16 and 8 nm films (black, red and blue line, respectively). Left panel: the insulating phase; right panel: the metallic phase.

The V 3p$_{3/2}$ spectra exhibit a strong enhancement of the pre-edge feature respect to the V *3d* CIS spectra. This is due to the large overlap among 3p and *3d* orbitals, which may favour the decay $2p^5 3d^2$ -> $2p^6 3p^5 3d^1$ + e_p of the photo-excited state. The intensity of the CIS$_{3/2}$ spectra contributes also the incoherent fraction of the Auger V $L_3M_{23}M_{45}$. As depicted in Figure 2.2.5 the latter is present in the kinetic energy region 462-477 eV. For example, using the photon energy of 516 eV the V 3p$_{3/2}$ outgoing photoelectron has the energy of 474.8 eV, which means that the incoherent contribution from the two-holes Auger decay is present. According to the analysis carried out in the previous section, the two feature of the CIS$_{3/2}$ spectra of the metallic phase can be assigned to the $d^*_{||}$ (515.8-516 eV) and σ* (518.4 eV) empty bands. Their intensity ratio ($d^*_{||}$/σ*) increases with the strain in agreement with what observed in the V *3d* (C) CIS spectra and the strain-induced orbital occupancy at the Fermi level, by shifting up the $d^*_{||}$ while lowering the π*band. In addition the $d^*_{||}$ and σ* features are separated by 2.4-2.6 eV which ~~is~~ in good agreement with the $d^*_{||}$-σ*split observed in the *3d* C CIS spectra.

In the insulating phase, $d^*_{||}$ (515.9 eV) and σ* (518.3 eV) bands are clearly separated by 2.4 eV in agreement with XANES results found in the literature[61]. Contrary to the metallic spectra, the $d^*_{||}$/σ* intensity ratio is not correlated with the strain: it is ~1 for the 32 nm film, < 1 for the 16 nm film and > 1 in the 8 nm film. In addition across the MIT the $d^*_{||}$ feature decreases in intensity for the 8 and the 32 nm films, while increases for the 16 nm film. This anomalous behaviour is observed also in the CIS$_{1/2}$ spectra shown in Figure 4.2.3.

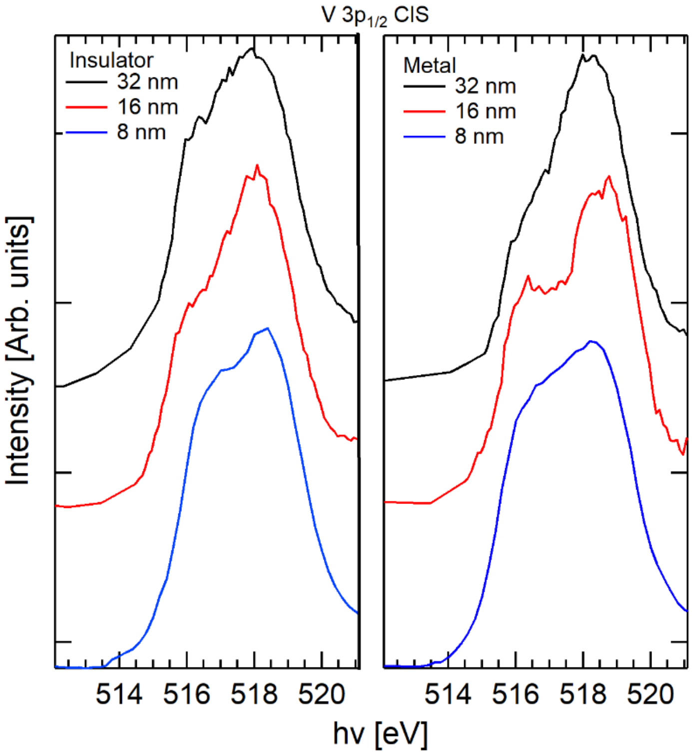

Figure 4.2.3: CIS$_{1/2}$ (BE=43.6 eV) spectra in the photon energy range 512.1-521.1 eV for the 32, 16 and 8 nm films (black, red and blue line respectively). Left panel: insulating phase; right panel: metallic phase.

The line-shape is different with respect to the CIS$_{3/2}$ spectra. The spectra of the metallic phase strongly resemble the L$_3$ edge of the XANES spectra. An unresolved feature is observable at ~516 eV, which intensity increases with strain. This behaviour is typical of the $d_{||}^{*}$ feature. In the insulating phase, spectra are dominated by two main features: one at 518.1 eV and one at 516.7 eV. The energy position does not match that of the $d_{||}^{*}$ and σ* features observed in the CIS$_{3/2}$ spectra as can be seen in Figure 4.2.4. The CIS spectra of the 8 nm film (insulating phase) have been chosen since the differences are clearly evident. The pre-edge peak of the CIS$_{1/2}$ spectrum is shifted toward higher energies respect to the CIS$_{3/2}$ spectra, pointing out that the excited states associated with the Auger decay of the 3p$^{3}_{3/2}$ and the 3p$^{1}_{1/2}$ final states are different. At the resonance of the L$_3$ edge, the only electrons available for the XANES excitation are the *2p*$_{3/2}$. Because of the dipole selection rules, the total angular momentum of the excited electrons is J=5/2 or J=1/2. Depending on the J value, the electron is excited in the specific empty band with the proper symmetry.

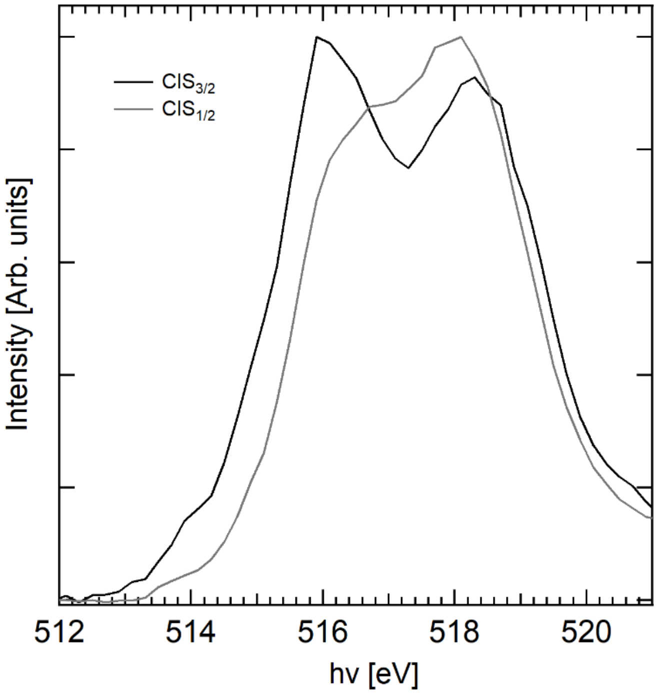

Figure 4.2.4: CIS spectra of the V 3p$_{3/2}$ (black) and V 3p$_{1/2}$ features (grey) for the 8nm film in the insulating phase.

This may result in a preferential decay of the excited state in the V *3p$_{3/2}$* or *3p$_{1/2}$* depending on the final state symmetry. To confirm this hypothesis a specific theoretical model for the resonant Auger decay of VO$_2$ is necessary.

4.3 CIS investigation of VO_2 disordered NS film

The conclusions drawn in the previous sections, relay on the strained samples ordered atomic lattice, which produces an electronic structure with characteristic fingerprints. In the case of a disordered sample, the Jahn-Teller distortion affects the orbital energetic order, making hard to recognize specific orbital features. In this section, CIS spectroscopy has been used to recognise the orbitals' features of MIT in a disordered VO_2 sample. The CIS spectra of the V *3d* $\underline{C}$ and $\underline{L}$ features along with the $CIS_{1/2}$ and $CIS_{3/2}$ spectra are showed in Figure 4.3.1.

The V *3d* $\underline{C}$ CIS spectra are the most severely affected by crossing the MIT. In the insulating phases, two features are clearly recognized: β (517.6 eV) and γ (519 eV). However, the line shape suggests the presence of two additional features at hv=516 eV and hv=518.5 eV. The maximum intensity (β feature) is found at 517.6 eV while for the ordered samples is shifted by 0.8 eV toward higher photon energies, in correspondence of the σ* peak (518.4 eV). Based on the $\underline{C}$ CIS results obtained in section 4.1 and on the presence of the Jahn-Teller distortion, the t_{2g} and e_g characters can be assigned to β and γ, respectively.

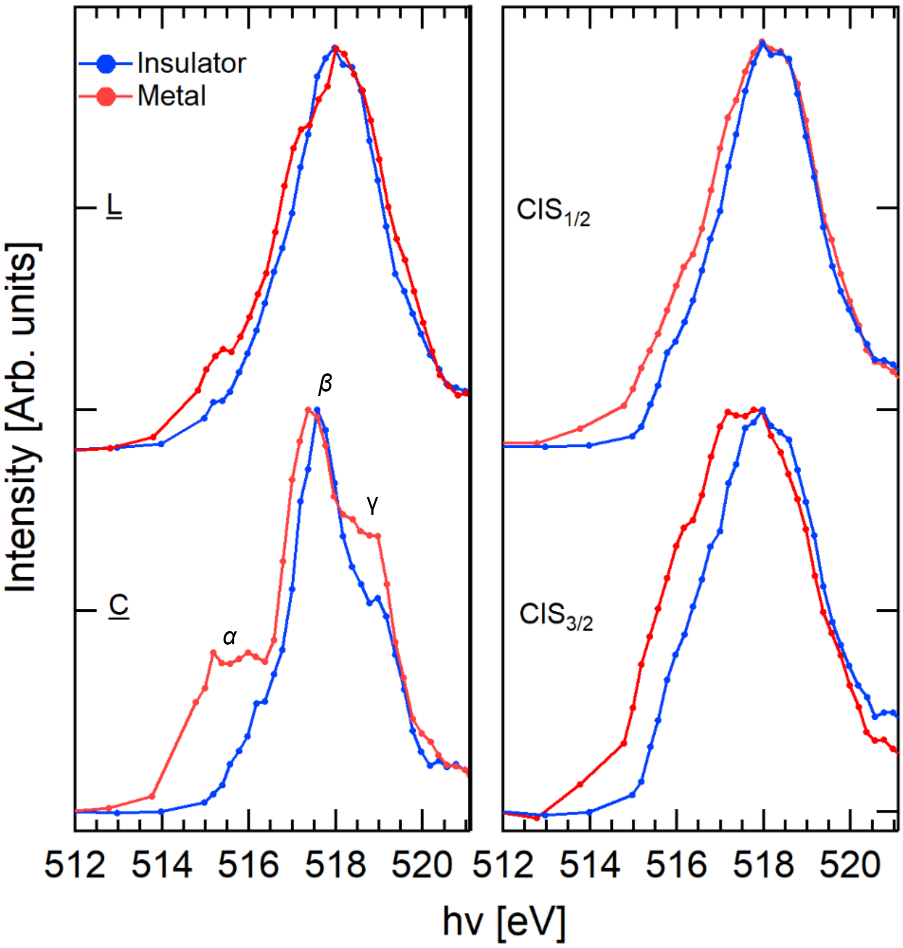

Figure 4.3.1: CIS spectra of the metallic (red) and insulating (blue) phases of the disordered NS sample in the range: 512-521.1 eV. Left panel, V 3d CIS spectra: top, $\underline{L}$ feature (BE=1.5 eV); bottom $\underline{C}$ feature (BE=0.4 eV). Right panel, V 3p CIS spectra: top, V $3p_{1/2}$ feature (BE=43.6 eV); bottom V $3p_{3/2}$ feature (BE=41.2 eV). The spectra are normalized to the incident photon flux and to their maximum intensity.

The energy mismatch between γ and σ* as well as the interpretation of the β feature position, can be understood considering a severe distortion of the ligand octahedral complex. The oxygen octahedron is formed by 3 L-M-L (ligand-metal-ligand) units, which share the same metal atom. Within a unit, the ligand atoms lay on the same axis. When one of the L-M-L units is bent in such a way that the angle θ between the two ligand atoms is less than 180° the t_{2g} and e_g degeneracy is lifted as showed in Figure 4.3.2. Reducing θ, i.e., increasing the bending, one of the 2 e_g orbitals is down-shifted in energy, while two of the 3 t_{2g} orbitals are shifted upwards [136]. The total effect is the reduction of the t_{2g}-e_g energy split. In this framework, if β and γ have t_{2g} and e_g character, respectively, their energy separation has to be smaller of the separation of the ordered samples. The β and γ features are separated by 1.6 eV, which is smaller than the ordered sample π*- σ* energy separation (2.4 eV) measured at the O K edge XANES in section 3. In addition, the β-γ energy separation has the same value of the π*- σ* energy distance measured at the O K edge of the NS sample. This suggests the correspondence between ~~the~~ β-γ and π*-σ* with β having the t_{2g} character and γ the e_g one.

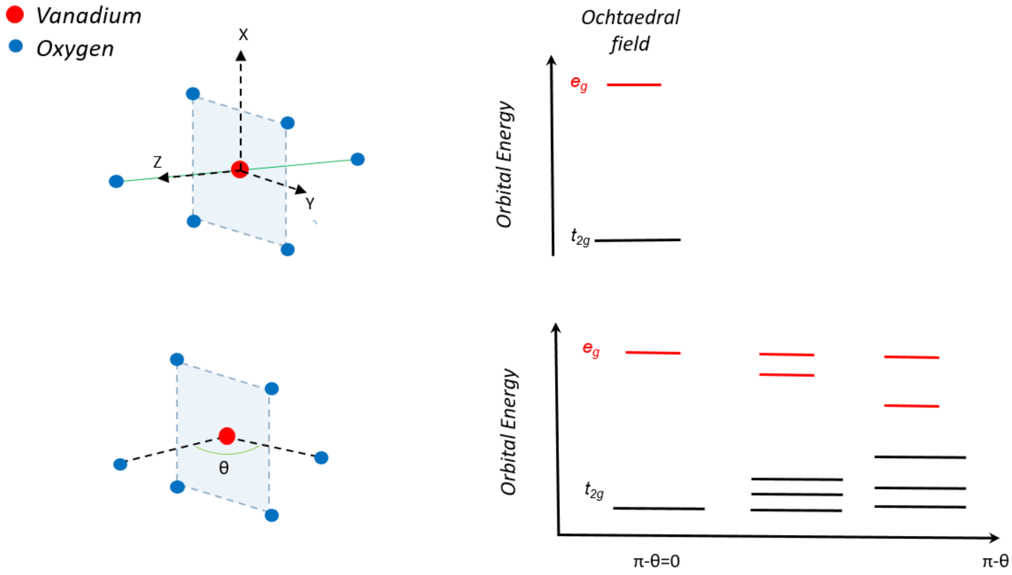

Figure 4.3.2: Schematic representation of the empty orbitals energy landscape (t_{2g} black, e_g red) in relation to the geometric distortion of the ligand octahedron. Top: undistorted octahedron and relative energy diagram; bottom bending of one L-M-L unit and its orbital energy scenario.

Despite the Jahn-Teller distortion described above have been identified as the main cause of the reduced t_{2g}-e_g energy separation, the presence of additional distortions acting at the same time but on different units cannot be ruled out. For example, the elongation or compression of the L-M distance within a unit may affect simultaneously the L-M-L bending, or different units may be bent with different angles. To rule out the existence of other possible effects a theoretical model is necessary.

Across the phase transition, the appearance of the α feature is accompanied by the increase in the γ intensity. Actually, since the CIS spectra are normalized to the maximum of the β feature intensity the spectral changes have to be interpreted as the transfer of the spectral weight from β to α. The latter can be seen as one of the t_{2g} orbital not degenerate with the other two (β) present in the metallic phase. The increase in the intensity of the γ feature is a consequence of the β-> α spectral transfer. A shift of the β peak of 0.2 eV toward lower photon energy is also observed. This interpretation matches the band model proposed in Chapter 3 (see Figure 3.2.11) and it is coherent with XANES and ResPES results.

The L CIS spectrum is broader (as discussed in section 4.1) respect to the C CIS spectrum and, as a consequence, the spectral features are not well resolved. In the insulating phase, the maximum intensity shifts from 517.6 (C) to 518 eV (L), suggesting the increase of the spectral components with e_g character. Across the phase transition, the α feature is still detectable despite the reduction respect to C spectra underlying the reduced sensitivity of the L photoemission channel to t_{2g} spectral components. In the metallic phase, the β component can be resolved with respect to the main peak at 518 eV. Moreover, the maximum intensity does not shift across the MIT confirming that spectral weight is not transferred among empty orbitals with e_g and t_{2g} character.

Between the V 3p photoemission channels, the major changes across the MIT are showed by $CIS_{3/2}$. In the metallic phases, three peaks can be recognized at the photon energies of 517.7, 517.2 and 516 eV. These three features lay in energy regions where empty orbitals with t_{2g} character have been identified in C and L CIS spectra. This result suggests that $CIS_{3/2}$ is particularly sensitive to empty t_{2g} orbitals and it is consistent with the severe broadening of the $CIS_{3/2}$ spectrum of the metallic phase respect to that of the insulating phase, which also underlines the redistribution of the empty orbitals across the phase transition. In addition, the three features observed in the $CIS_{3/2}$ spectra can be correlated to those present in the XANES difference spectra in Chapter 3 (see Figure 3.1.10). The $CIS_{1/2}$ spectrum is quite broad and does not exhibit outstanding features. Across the MIT the transfer of the spectral weight in the energy region of the empty t_{2g} orbitals is observed in agreement with ~~the~~ other CIS spectra. However, the magnitude is quite small respect to the $CIS_{3/2}$ spectra, suggesting that also in the disordered NS film the excited state may exhibit a different angular momentum symmetry and, therefore, a different coupling with the final state.

In conclusion, it has been shown that CIS spectroscopy is a versatile tool to collect XANES spectra of selected partial electron yield. The possibility to choose among different photoemission channels allows us to recognize and to identify specific empty orbitals involved in the MIT. In addition, the CIS investigation of the NS sample confirms the band model proposed in chapter 3. It underlines also the fundamental role of the mutual electron interaction in the VO_2 phase transition.

Conclusions

Among the many stimulating TM oxides, VO_2 deserves a special mention: it is really a fascinating material that since its discovery triggered researches and still now offers plenty of opportunities to understand the physics of correlated systems. In addition, it offers many opportunities for applications in different fields. It undergoes a MIT near room temperature coupled with a structural phase transition from the low-temperature monoclinic insulator phase to the high-temperature rutile metal phase. The nature of the MIT is still under debate since different mechanisms like electron correlation driven Mott-Hubbard transition or structurally driven Peierls transition or a combination of both have been considered. The path leading to the full exploitation of the MIT feature for VO_2-based technologies is still in the early stages and a deeper understanding of the nature of the phase transition is required.

In this thesis, the interplay and the dynamics of the orbital, structural and electronic degree of freedom across MIT have been studied using advanced spectroscopic techniques. In order to observe the interplay of the lattice structure with the orbital dynamic across the MIT, three strained single crystalline $VO_2/TiO_2(001)$ thin and ultra-thin films, synthesized using Molecular Beam Epitaxy (MBE) and NS disordered films synthesized using Supersonic Cluster Beam Deposition (SBCD) have been investigated and compared. The strain effect resulted in a reduction of the c_r parameter with a concurrent increase of the apical V-O distance. Studying these films across the MIT, it has been possible to investigate the effect of the decrease of the V *3d*-O *2p* wave functions overlap and the induced modifications to the orbital arrangements by the crystal field.

To summarize, in this thesis I demonstrated that:

1. Using SCBD it is possible to tune the oxidation state of the VO_x NS films. As a consequence, 3d occupancy and Work Function (WF) can be modulated. In addition, because of the nanogranular nature of the NS films, quantum confinement can be exploited to increase the WF respect to the bulk materials.

Actually, I was able to grow at room temperature NS vanadium oxides films with a tunable oxidation state and they were systematically investigated using in-situ Auger spectroscopy, looking at the VO_x 3d occupancy as a function of the stoichiometry. From the analysis of the Auger line-shape, we quantitatively correlated the *3d* DOS spectral weight with the oxygen concentration. Results confirm the failure of the ionic picture to describe the *3d* occupancy in NS vanadium oxides, and the role of the hybridization in the VO_x NS films. We have shown that the fraction of unpaired *d* electron exhibits a linear dependence from the oxygen content, that points out strong *4s-3d* ($x<1$) and *3d-2p* ($x>1$) hybridizations varying with the stoichiometry. Based on our data we propose a heuristic model, which links the outer valence branching ratio with the stoichiometry, giving a role to the V 3d-O 2p hybridization in all VO_x films. In addition, we observed the occurrence of a linear correlation between the WF and the stoichiometry in the investigated range $0.5<x<2.45$.

For different stoichiometry, the NS films WF have been observed to be systematically higher respect to the corresponding WF of bulk vanadium oxides. This has been interpreted as a quantum confinement effect due to the synthesis conditions of the NS films. In fact, SCBD is a low kinetic energy deposition technique, in which the nanoparticles maintain their individual character upon landing on the substrate. As a consequence, the NS films grow without coalescence effects, i.e. the nanoparticles are assembled together retaining a “memory” of the small size of their gas-phase precursors. This “memory effect” clarified the nanograin structure of these films pointing out a mechanism of quantum confinement enhancement of the WF value. By controlling the oxidation state degree of freedom and accessing the nanoscale, we demonstrated the unique capability of our approach to synthesize NS films with a tunable WF from 3.7 up to 7 eV, which can be exploited to grow at room temperature hole or electron injection layers for technological applications. As a consequence, the SCBD appears as an effective and reliable method to control the electronic structure and the work function of NS films.

2. A systematic XANES investigation of VO_x NS films revealed that they are disordered, this allowed to synthetize NS disordered VO_2 samples.

For all NS films we systematically studied via in-situ XANES measurements the local arrangements of oxygen atoms around vanadium as a function of the stoichiometry. Actually, NS VO_x samples produced using the PMCS apparatus are disordered with oxygen atoms arranged in randomly distorted octahedra around vanadium atoms. Nevertheless, the ability to synthetize samples with a tunable stoichiometry allowed us to obtain specific VO_2 disordered samples, in which the Peierls distortion mechanism is quenched because of the lack of the long-range lattice periodicity.

3. XANES (Auger yield) investigation of strained VO_2 samples allowed us to observe spectral changes across the MIT which are compatible with the π^*- $d_{||}^*$ inversion in the metallic state and π^*- $d_{||}^*$ separation in the insulating state. In the NS sample, the MIT involves mainly empty orbitals with t_{2g} character.

By means of XANES spectroscopy collected with two different Auger emission lines (V $L_3M_{23}M_{45}$ and O $KL_{23}L_{23}$) and ResPES, I also characterized the strain-induced orbital dynamic across the MIT. These spectroscopies that do not require long-range ordered samples allowed to compare the transition features of the crystalline samples with those of the NS samples. In particular, XANES spectra collected with the Auger O $KL_{23}L_{23}$ allowed studying the O K edge line shape minimizing the interference from V L edges. This improved oxygen sensitivity helped to identify trends in the orbital occupancy and the relative energy changes as a function of the sample thickness. As the strain increase also the π^*-$d_{||}^*$ orbitals split increases in the insulating phase, while in the metallic phase the spectral changes are compatible with an inversion of the π^* and $d_{||}^*$ orbital occupancy at the FL respect to the bulk VO_2. Finally, a redshift of the Turning Point of the difference spectra has been observed. In NS samples the major spectral changes across the MIT are observed in the π^* (t_{2g} *) region, a behaviour that is compatible with the Mott-Hubbard model for the MIT transition.

4. From ResPES measurements it appears that tuning the strain it is possible to control also the metallicity of the sample. In addition, an electron correlation driven MIT is observed in the NS sample in which the bandgap is closed by the collapse of a t_{2g}* band to FL.

Using ResPES, spanning the photon energy across the V $L_{2,3}$ edges, I showed that only the unpaired 3d electrons are involved in the MIT. We observed also the appearance of a Fermi edge in the crystalline strained samples and a small but finite DOS at the FL in NS samples. From the measure of the screening parameters ratio (L_m/L_i) a decrease of the sample metallicity increasing the strain is detected. Also the NS film exhibits $L_m/L_i > 1$ confirming the occurrence of the MIT.

From the combination of XANES and ResPES measurements, we can conclude that an electron correlation mechanism is responsible of the MIT in VO_2. In disordered NS samples in which the Peierls transition is suppressed, the electron correlation driven MIT involves mostly t_{2g} empty orbitals. ResPES measurements confirm the finite DOS at the FL and the collapse and the subsequent occupation of the t_{2g}* in the metallic phase in agreement with the XANES spectra. However, from the analysis of the strained and ultra-strained films, it is clear that the sample structure modulates the MIT properties. In particular, the change of the multi-orbital contribution to the phase transition as a function of the thickness (i.e. strain) is reflected in the XANES spectra. Coupling these results with the decrease of the metallicity in strained films respect to the bulk-like VO_2 shows that the lattice order is of fundamental importance in tuning the MIT.

5. Exploiting CIS spectroscopy it has been possible to track the orbital dynamic across the MIT. In the metallic phase of the ordered samples, increasing the strain an increase of the $d_{||}^*$ along with a decrease of the π^* signal has been observed. This points out an inversion of the π^*-$d_{||}^*$ band. In the NS film, CIS spectroscopy shows the collapse of one of the t_{2g}* band to FL confirming the band model proposed for the disordered sample phase transition.

With this technique, I identified the different orbital contributions to the MIT as a function of the structure. In the ordered samples, in the metallic phase, it has been shown the correlated increase of the $d_{||}^*$ band while increasing the strain, accompanied by the concurrent decrease of the π* orbital signal. This dynamic is compatible with a strain-induced population inversion at the FL in metallic VO_2. Moreover, the CIS investigation of NS disordered samples allowed to track the transfer of the spectral weight among t_{2g}* orbitals across the MIT, confirming the band model proposed for a phase transition of a disordered VO_2 sample.

The results of this thesis confirm that the MIT in a disordered sample is driven by electron-electron correlation. However, the lattice order parameter, which is not strictly necessary to trigger the phase transition, is also fundamental to tune and control MIT features such as the FL population, i.e., the metallic properties and the orbital occupancy.

Appendix 1.

XPS and UPS

Shining a sample with a photon beam with enough energy results in the emission of electrons. The detection of the photo-emitted electrons as a function of their kinetic energy is called PhotoElectron Spectroscopy or PES. X-ray photoelectron spectroscopy (XPS) and Ultra-violet photoelectron spectroscopy (UPS) are two kinds of PES, where a photon beam with energy in the X-ray region and Ultra-Violet region respectively, is used to ionize the sample.

PES is basically exploitation of the photoelectric effect and it can be described with a transition from an initial bound state $|i\rangle$ with N electrons into a final state $|f\rangle$ with N-1 bound electrons and 1 free electron. For an unpolarised photons beam the cross-section of a photoemission process is given by[168]:

$$\sigma_{if} = \frac{4\pi^2 \alpha a_0^2}{3} hv \left|M_{if}\right|^2 \delta(E_i - E_f + hv) \tag{A1.1}$$

Where σ_{if} is the cross-section relative to the transition $|i\rangle$ -> $|f\rangle$, α is the fine structure constant, a_0 is the Bohr radius, *hv* is the photon energy, M_{if} is the matrix element and $\delta(E_i - E_f - hv)$ represents the conservation of energy.

M_{if} is calculated using perturbation theory, and within the dipole approximation it can be written as:

$$M_{if} = \left\langle f \middle| \sum_j r_j \middle| i \right\rangle \tag{A1.2}$$

Where r_j is the position of the j-th electron.

The energy conservation expressed in (A1.1) can be written as:

$$-hv = E_i - E_f = E_N - E_{N-1} - K_e \quad \Rightarrow \quad E_{N-1} - E_N = hv - K_e \tag{A1.3}$$

Where E_N is the energy of the initial state, E_{N-1} is the energy of the ionized target with N-1 electrons in the final state and K_e is the kinetic energy of the photoelectron. E_{N-1}- E_N is called Binding Energy (BE) and represents the energy of the photoelectron in the initial state when it is bound inside the solid. Very often the BE are calculated respect to FL level instead of the Vacuum level therefore equation A1.3 can be written as:

$$BE + WF = hv - K_e \tag{A1.4}$$

Where WF is the work function of the material, i.e. the energy difference between FL and the Vacuum level.

From equation A1.4 it can be seen how measuring the photoelectron kinetic energy it is possible to extract information on the sample. To study the photoemitted electrons from a core-level (high BE value) it is necessary to increase the energy of the photon beam. As a consequence XPS allows to study valence and core electrons, while UPS is limited to valence band investigation.

Despite XPS is able to probe the valence band of a material, UPS is often more used. This is due to the cross-section magnitude of the outer electrons. In general, the valence electrons cross-section is much smaller in the X-ray range respect to Ultra-violet.

UPS is also used to determine the Work function of a material. Biasing the sample it is possible to acquire the secondary electrons cut-off (BE relative to the emission of an electron with K_e=0 eV) and because of the high valence electrons sensitivity, FL is easily observable. The difference between the FL and the secondary electron cut-off determines the WF.

The access to the core-level makes XPS a powerful technique to investigate the chemical nature of the sample. In fact, every chemical element has a unique set of energy levels with characteristics binding energies.

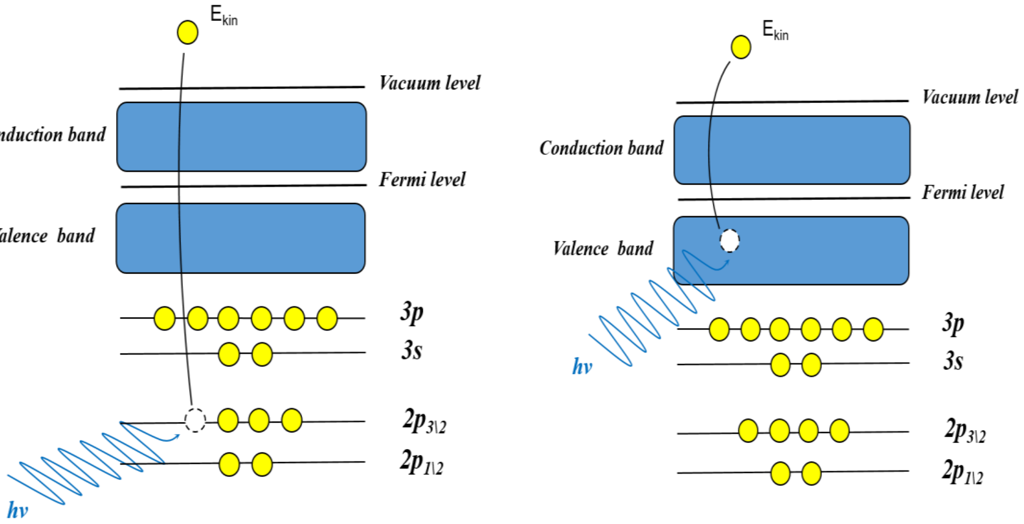

Figure A1.1: Schematic representation of core-level XPS (left panel) and Valence band UPS (right panel).

XPS is also sensitive at what is called chemical shift. The chemical shift is the variation of the BE observed when an element form inequivalent chemical bonds. Depending on the nature of the chemical bond, an atom can yield or receive valence electrons which affect the screening of the positive nucleus. For example, in VO_2 vanadium shares 4 electrons with the 2 oxygen atoms. This results in a reduction of the effective negative charge around the vanadium atom and therefore in a reduced ability to screen the positive charge of the nucleus. Consequently, the core-levels in VO_2 are slightly more bound, i.e. higher BE, respect to the case of pure V. the chemical shift can be detected using XPS making possible to discriminate between different oxidation state of a metal oxide or to identify how the elements of the samples are chemically bounded. XPS has been used in section 2.2.3 to determine the oxidation state of NS VO_x films.

Final state effects may also affect the kinetic energy of the photoelectron that going out from the solid can leave the system in an excited state. The spectrum of the accessible excitations strongly depends on the material properties, for example, plasmon excitation, shake up and the contribution from different screening mechanisms can be observed. A complete description of all the possible final state effects is beyond the purpose of this thesis and we refer to the literature for detailed information[168].

As a consequence of the photoemission process, the system is left with a hole in a core-level. This configuration is not stable and the positive attraction of the core hole induces the decay from an electron of an upper level in order to minimize mechanisms can be observed: radiative and Auger.

In the radiative channel, the electronic transition is followed by the emission of an X-ray photon.

In the Auger decay, the electronic transition form an upper level is followed by the emission of an electron, leaving the system in a two-holes final state.

Auger decays electrons are labelled as XYZ according to which electrons are involved. X represents the level of the core hole caused by direct photoemission, Y indicates the level of the electron that decay at the core hole level and Z is the electron emitted.

Two different conventions are used: X, Y and Z may directly indicate the energy level of the electron involved in the Auger decay. In this case, the Auger process depicted in Figure A1.2 can be written as $2p_{3/2}$3pV. The letter V is often used to indicate a valence electron.

Or as an alternative, the energy levels can be labelled according to the X-ray absorption notation in which a letter replace the principal quantum number and a numerical subscript indicate the total angular momentum component: 1s->K, 2s-> L_1, $2p_{1/2}$-> L_2, $2p_{3/2}$-> L_3, etc.

This is the notation used in this thesis. The Auger process depicted in Figure A1.2 is labelled as $L_3M_{2,3}V$.

Auger electrons have the properties to be emitted with kinetic energy independent from the incident photon energy. In fact, the kinetic energy of an Auger electron depends only on the difference between the energy levels involved during the decay process as described from Eq A2.1.5 for the decay $L_3M_{2,3}V$.

Where K_A is the kinetic energy of the Auger electron. Because of this property, Auger electrons are a fingerprint of material, but they can also be used to extract information on the electronic structure of the sample. For example, in section 2.2.4 the Auger decay $L_3M_{2,3}M_{4,5}$ has been studied for different VO_x films. Since in vanadium oxides, a fraction of *3d* electrons are bound with oxygen atoms, while the rest is unpaired the decay channel $L_3M_{2,3}M_{4,5}$ exhibits two lobes which intensity changes with the oxygen content. Two main decay mechanisms can be observed: radiative and Auger.

In the radiative channel, the electronic transition is followed by the emission of an X-ray photon.

In the Auger decay, the electronic transition form an upper level is followed by the emission of an electron, leaving the system in a two-holes final state.

Auger decays electrons are labelled as XYZ according to which electrons are involved. X represents the level of the core hole caused by direct photoemission, Y indicates the level of the electron that decay at the core hole level and Z is the electron emitted.

Two different conventions are used: X, Y and Z may directly indicate the energy level of the electron involved in the Auger decay. In this case, the Auger process depicted in Figure A1.2 can be written as $2p_{3/2}$3pV. The letter V is often used to indicate a valence electron.

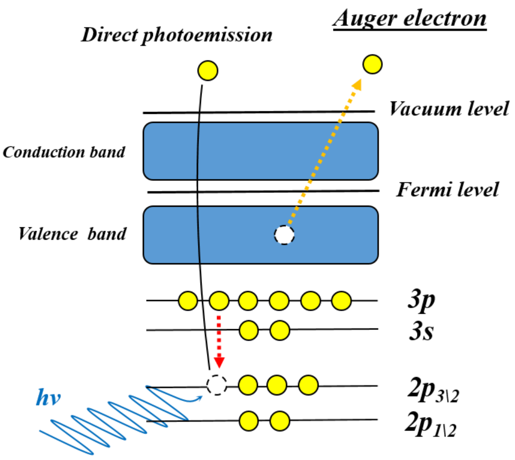

Figure A1.2: Schematic representation of the emission of an Auger electron following the core-level direct photoemission. The Auger channel depicted is the $L_3M_{2,3}V$.

Or as an alternative, the energy levels can be labelled according to the X-ray absorption notation in which a letter replace the principal quantum number and a numerical subscript indicate the total angular momentum component: 1s->K, 2s-> L_1, $2p_{1/2}$-> L_2, $2p_{3/2}$-> L_3, etc. This is the notation used in this thesis. The Auger process depicted in Figure A1.2 is labelled as $L_3M_{2,3}V$.

Auger electrons have the properties to be emitted with kinetic energy independent from the incident photon energy. In fact, the kinetic energy of an Auger electron depends only on the difference between the energy levels involved during the decay process as described from Eq A2.1.5 for the decay $L_3M_{2,3}V$.

$$K_A = BE_{2p_{3/2}} - BE_{3p} - BE_V \tag{A1.5}$$

Where K_A is the kinetic energy of the Auger electron. Because of this property, Auger electrons are a fingerprint of material, but they can also be used to extract information on the electronic structure of the sample. For example, in section 2.2.4 the Auger decay $L_3M_{2,3}M_{4,5}$ has been studied for different VO_x films. Since in vanadium oxides, a fraction of *3d* electrons are bound with oxygen atoms, while the rest is unpaired the decay channel $L_3M_{2,3}M_{4,5}$ exhibits two lobes which intensity changes with the oxygen content.

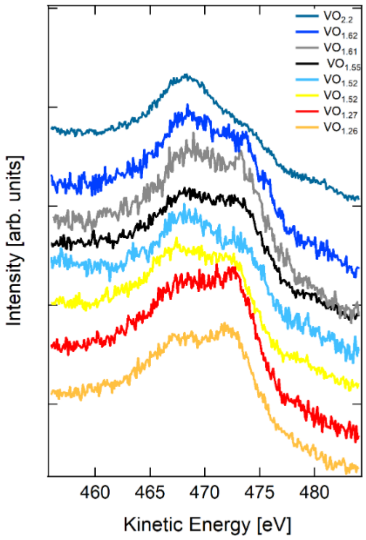

Figure A1.3: Auger $L_3M_{2,3}M_{4,5}$ for different VO_x NS films.

Work Function measurements

Within the photoemission techniques, WF measurements deserve special attention. It is well known that the sample WF does not influence photoemission measurements since only the analyzer WF enters in the conservation of energy [117].

The sample and the analyzer are placed in electrical contact, i.e. their FL are aligned. The photoelectrons ejected by the sample surface have to overcome an energy barrier which intensity is determined by the difference in WF between the sample and the analyzer as depicted in Figure A1.4.

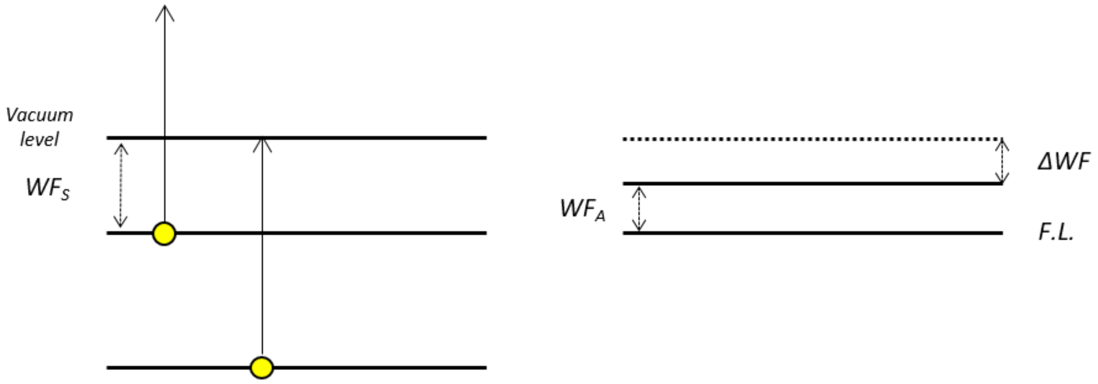

Figure A1.4: Schematic representation of a photoemission process. WF_s is the sample WF, WF_A the analyzer WF, $\Delta WF = WF_s - WF_A$.

In a real photoemission experiment, an additional term has to be considered in Eq. A1.4

$$K_e = hv - BE - WF_S + \Delta WF = hv - BE - WF_A \tag{A1.4}$$

Where $\Delta WF = WF_s - WF_A$, WF_s is the sample WF and WF_A the analyzer WF.

As a consequence, the sample's WF does not appear to enter the direct photoemission process. However, if FL is populated it is possible to set an internal energy reference imposing:

$$K_e(FL) = hv \tag{A1.5}$$

Where $K_e(FL)$ is the kinetic energy of the electrons at FL. Equation A1.5 consists of a rigid shift of the entire spectrum. In this way, the BE is calculated as:

$$BE = hv - K_e^* \tag{A1.6}$$

In which K_e^* is the Kinetic energy of the photoelectrons calculated considering Eq. A1.5.

On this scale the BE of FL is automatically set to 0 while the BE of the secondary electrons offset is set to:

$$BE_{SO} = hv - WF_s \tag*{(A1.6)}$$

Inverting the sample's WF can be extracted. It is necessary to point out that this method will work only for metallic samples since the FL population is required. However, it can be applied for semiconductor and insulating samples if it is possible to calibrate the analyzer with a metal. This will give us information about the position of the analyzer FL and consequently the possibility to calculate the WF also for semiconductor and insulating samples.

Appendix 2.

XANES

X-ray Absorption Near Edge Structure (XANES) is a spectroscopic technique that concerns the absorption of a photon and the consequent excitation of an electron into an empty band. The local character of core-level excitations allows investigating both the local structure and the unoccupied Density Of State (empty DOS).

XANES is the energetic region of the absorption spectra in which the excited electrons have a wavelength that is longer than the nearest neighbour distance. In this particular energetic region, which extends from 5 to 100 eV beyond the absorption threshold, the outgoing electron undergoes multiple scattering processes from the neighbour atoms [141,169,170]. The XANES signal is therefore very sensitive to geometry and symmetry of the atomic disposition inside the sample.

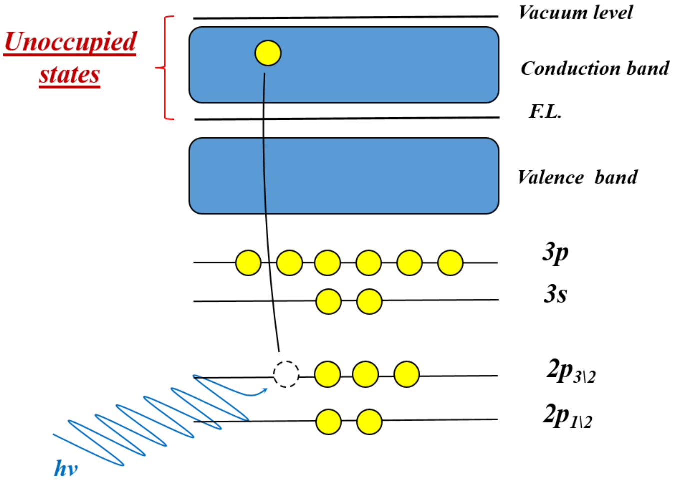

Figur3 A2.1: Schematic representation of the XANES process.

Using synchrotron radiation, it is possible to tune the photon energy hv to sweep across a core-level resonance of the system, for which the photo-absorption cross-section is maximum. According to quantum mechanics, the total absorption cross-section can be obtained using Fermi golden rule and dipole approximation. Therefore the finale state probed using XANES obeys to the dipole selection rule.

$$\sigma \; \alpha \; hv \sum_f \left|M_{if}\right|^2 \delta(E_i - E_f + hv) \qquad \text{(A2.1)}$$

Where *hv* is the photon energy, M_{if} is the matrix element and $\delta(E_i - E_f - hv)$ represents the conservation of energy. M_{if} can be calculated as:

$$M_{if} = \langle f^* | \textstyle\sum_j r_j \, |i\rangle \qquad \text{(A2.2)}$$

In which, $|i\rangle$ is the initial state with N bound electrons and $|f^*\rangle$ is the finale excited state with a hole in the core-level and one electron excited in an empty state. r_j is the position of the j-th electron.

For historical reasons, the absorption thresholds are named after the principal quantum numbers of the initial state. If n=1, absorption edges are K edges, if n=2 they are called L edges, n=3 M edges and so on. A subscript is also used to distinguish between the different subshell, therefore: L_1 absorption edge is acquired exciting 2s electron, L_2->$2p_{1/2}$ electrons and L_3->$2p_{3/2}$ electrons, etc.

XANES spectra can also be acquired using different detection techniques. A complete overview can be found in the literature[141]. In this thesis, particular attention is devoted to the different electron yields.

Total Electron Yield:

Total Electron Yield (TEY) acquisition method consists of tuning the photon energy across the system resonance and counting all the electrons which escape from the sample surface. This can be achieved by connecting the sample to the ground through an amperemeter and measuring the neutralization current. TEY signal is dominated by secondary electrons created as a consequence of the photoemission process. As a consequence it is the most bulk-sensitive detection technique among the electron yields, reaching probing depths of several nanometers[171]. TEY has been used in section 2.2.7 in order to investigate the stoichiometry and to probe the local structure of NS VO_x samples.

Auger Electron Yield:

Auger Electron Yield (AEY) is the measurements of the intensity of a specific decay channel of the core-hole as a function of the photon energy. The probing depth is limited by the mean free path of the Auger electrons, therefore it is a rather surface-sensitive technique. Choosing the appropriate Auger decay it is possible to probe the empty DOS with different sensitivity, making AEY an extremely versatile technique. In section 3.1 AEY has been used to study the evolution of the XANES spectra of VO_2 thin and nanostructured films across the MIT.

Constant Initial State:

Constant Initial State (CIS) spectroscopy consists of measuring the intensity variation of a direct photoemission peak as a function of the photon energy. This technique requires the ionization energy to be constant, i.e. the difference between the kinetic energy of the photoemitted electron and the photon beam must be constant. Similarly to AEY, CIS is extremely versatile since it is possible to study the intensity evolution of photoemission peak with a significant physical meaning. CIS spectroscopy has been used in chapter 4 to investigate the orbital contribution to the MIT for strained and disordered VO_2 films.

Appendix 3.

Resonant Photoemission

Resonant photoemission spectroscopy is a branch of photoelectron spectroscopy and in particular of variable energy photoemission spectroscopy. Historically XPS and UPS apparatus developed using X-ray lamp (Al Kα or Mg Kα) or noble gas lamp (He I and II) as ionization source therefore without the opportunity to finely tune the photon energy. The advent of synchrotron radiation provided a continuously tunable radiation source, with high intensity and controllable polarization.

The ability to vary the photon energy allowed to exploit cross-section effects to better extract the signal of interest from the investigated samples. Of particular interest is the resonant enhancement of the cross-section when the photon energy is tuned across a core-hole resonance. When the photon energy is tuned to match an absorption edge of the sample, two possible processes which lead to the same final state are possible: the direct photoemission and the Auger-like emission following the relaxation of a photo-excited state. As a consequence, an interference process takes place modulating the photoemission intensity of the resonating states as a function of the photon energy. In this thesis the samples analysed are VO_2 thin films and NS film, therefore this material will be taken as an example, however, the considerations derived are of general nature.

Tuning the photon energy across the VO_2 L_3 and L_2 edges a *2p* electron is excited in the partially empty *3d* subshell. The excited state will decay via Coulomb interaction, with a concurrent emission of an electron. This generates two identical final states,

summarized in Eq. A3.1 and A3.2, which constructively interfere modulating the photoemission intensity as a function of the photon energy.

$$2p^6 3d^n + h\nu \rightarrow 2p^6 3d^{n-1} + e^- \qquad \text{(A3.1)}$$

and the photo-absorption channel:

$$2p^6 3d^n + h\nu \rightarrow 2p^5 3d^{n+1} \rightarrow 2p^6 3d^{n-1} + e^- \qquad \text{(A3.2)}$$

The ResPES effect can be described as the production of an excited intermediate state, which decays through a Coster–Kronig (CK) or super-Coster–Kronig (SCK) process. Coherent superposition of channels in Eq. 3.2 and Eq. 3.3 can lead to resonant enhancement of the $3d^{n-1}$ final state[172]. Due to the local character of the ResPES process, it is possible to distinguish metal *3d*-like states in the valence band from those having ligand character disentangling the mixing between the different ground state configurations.

ResPES has been used in Chapter 3 in order to disentangle the O and V contribution in the valence band and to study the occupation of FL across the MIT.

Bibliography

[1] G.E. Moore, Cramming more components onto integrated circuits. In: Electronics, Electronics. (1965).

[2] D. Clark, Intel Rechisels the Tablet on Moore's Law, (2015). https://blogs.wsj.com/digits/2015/07/16/intel-rechisels-the-tablet-on-moores-law/.

[3] P.A. Lee, N. Nagaosa, X.G. Wen, Doping a Mott insulator: Physics of high-temperature superconductivity, Rev. Mod. Phys. (2006). doi:10.1103/RevModPhys.78.17.

[4] Y. Tokura, Y. Tomioka, Colossal magnetoresistive manganites, J. Magn. Magn. Mater. (1999). doi:10.1016/S0304-8853(99)00352-2.

[5] M. Brahlek, L. Zhang, J. Lapano, H.-T. Zhang, R. Engel-Herbert, N. Shukla, S. Datta, H. Paik, D.G. Schlom, Opportunities in vanadium-based strongly correlated electron systems, MRS Commun. 7 (2017) 27–52. doi:10.1557/mrc.2017.2.

[6] U. Schwingenschlögl, V. Eyert, The vanadium Magnéli phases VnO2n-1, Ann. Der Phys. (2004). doi:10.1002/andp.200410099.

[7] C.K. Chan, H. Peng, R.D. Twesten, K. Jarausch, X.F. Zhang, Y. Cui, Fast, completely reversible Li insertion in vanadium pentoxide nanoribbons, Nano Lett. (2007). doi:10.1021/nl062883j.

[8] N. Xu, X. Ma, M. Wang, T. Qian, J. Liang, W. Yang, Y. Wang, J. Hu, C. Yan, Stationary Full Li-Ion Batteries with Interlayer-Expanded V 6 O 13 Cathodes and Lithiated Graphite Anodes, Electrochim. Acta. (2016). doi:10.1016/j.electacta.2016.04.044.

[9] X. Shi, J. Du, T.G.J. Jones, X. Wang, H.P. Liang, Understanding the Mechanism for Capacity Decay of V 6 O 13 -Based Lithium-Metal Polymer Batteries, ACS Appl. Mater. Interfaces. (2018). doi:10.1021/acsami.8b10629.

[10] B. Fisher, J. Genossar, G.M. Reisner, Systematics in the metal-insulator transition temperatures in vanadium oxides, Solid State Commun. (2016). doi:10.1016/j.ssc.2015.10.015.

[11] F.J. Morin, Oxides which show a metal-to-insulator transition at the neel temperature, Phys. Rev. Lett. (1959). doi:10.1103/PhysRevLett.3.34.

[12] T. Yajima, T. Nishimura, A. Toriumi, Positive-bias gate-controlled metal-insulator transition in ultrathin VO2 channels with TiO2 gate dielectrics, Nat. Commun. (2015). doi:10.1038/ncomms10104.

[13] V.R. Morrison, R.P. Chatelain, K.L. Tiwari, A. Hendaoui, A. Bruhács, M. Chaker, B.J. Siwick, A photoinduced metal-like phase of monoclinic VO2 revealed by ultrafast electron diffraction, Science (80-.). (2014). doi:10.1126/science.1253779.

[14] J. Narayan, V.M. Bhosle, Phase transition and critical issues in structure-property correlations of vanadium oxide, J. Appl. Phys. 100 (2006) 103524. doi:10.1063/1.2384798.

[15] P. Jin, K. Yoshimura, S. Tanemura, Dependence of microstructure and thermochromism on substrate temperature for sputter-deposited VO2 epitaxial films, J. Vac. Sci. Technol. A Vacuum, Surfaces, Film. (1997). doi:10.1116/1.580439.

[16] D. Brassard, S. Fourmaux, M. Jean-Jacques, J.C. Kieffer, M.A. El Khakani, Grain size effect on the semiconductor-metal phase transition characteristics of magnetron-sputtered VO2 thin films, Appl. Phys. Lett. (2005). doi:10.1063/1.2001139.

[17] J.Y. Suh, R. Lopez, L.C. Feldman, R.F. Haglund, Semiconductor to metal phase transition in the nucleation and growth of VO 2 nanoparticles and thin films, J. Appl. Phys. (2004). doi:10.1063/1.1762995.

[18] L. Fan, F. Wang, X. Chen, Z. Liu, C. Ma, L. Zhu, Q. Meng, B. Wang, Q. Zhang, C. Zou, Well-Dispersed Monoclinic VO 2 Nanoclusters with Uniform Size for Sensitive near-Infrared Detection , ACS Appl. Nano Mater. (2018). doi:10.1021/acsanm.8b01126.

[19] R. Lopez, T.E. Haynes, L.A. Boatner, L.C. Feldman, R.F. Haglund, Size effects in the structural phase transition of VO2 nanoparticles, Phys. Rev. B - Condens. Matter Mater. Phys. (2002). doi:10.1103/PhysRevB.65.224113.

[20] E.U. Donev, J.I. Ziegler, R.F. Haglund Jr, L.C. Feldman, Size effects in the structural phase transition of VO 2 nanoparticles studied by surface-enhanced Raman scattering, J. Opt. A Pure Appl. Opt. 11 (2009) 125002. doi:10.1088/1464-4258/11/12/125002.

[21] J. Jeong, Z. Yong, A. Joushaghani, A. Tsukernik, S. Paradis, D. Alain, J.K.S. Poon, Current induced polycrystalline-to-crystalline transformation in vanadium dioxide nanowires, Sci. Rep. (2016). doi:10.1038/srep37296.

[22] J.G. Ramirez, T. Saerbeck, S. Wang, J. Trastoy, M. Malnou, J. Lesueur, J.P. Crocombette, J.E. Villegas, I.K. Schuller, Effect of disorder on the metal-insulator transition of vanadium oxides: Local versus global effects, Phys. Rev. B - Condens. Matter Mater. Phys. 91 (2015). doi:10.1103/PhysRevB.91.205123.

[23] Z. Luo, Z. Wu, X. Xu, T. Wang, Y. Jiang, Electrical and optical properties of nanostructured VOX thin films prepared by direct current magnetron reactive sputtering and post-annealing in oxygen, Thin Solid Films. (2011). doi:10.1016/j.tsf.2011.03.003.

[24] Y. Muraoka, Z. Hiroi, Metal-insulator transition of VO2 thin films grown on TiO 2 (001) and (110) substrates, Appl. Phys. Lett. (2002). doi:10.1063/1.1446215.

[25] H. Futaki, M. Aoki, Effects of Various Doping Elements on the Transition Temperature of Vanadium Oxide Semiconductors, Jpn. J. Appl. Phys. (1969). doi:10.1143/jjap.8.1008.

[26] M. Jerry, W.Y. Tsai, B. Xie, X. Li, V. Narayanan, A. Raychowdhury, S. Datta, Phase transition oxide neuron for spiking neural networks, in: Device Res. Conf. - Conf. Dig. DRC, 2016. doi:10.1109/DRC.2016.7548503.

[27] M.D. Pickett, G. Medeiros-Ribeiro, R.S. Williams, A scalable neuristor built with Mott memristors, Nat. Mater. (2013). doi:10.1038/nmat3510.

[28] N. Shukla, A. V. Thathachary, A. Agrawal, H. Paik, A. Aziz, D.G. Schlom, S.K. Gupta, R. Engel-Herbert, S. Datta, A steep-slope transistor based on abrupt electronic phase transition, Nat. Commun. (2015). doi:10.1038/ncomms8812.

[29] J. Lin, S. Ramanathan, S. Guha, Electrically driven insulator-metal transition-based devices - Part I: The Electrothermal model and experimental analysis for the dc characteristics, IEEE Trans. Electron Devices. (2018). doi:10.1109/TED.2018.2859180.

[30] J. Kim, C. Ko, A. Frenzel, S. Ramanathan, J.E. Hoffman, Nanoscale imaging and control of resistance switching in VO2 at room temperature, Appl. Phys. Lett. (2010). doi:10.1063/1.3435466.

[31] C. Wang, L. Zhao, Z. Liang, B. Dong, L. Wan, S. Wang, New intelligent multifunctional SiO2/VO2 composite films with enhanced infrared light regulation performance, solar modulation capability, and superhydrophobicity, Sci. Technol. Adv. Mater. (2017). doi:10.1080/14686996.2017.1360752.

[32] N.F. Mott, The transition to the metallic state, Philos. Mag. (1961). doi:10.1080/14786436108243318.

[33] A. Zylbersztejn, N.F. Mott, Metal-insulator transition in vanadium dioxide, Phys. Rev. B. 11 (1975) 4383–4395. doi:10.1103/PhysRevB.11.4383.

[34] J. Hubbard, Electron correlations in narrow energy bands III. An improved solution, Proc. R. Soc. London. Ser. A. Math. Phys. Sci. (1964). doi:10.1098/rspa.1964.0190.

[35] V. Eyert, The metal-insulator transitions of VO2: A band theoretical approach, Ann. Phys. 11 (2002) 650–704. doi:10.1002/1521-3889(200210)11:9<650::AID-ANDP650>3.0.CO;2-K.

[36] J.B. Goodenough, The two components of the crystallographic transition in VO2, J. Solid State Chem. (1971). doi:10.1016/0022-4596(71)90091-0.

[37] R. Peiersl, More Surprises in Theoretical Physics, Princeton University Press, 1992.

[38] C. Weber, D.D. O'Regan, N.D.M. Hine, M.C. Payne, G. Kotliar, P.B. Littlewood, Vanadium dioxide: A peierls-mott insulator stable against disorder, Phys. Rev. Lett. (2012). doi:10.1103/PhysRevLett.108.256402.

[39] L. Hoddeson, G. Baym, M. Eckert, The development of the quantum-mechanical electron theory of metals: 1928, Rev. Mod. Phys. (1987). doi:10.1103/RevModPhys.59.287.

[40] J.H. De Boer, E.J.W. Verwey, Semi-conductors with partially and with completely filled3d-lattice bands, Proc. Phys. Soc. (1937). doi:10.1088/0959-5309/49/4S/307.

[41] N.F. Mott, The basis of the electron theory of metals, with special reference to the transition metals, Proc. Phys. Soc. Sect. A. (1949). doi:10.1088/0370-1298/62/7/303.

[42] M. Imada, F. Atsushi, T. Yoshinori, Metal insulator transition, Rev. Mod. Phys. (1998).

[43] N.F. Mott, Metal-Insulator Transition, Rev. Mod. Phys. 40 (1968) 677–683. doi:10.1103/RevModPhys.40.677.

[44] G. Grüner, The dynamics of charge-density waves, Rev. Mod. Phys. (1988). doi:10.1103/RevModPhys.60.1129.

[45] P.W. Anderson, Absence of diffusion in certain random lattices, Phys. Rev. (1958). doi:10.1103/PhysRev.109.1492.

[46] A. Aspect, M. Inguscio, Anderson localization of ultracold atoms, Phys. Today. (2009). doi:10.1063/1.3206092.

[47] G. Roati, C. D'Errico, L. Fallani, M. Fattori, C. Fort, M. Zaccanti, G. Modugno, M. Modugno, M. Inguscio, Anderson localization of a non-interacting Bose-Einstein condensate, Nature. (2008). doi:10.1038/nature07071.

[48] D.B. Rogers, R.D. Shannon, A.W. Sleight, J.L. Gillson, Crystal chemistry of metal dioxides with rutile-related structures, Inorg. Chem. (1969). doi:10.1021/ic50074a029.

[49] S. Ramanathan, Thin film metal-oxides: Fundamentals and applications in electronics and energy, 2010. doi:10.1007/978-1-4419-0664-9.

[50] L. Pauling, The principles determining the structure of complex ionic crystals, J. Am. Chem. Soc. (1929). doi:10.1021/ja01379a006.

[51] Y. Wu, L. Fan, W. Huang, S. Chen, S. Chen, F. Chen, C. Zou, Z. Wu, Depressed transition temperature of W x V 1-x O 2 : Mechanistic insights from the X-ray absorption fine structure (XAFS) spectroscopy, Phys. Chem. Chem. Phys. (2014). doi:10.1039/c4cp01661k.

[52] J.M. Longo, P. Kierkegaard, C.J. Ballhausen, U. Ragnarsson, S.E. Rasmussen, E. Sunde, N.A. Sørensen, A Refinement of the Structure of VO2., Acta Chem. Scand. 24 (1970) 420–426. doi:10.3891/acta.chem.scand.24-0420.

[53] A. Moatti, R. Sachan, V.R. Cooper, J. Narayan, Electrical Transition in Isostructural VO 2 Thin-Film Heterostructures, Sci. Rep. (2019). doi:10.1038/s41598-019-39529-z.

[54] M. Yang, Y. Yang, B. Hong, L. Wang, K. Hu, Y. Dong, H. Xu, H. Huang, J. Zhao, H. Chen, L. Song, H. Ju, J. Zhu, J. Bao, X. Li, Y. Gu, T. Yang, X. Gao, Z. Luo, C. Gao, Suppression of Structural Phase Transition in VO 2 by Epitaxial Strain in Vicinity of Metal-insulator Transition, Sci. Rep. (2016). doi:10.1038/srep23119.

[55] E. Arcangeletti, L. Baldassarre, D. Di Castro, S. Lupi, L. Malavasi, C. Marini, A. Perucchi, P. Postorino, Evidence of a pessure-induced metallization process in monoclinic VO2, Phys. Rev. Lett. 98 (2007). doi:10.1103/PhysRevLett.98.196406.

[56] D. Lee, B. Chung, Y. Shi, G.Y. Kim, N. Campbell, F. Xue, K. Song, S.Y. Choi, J.P. Podkaminer, T.H. Kim, P.J. Ryan, J.W. Kim, T.R. Paudel, J.H. Kang, J.W. Spinuzzi, D.A. Tenne, E.Y. Tsymbal, M.S. Rzchowski, L.Q. Chen, J. Lee, C.B. Eom, Isostructural metal-insulator transition in VO 2, Science (80-.). (2018). doi:10.1126/science.aam9189.

[57] J.M. Atkin, S. Berweger, E.K. Chavez, M.B. Raschke, J. Cao, W. Fan, J. Wu, Strain and temperature dependence of the insulating phases of VO 2 near the metal-insulator transition, Phys. Rev. B - Condens. Matter Mater. Phys. 85 (2012) 020101. doi:10.1103/PhysRevB.85.020101.

[58] H. Bethe, Termaufspaltung in Kristallen (Splitting of terms in crystals. Complete English translation), Ann. Phys. (1929). doi:https://doi.org/10.1142/9789812795755_0001.

[59] J.H. Van Vleck, Theory of the variations in paramagnetic anisotropy among different salts of the iron group, Phys. Rev. (1932). doi:10.1103/PhysRev.41.208.

[60] B.J. S Griffith, L.E. Orgel, Ligand-Field Theory, Q. Rev. 11 (1957) 381–393. doi:10.1039/QR9571100381.

[61] S. Lee, T.L. Meyer, C. Sohn, D. Lee, J. Nichols, D. Lee, S.S.A. Seo, J.W. Freeland, T.W. Noh, H.N. Lee, Electronic structure and insulating gap in epitaxial VO 2 polymorphs, APL Mater. 3 (2015) 126109. doi:10.1063/1.4939004.

[62] N.B. Aetukuri, A.X. Gray, M. Drouard, M. Cossale, L. Gao, A.H. Reid, R. Kukreja, H. Ohldag, C.A. Jenkins, E. Arenholz, K.P. Roche, H.A. Dürr, M.G. Samant, S.S.P. Parkin, Control of the metal-insulator transition in vanadium dioxide by modifying orbital occupancy, Nat. Phys. (2013). doi:10.1038/nphys2733.

[63] J. Narayan, V.M. Bhosle, Phase transition and critical issues in structure-property correlations of vanadium oxide, J. Appl. Phys. (2006). doi:10.1063/1.2384798.

[64] L.L. Fan, S. Chen, Z.L. Luo, Q.H. Liu, Y.F. Wu, L. Song, D.X. Ji, P. Wang, W.S. Chu, C. Gao, C.W. Zou, Z.Y. Wu, Strain dynamics of ultrathin VO2 film grown on TiO2 (001) and the

associated phase transition modulation, Nano Lett. (2014). doi:10.1021/nl501480f.

[65] L.L. Fan, S. Chen, Y.F. Wu, F.H. Chen, W.S. Chu, X. Chen, C.W. Zou, Z.Y. Wu, Growth and phase transition characteristics of pure M-phase VO 2 epitaxial film prepared by oxide molecular beam epitaxy, Appl. Phys. Lett. (2013). doi:10.1063/1.4823511.

[66] D.G. Schlom, Perspective: Oxide molecular-beam epitaxy rocks!, APL Mater. (2015). doi:10.1063/1.4919763.

[67] A.Y. Cho, J.R. Arthur, Molecular beam epitaxy, Prog. Solid State Chem. 10 (1975) 157–191. doi:10.1016/0079-6786(75)90005-9.

[68] A.Y. Cho, How molecular beam epitaxy (MBE) began and its projection into the future, J. Cryst. Growth. (1999). doi:10.1016/S0022-0248(98)01265-2.

[69] L. Xu, H.W. Liang, Y. Yang, S.H. Yu, Stability and Reactivity: Positive and Negative Aspects for Nanoparticle Processing, Chem. Rev. (2018). doi:10.1021/acs.chemrev.7b00208.

[70] B. von Issendorff, O. Cheshnovsky, Metal To Insulator Transitions in Clusters, Annu. Rev. Phys. Chem. 56 (2005) 549–580. doi:10.1146/annurev.physchem.54.011002.103845.

[71] F. Baletto, Structural properties of sub-nanometer metallic clusters, J. Phys. Condens. Matter. (2019). doi:10.1088/1361-648X/aaf989.

[72] C. Vázquez-Vázquez, M.A. López-Quintela, M.C. Buján-Núñez, J. Rivas, Finite size and surface effects on the magnetic properties of cobalt ferrite nanoparticles, J. Nanoparticle Res. (2011). doi:10.1007/s11051-010-9920-7.

[73] P. Shvets, O. Dikaya, K. Maksimova, A. Goikhman, A review of Raman spectroscopy of vanadium oxides, J. Raman Spectrosc. 50 (2019) 1226–1244. doi:10.1002/jrs.5616.

[74] K. Wegner, P. Piseri, H.V. Tafreshi, P. Milani, Cluster beam deposition: A tool for nanoscale science and technology, J. Phys. D. Appl. Phys. 39 (2006). doi:10.1088/0022-3727/39/22/R02.

[75] P. Milani; S. Iannotta, Cluster Beam Synthesis of Nanostructured Materials, Springer Science & Business Media, 2012.

[76] G. Scoles, Atomic and Molecular Beam Methods, Oxford University Press, 1988.

[77] P. Piseri, H.V. Tafreshi, P. Milani, Manipulation of nanoparticles in supersonic beams for the production of nanostructured materials, Curr. Opin. Solid State Mater. Sci. 8 (2004) 195–202. doi:10.1016/j.cossms.2004.08.002.

[78] E. Barborini, P. Piseri, P. Milani, Pulsed microplasma source of high intensity supersonic carbon cluster beams, J. Phys. D. Appl. Phys. (1999). doi:10.1088/0022-3727/32/21/102.

[79] T. Mazza, E. Barborini, P. Piseri, P. Milani, D. Cattaneo, A. Li Bassi, C.E. Bottani, C. Ducati, Raman spectroscopy characterization of Ti O2 rutile nanocrystals, Phys. Rev. B - Condens. Matter Mater. Phys. (2007). doi:10.1103/PhysRevB.75.045416.

[80] I.N. Kholmanov, E. Barborini, S. Vinati, P. Piseri, A. Podestà, C. Ducati, C. Lenardi, P. Milani, The influence of the precursor clusters on the structural and morphological evolution of nanostructured TiO 2 under thermal annealing, Nanotechnology. 14 (2003) 1168–1173. doi:10.1088/0957-4484/14/11/002.

[81] T. Caruso, C. Lenardi, R.G. Agostino, M. Amati, G. Bongiorno, T. Mazza, A. Policicchio, V. Formoso, E. MacCallini, E. Colavita, G. Chiarello, P. Finetti, F. Šutara, T. Skála, P. Piseri, K.C. Prince, P. Milani, Electronic structure of cluster assembled nanostructured Ti O2 by

resonant photoemission at the Ti L2,3 edge, J. Chem. Phys. (2008). doi:10.1063/1.2832321.

[82] T. Mazza, M. Devetta, P. Milani, G. Bongiorno, M. Coreno, P. Piseri, Accessing the fractal dimension of free clusters in supersonic beams, New J. Phys. (2011). doi:10.1088/1367-2630/13/2/023009.

[83] P. Piseri, T. Mazza, G. Bongiorno, C. Lenardi, L. Ravagnan, F. Della Foglia, F. DiFonzo, M. Coreno, M. DeSimone, K.C. Prince, P. Milani, Core level spectroscopy of free titanium clusters in supersonic beams, New J. Phys. (2006). doi:10.1088/1367-2630/8/8/136.

[84] P. Piseri, A. Podestà, E. Barborini, P. Milani, Production and characterization of highly intense and collimated cluster beams by inertial focusing in supersonic expansions, Rev. Sci. Instrum. (2001). doi:10.1063/1.1361082.

[85] E. Clouet, Modeling of Nucleation Processes, in: Fundam. Model. Met. Process., 2018. doi:10.31399/asm.hb.v22a.a0005410.

[86] D.T. Wu, L. Gránásy, F. Spaepen, Nucleation and the solid-liquid interfacial free energy, MRS Bull. (2004). doi:10.1557/mrs2004.265.

[87] E.E. Finney, R.G. Finke, Nanocluster nucleation and growth kinetic and mechanistic studies: A review emphasizing transition-metal nanoclusters, J. Colloid Interface Sci. (2008). doi:10.1016/j.jcis.2007.05.092.

[88] H. Haberland, Clusters of atoms and molecules, Springer-Verlag Berlin Heidelberg, 1994. doi:10.1007/978-3-642-84329-7.

[89] B.K. Rao, B.M. Smirnov, Kinetics of clusterization in expanding vapor, Phys. Scr. (1997). doi:10.1088/0031-8949/56/5/007.

[90] E.H.A. Granneman, Ionized-cluster beam deposition and epitaxy, Microelectron. Eng. 10 (1990) 153–154. doi:10.1016/0167-9317(90)90006-F.

[91] H. Haberland, Z. Insepov, M. Moseler, Molecular-dynamics simulation of thin-film growth by energetic cluster impact, Phys. Rev. B. 51 (1995) 11061–11067. doi:10.1103/PhysRevB.51.11061.

[92] L. Bardotti, B. Prével, P. Mélinon, A. Perez, Q. Hou, M. Hou, Deposition of clusters on Au(111) surfaces. II. Experimental results and comparison with simulations, Phys. Rev. B. 62 (2000) 2835–2842. doi:10.1103/PhysRevB.62.2835.

[93] W. Bouwen, E. Kunnen, K. Temst, P. Thoen, M.J. Van Bael, F. Vanhoutte, H. Weidele, P. Lievens, R.E. Silverans, Characterization of granular Ag films grown by low-energy cluster beam deposition, Thin Solid Films. 354 (1999) 87–92. doi:10.1016/S0040-6090(99)00571-4.

[94] T. Mazza, E. Barborini, I.N. Kholmanov, P. Piseri, G. Bongiorno, S. Vinati, P. Milani, C. Ducati, D. Cattaneo, A. Li Bassi, C.E. Bottani, A.M. Taurino, P. Siciliano, Libraries of cluster-assembled titania films for chemical sensing, Appl. Phys. Lett. (2005). doi:10.1063/1.2035874.

[95] E. Barborini, C. Ducati, M. Leccardi, G. Bertolini, P. Repetto, P. Milani, Nanostructured refractory metal oxide films produced by a pulsed microplasma cluster source as active layers in microfabricated gas sensors, in: Jpn. J. Appl. Phys., 2011. doi:10.1143/JJAP.50.01AK01.

[96] M. de Simone, E. Snidero, M. Coreno, G. Bongiorno, L. Giorgetti, M. Amati, C. Cepek,

Oxidation of nanostructured Ti films produced by low energy cluster beam deposition: An X-ray Photoelectron Spectroscopy characterization, Thin Solid Films. 520 (2012) 4803–4807. doi:10.1016/j.tsf.2011.10.075.

[97] G. Silversmit, D. Depla, H. Poelman, G.B. Marin, R. De Gryse, Determination of the V2p XPS binding energies for different vanadium oxidation states (V5+ to V0+), J. Electron Spectros. Relat. Phenomena. 135 (2004) 167–175. doi:10.1016/j.elspec.2004.03.004.

[98] M. Schmid, H.P. Steinrück, J.M. Gottfried, A new asymmetric Pseudo-Voigt function for more efficient fitting of XPS lines, Surf. Interface Anal. 46 (2014) 505–511. doi:10.1002/sia.5521.

[99] D.A. Davydov, A.I. Gusev, Ordered monoclinic vanadium suboxide V14O6, Phys. Solid State. 51 (2009) 156–164. doi:10.1134/s106378340901020x.

[100] K. Hiraga, M. Hirabayashi, Crystal structure of vanadium suboxide V2O1±x, J. Solid State Chem. 14 (1975) 219–228. doi:10.1016/0022-4596(75)90026-2.

[101] P. Pervan, T. Valla, M. Milun, Vanadium CVV Auger transition, Solid State Commun. 99 (1996) 393–397. doi:10.1016/0038-1098(96)00277-3.

[102] F.J. Szalkowski, G.A. Somorjai, Auger electron spectroscopic investigations of chemical shifts in some vanadium compounds, J. Chem. Phys. 61 (1974) 2064–2070. doi:10.1063/1.1682213.

[103] F.J. Szalkowski, G.A. Somorjai, Auger electron spectroscopy investigations of the surface chemical composition of vanadium, the vanadium oxides, and oxidized vanadium: Chemical shift and peak intensity analysis, J. Chem. Phys. 56 (1972) 6097–6103. doi:10.1063/1.1677160.

[104] G.A. Sawatzky, D. Post, X-ray photoelectron and Auger spectroscopy study of some vanadium oxides, Phys. Rev. B. 20 (1979) 1546–1555. doi:10.1103/PhysRevB.20.1546.

[105] R. Zimmermann, R. Claessen, F. Reinert, T. Pillo, R. Zimmermann, P. Steiner, N. Mannella, Electronic structure of 3d-transition-metal oxides: on-site Coulomb repulsion versus covalency, J. Physics-Condensed Matter. 11 (1999) 1657–1682. doi:10.1080/13602381.2016.1168624.

[106] Q.H. Wu, A. Thissen, W. Jaegermann, M. Schüz, P.C. Schmidt, Resonant photoemission spectroscopy study of electronic structure of V 2 O 5, Chem. Phys. Lett. 430 (2006) 309–313. doi:10.1016/j.cplett.2006.08.071.

[107] R. Zimmermann, R. Claessen, F. Reinert, P. Steiner, S. Hüfner, Strong hybridization in vanadium oxides: Evidence from photoemission and absorption spectroscopy, J. Phys. Condens. Matter. 10 (1998) 5697–5716. doi:10.1088/0953-8984/10/25/018.

[108] E. Papalazarou, M. Gatti, M. Marsi, V. Brouet, F. Iori, L. Reining, E. Annese, I. Vobornik, F. Offi, A. Fondacaro, S. Huotari, P. Lacovig, O. Tjernberg, N.B. Brookes, M. Sacchi, P. Metcalf, G. Panaccione, Valence-band electronic structure of V2 O3: Identification of v and O bands, Phys. Rev. B. 80 (2009) 1–6. doi:10.1103/PhysRevB.80.155115.

[109] T.E. Norwood, J.L. Fry, Energy Bands of VO, Phys. Rev. B. 2 (1970) 472–481. doi:10.1103/PhysRevB.2.472.

[110] S. Tewari, Electronic band structure of VO by the augmented-plane-wave method, Solid State Commun. 11 (1972) 1139–1142. doi:10.1016/0038-1098(72)90810-1.

[111] D.J. Kraan, The band structure of VO by the APW-LCAO method, Solid State Commun. 15

(1974) 991–995. doi:10.1016/0038-1098(74)90516-X.

[112] M.T. Greiner, Z.H. Lu, Thin-film metal oxides in organic semiconductor devices: Their electronic structures, work functions and interfaces, NPG Asia Mater. 5 (2013) e55-16. doi:10.1038/am.2013.29.

[113] R. Zimmermann, R. Claessen, F. Reinert, P. Steiner, S. Hüfner, Strong hybridization in vanadium oxides: evidence from photoemission and absorption spectroscopy, J. Phys. Condens. Matter. 10 (1998) 5697–5716. doi:10.1088/0953-8984/10/25/018.

[114] S. Shin, S. Suga, M. Taniguchi, M. Fujisawa, H. Kanzaki, A. Fujimori, H. Daimon, Y. Ueda, K. Kosuge, S. Kachi, Vacuum-ultraviolet reflectance and photoemission study of the metal-insulator phase transitions in VO2, V6O13, and V2O3, Phys. Rev. B. 41 (1990) 4993–5009.

[115] M. Gupta, D.E. Ellis, Cluster model for lattice distortion effects on electronic structure: VO and VO2, Phys. Rev. B. 13 (1976) 3405–3418.

[116] U. Gelius, K. Siegbahn, ESCA studies of molecular core and valence levels in the gas phase, Gen. Discuss. Faraday Soc. 54 (1972) 257–268. doi:10.1039/DC9725400257.

[117] D. Briggs, Handbook of X-ray Photoelectron Spectroscopy C. D. Wanger, W. M. Riggs, L. E. Davis, J. F. Moulder and G. E.Muilenberg Perkin-Elmer Corp., Physical Electronics Division, Eden Prairie, Minnesota, USA, 1979. 190 pp. $195, Surf. Interface Anal. 3 (1981) v–v. doi:10.1002/sia.740030412.

[118] S. Macis, C. Aramo, C. Bonavolontà, G. Cibin, A. D'Elia, I. Davoli, M. De Lucia, M. Lucci, S. Lupi, M. Miliucci, A. Notargiacomo, C. Ottaviani, C. Quaresima, M. Scarselli, J. Scifo, M. Valentino, P. De Padova, A. Marcelli, MoO 3 films grown on polycrystalline Cu: Morphological, structural, and electronic properties , J. Vac. Sci. Technol. A. 37 (2019) 021513. doi:10.1116/1.5078794.

[119] Q.H. Wu, A. Thissen, W. Jaegermann, M. Liu, Photoelectron spectroscopy study of oxygen vacancy on vanadium oxides surface, Appl. Surf. Sci. 236 (2004) 473–478. doi:10.1016/j.apsusc.2004.05.112.

[120] R. Wang, T. Katase, K.K. Fu, T. Zhai, J. Yang, Q. Wang, H. Ohta, N. Koch, S. Duhm, Oxygen Vacancies Allow Tuning the Work Function of Vanadium Dioxide, Adv. Mater. Interfaces. 5 (2018) 1–7. doi:10.1002/admi.201801033.

[121] C. Ko, Z. Yang, S. Ramanathan, Work Function of Vanadium Dioxide Thin Films Across the Metal-Insulator Transition and the Role of Surface Nonstoichiometry, ACS Appl. Mater. Interfaces. 3 (2011) 3396–3401. doi:10.1021/am2006299.

[122] C. Leung, L. Kao, S. Su, J. Feng, T. Chan, Relationship between surface dipole, work function and charge transfer: Some exceptions to an established rule, Phys. Rev. B - Condens. Matter Mater. Phys. 68 (2003) 1–6. doi:10.1103/PhysRevB.68.195408.

[123] M. Stössel, J. Staudigel, F. Steuber, J. Simmerer, A. Winnacker, Impact ofthe cathode metal work function on the performance of vacuum-deposited organic light emitting-devices, Appl. Phys. A. 390 (1999) 387–390. doi:10.1007/s003399900011.

[124] D.M. Wood, Classical size dependence of the work function of small metallic spheres, Phys. Rev. Lett. 46 (1981) 749. doi:10.1103/PhysRevLett.46.749.

[125] M. Seidl, K.H. Meiwes-Broer, M. Brack, Finite-size effects in ionization potentials and electron affinities of metal clusters, J. Chem. Phys. 95 (1991) 1295–1303.

doi:10.1063/1.461111.

[126] A. Schmidt-Ott, P. Schurtenberger, H.C. Siegmann, Enormous yield of photoelectrons from small particles, Phys. Rev. Lett. 45 (1980) 1284–1287. doi:10.1103/PhysRevLett.45.1284.

[127] L. Zhou, M.R. Zachariah, Size resolved particle work function measurement of free nanoparticles: Aggregates vs. spheres, Chem. Phys. Lett. 525–526 (2012) 77–81. doi:10.1016/j.cplett.2011.11.045.

[128] F. Borghi, A. Podestà, C. Piazzoni, P. Milani, Growth Mechanism of Cluster-Assembled Surfaces: From Submonolayer to Thin-Film Regime, Phys. Rev. Appl. 9 (2018) 044016. doi:10.1103/PhysRevApplied.9.044016.

[129] W.E. Ford, D. Gao, N. Knorr, R. Wirtz, F. Scholz, Z. Karipidou, K. Ogasawara, S. Rosselli, V. Rodin, G. Nelles, F. Von Wrochem, Organic dipole layers for ultralow work function electrodes, ACS Nano. (2014). doi:10.1021/nn502794z.

[130] A. Marcelli, M.I. Mazuritskiy, S.B. Dabagov, D. Hampai, A.M. Lerer, E.A. Izotova, A. D'Elia, S. Turchini, N. Zema, F. Zuccaro, M. de Simone, S.J. Rezvani, M. Coreno, A new XUV optical end-station to characterize compact and flexible photonic devices using synchrotron radiation, J. Instrum. 13 (2018) C03035–C03035. doi:10.1088/1748-0221/13/03/C03035.

[131] J.G. Chen, C.M. Kirn, B. Frühberger, B.D. DeVries, M.S. Touvelle, A NEXAFS determination of the oxidation state of vanadium carbide on V(110): observation of charge transfer from vanadium to carbon, Surf. Sci. 321 (1994) 145–155. doi:10.1016/0039-6028(94)90035-3.

[132] J.G. Chen, NEXAFS investigations of transition metal oxides, nitrides, carbides, sulfides and other interstitial compounds, Surf. Sci. Rep. 30 (1997) 1–152. doi:10.1016/S0167-5729(97)00011-3.

[133] F.M.F. De Groot, M. Grioni, J.C. Fuggle, J. Ghijsen, G.A. Sawatzky, H. Petersen, Oxygen 1s X-ray-absorption edges of transition-metal oxides, Phys. Rev. B. 40 (1989) 5715–5723. doi:10.1103/PhysRevB.40.5715.

[134] K. Hermann, M. Witko, Theory of physical and chemical behavior of transition metal oxides: vanadium and molybdenum oxides, in: Chem. Phys. Solid Surfaces, 2001: pp. 136–198. doi:10.1016/S1571-0785(01)80024-9.

[135] D. Ruzmetov, S.D. Senanayake, S. Ramanathan, X-ray absorption spectroscopy of vanadium dioxide thin films across the phase-transition boundary, Phys. Rev. B - Condens. Matter Mater. Phys. (2007). doi:10.1103/PhysRevB.75.195102.

[136] S. Kasatikov, E. Filatova, S. Sakhonenkov, A. Konashuk, A. Makarova, Relationship between Ta Oxidation State and Its Local Atomic Coordination Symmetry in a Wide Range of Oxygen Nonstoichiometry Extent of TaO x, J. Phys. Chem. C. 123 (2019) 6849–6860. doi:10.1021/acs.jpcc.8b12053.

[137] J. Zaanen, G.A. Sawatzky, J. Fink, W. Speier, J.C. Fuggle, L2,3 absorption spectra of the lighter 3d transition metals, Phys. Rev. B. 32 (1985) 4905–4913. doi:10.1103/PhysRevB.32.4905.

[138] J.T. Lau, J. Rittmann, V. Zamudio-Bayer, M. Vogel, K. Hirsch, P. Klar, F. Lofink, T. Möller, B. V. Issendorff, Size dependence of L2,3 branching ratio and 2p core-hole screening in X-ray absorption of metal clusters, Phys. Rev. Lett. 101 (2008). doi:10.1103/PhysRevLett.101.153401.

[139] O. Bunău, Y. Joly, Time-dependent density functional theory applied to x-ray absorption spectroscopy, Phys. Rev. B - Condens. Matter Mater. Phys. 85 (2012). doi:10.1103/PhysRevB.85.155121.

[140] L. Floreano, G. Naletto, D. Cvetko, R. Gotter, M. Malvezzi, L. Marassi, A. Morgante, A. Santaniello, A. Verdini, F. Tommasini, G. Tondello, Performance of the grating-crystal monochromator of the ALOISA beamline at the Elettra Synchrotron, Rev. Sci. Instrum. (1999). doi:10.1063/1.1150001.

[141] R.Z. Bachrach, Synchrotron Radiation Research Advances in Surface and Interface Science, Springer US, Boston, MA, 1992. doi:10.1007/978-1-4615-3278-1.

[142] A. Marcelli, M. Coreno, M. Stredansky, W. Xu, C. Zou, L. Fan, W. Chu, S. Wei, A. Cossaro, A. Ricci, A. Bianconi, A. D'Elia, Nanoscale Phase Separation and Lattice Complexity in VO2: The Metal–Insulator Transition Investigated by XANES via Auger Electron Yield at the Vanadium L23-Edge and Resonant Photoemission, Condens. Matter. 2 (2017). doi:10.3390/condmat2040038.

[143] M. Abbate, F.M.F. De Groot, J.C. Fuggle, Y.J. Ma, C.T. Chen, F. Sette, A. Fujimori, Y. Ueda, K. Kosuge, Soft-x-ray-absorption studies of the electronic-structure changes through the VO2 phase transition, Phys. Rev. B. (1991). doi:10.1103/PhysRevB.43.7263.

[144] N.F. Quackenbush, J.W. Tashman, J.A. Mundy, S. Sallis, H. Paik, R. Misra, J.A. Moyer, J.H. Guo, D.A. Fischer, J.C. Woicik, D.A. Muller, D.G. Schlom, L.F.J. Piper, Nature of the metal insulator transition in ultrathin epitaxial vanadium dioxide, Nano Lett. (2013). doi:10.1021/nl402716d.

[145] M. Wu, J.C. Zheng, H.Q. Wang, Investigation of the vanadium L23 -edge x-ray absorption spectrum of SrVO3 using configuration interaction calculations: Multiplet, valence, and crystal-field effects, Phys. Rev. B. (2018). doi:10.1103/PhysRevB.97.245138.

[146] S.H. Lee, H.M. Cheong, M. Je Seong, P. Liu, C.E. Tracy, A. Mascarenhas, J.R. Pitts, S.K. Deb, Microstructure study of amorphous vanadium oxide thin films using raman spectroscopy, J. Appl. Phys. (2002). doi:10.1063/1.1495074.

[147] D.H. Jung, H.S. So, J.S. Ahn, H. Lee, T.T.T. Nguyen, S. Yoon, S.Y. Kim, H.-Y. Jung, Low temperature growth of amorphous VO 2 films on flexible polyimide substrates with a TiO 2 buffer layer , J. Vac. Sci. Technol. A Vacuum, Surfaces, Film. (2018). doi:10.1116/1.5019388.

[148] F.M.F. de Groot, Differences between L3 and L2 X-ray absorption spectra, Phys. B Phys. Condens. Matter. (1995). doi:10.1016/0921-4526(94)00817-F.

[149] J. Zaanen, G.A. Sawatzky, J. Fink, W. Speier, J.C. Fuggle, L2,3 absorption spectra of the lighter 3d transition metals, Phys. Rev. B. (1985). doi:10.1103/PhysRevB.32.4905.

[150] M.W. Haverkort, Z. Hu, A. Tanaka, W. Reichelt, S. V. Streltsov, M.A. Korotin, V.I. Anisimov, H.H. Hsieh, H.J. Lin, C.T. Chen, D.I. Khomskii, L.H. Tjeng, Orbital-assisted metal-insulator transition in VO2, Phys. Rev. Lett. (2005). doi:10.1103/PhysRevLett.95.196404.

[151] V. Ilakovac, M. Kralj, P. Pervan, M.C. Richter, A. Goldoni, R. Larciprete, L. Petaccia, K. Hricovini, Final-state screening dynamics in resonant Auger decay at the 2p edge of vanadium, Phys. Rev. B - Condens. Matter Mater. Phys. 71 (2005) 1–6. doi:10.1103/PhysRevB.71.085413.

[152] M. Demeter, M. Neumann, W. Reichelt, Mixed-valence vanadium oxides studied by XPS, Surf. Sci. 454–456 (2000) 41–44. doi:10.1016/S0039-6028(00)00111-4.

[153] R. Eguchi, M. Taguchi, M. Matsunami, K. Horiba, K. Yamamoto, Y. Ishida, A. Chainani, Y. Takata, M. Yabashi, D. Miwa, Y. Nishino, K. Tamasaku, T. Ishikawa, Y. Senba, H. Ohashi, Y. Muraoka, Z. Hiroi, S. Shin, Photoemission evidence for a Mott-Hubbard metal-insulator transition in VO2, Phys. Rev. B - Condens. Matter Mater. Phys. (2008). doi:10.1103/PhysRevB.78.075115.

[154] A. Fujimori, I. Hase, H. Namatame, Y. Fujishima, Y. Tokura, H. Eisaki, S. Uchida, K. Takegahara, F.M.F. De Groot, Evolution of the spectral function in Mott-Hubbard systems with d1 configuration, Phys. Rev. Lett. (1992). doi:10.1103/PhysRevLett.69.1796.

[155] S. Suga, A. Sekiyama, S. Imada, T. Miyamachi, H. Fujiwara, A. Yamasaki, K. Yoshimura, K. Okada, M. Yabashi, K. Tamasaku, A. Higashiya, T. Ishikawa, ∼8 keV photoemission of the metal-insulator transition system VO 2, New J. Phys. (2009). doi:10.1088/1367-2630/11/10/103015.

[156] T. Valla, P.D. Johnson, Z. Yusof, B. Wells, Q. Li, S.M. Loureiro, R.J. Cava, M. Mikami, Y. Mori, M. Yoshimura, T. Sasaki, Coherence-incoherence and dimensional crossover in layered strongly correlated metals, Nature. (2002). doi:10.1038/nature00774.

[157] K. Shimada, Y. Takeda, M. Arita, H. Sato, A. Kimura, H. Namatame, M. Taniguchi, M. Tsubota, K. Katoh, F. Iga, T. Takabatake, Temperature-dependent metal-insulator transition in d- and f-electron systems studied by high-resolution photoemission spectroscopy, J. Electron Spectros. Relat. Phenomena. (2001). doi:10.1016/S0368-2048(00)00319-4.

[158] R.J.O. Mossanek, M. Abbate, Cluster model calculations with nonlocal screening channels of metallic and insulating V O2, Phys. Rev. B - Condens. Matter Mater. Phys. (2006). doi:10.1103/PhysRevB.74.125112.

[159] P.A. Dowben, Metallicity of thin films and overlayers, Surf. Sci. Rep. (2000). doi:10.1016/S0167-5729(00)00010-8.

[160] D. McIlroy, C. Waldfried, J. Zhang, J.W. Choi, F. Foong, S. Liou, P. Dowben, Comparison of the temperature-dependent electronic structure of the perovskites), Phys. Rev. B - Condens. Matter Mater. Phys. (1996). doi:10.1103/PhysRevB.54.17438.

[161] D. Li, J. Zhang, S. Lee, P.A. Dowben, Evidence for the formation of metallic mercury overlayers on Si(111), Phys. Rev. B. (1992). doi:10.1103/PhysRevB.45.11876.

[162] Z. Yang, C. Ko, V. Balakrishnan, G. Gopalakrishnan, S. Ramanathan, Dielectric and carrier transport properties of vanadium dioxide thin films across the phase transition utilizing gated capacitor devices, Phys. Rev. B - Condens. Matter Mater. Phys. (2010). doi:10.1103/PhysRevB.82.205101.

[163] D. Fu, K. Liu, T. Tao, K. Lo, C. Cheng, B. Liu, R. Zhang, H.A. Bechtel, J. Wu, Comprehensive study of the metal-insulator transition in pulsed laser deposited epitaxial VO 2 thin films, J. Appl. Phys. (2013). doi:10.1063/1.4788804.

[164] M.M. Qazilbash, K.S. Burch, D. Whisler, D. Shrekenhamer, B.G. Chae, H.T. Kim, D.N. Basov, Correlated metallic state of vanadium dioxide, Phys. Rev. B - Condens. Matter Mater. Phys. (2006). doi:10.1103/PhysRevB.74.205118.

[165] E.I. Solomon, L. Basumallick, P. Chen, P. Kennepohl, Variable energy photoelectron spectroscopy: electronic structure and electronic relaxation, Coord. Chem. Rev. 249 (2005) 229–253. doi:10.1016/j.ccr.2004.02.016.

[166] G.J. Lapeyre, R.J. Smith, J. Knapp, J. Anderson, Constant Final Energy and Constant Initial

Energy Spectroscopy, Le J. Phys. Colloq. 39 (1978) C4-134-C4-141. doi:10.1051/jphyscol:1978417.

[167] F. De Groot, Multiplet effects in X-ray spectroscopy, Coord. Chem. Rev. 249 (2005) 31–63. doi:10.1016/j.ccr.2004.03.018.

[168] U. Becker, D.A. Shirley, VUV and Soft X-Ray Photoionization, Springer US, Boston, MA, MA, 1996. doi:10.1007/978-1-4613-0315-2.

[169] A. Bianconi, M. Dell'Ariccia, P.J. Durham, J.B. Pendry, Multiple-scattering resonances and structural effects in the x-ray-absorption near-edge spectra of Fe II and Fe III hexacyanide complexes, Phys. Rev. B. (1982). doi:10.1103/PhysRevB.26.6502.

[170] S. Stizza, G. Mancini, M. Benfatto, C.R. Natoli, J. Garcia, A. Bianconi, Structure of oriented V2O5 gel studied by polarized x-ray-absorption spectroscopy at the vanadium K edge, Phys. Rev. B. (1989). doi:10.1103/PhysRevB.40.12229.

[171] M. Abbate, J.B. Goedkoop, F.M.F. de Groot, M. Grioni, J.C. Fuggle, S. Hofmann, H. Petersen, M. Sacchi, Probing depth of soft x-ray absorption spectroscopy measured in total-electron-yield mode, Surf. Interface Anal. 18 (1992) 65–69. doi:10.1002/sia.740180111.

[172] A. Tanaka, T. Jo, Resonant 3 d , 3 p and 3 s Photoemission in Transition Metal Oxides Predicted at 2 p Threshold, J. Phys. Soc. Japan. 63 (1994) 2788–2807. doi:10.1143/JPSJ.63.2788.

Ringraziamenti

Questa tesi di dottorato è il risultato di un lavoro durato tre anni che ha coinvolto molte persone e faccio un anticipato mea-culpa in caso abbia dimenticato qualcuno. Chi mi conosce sa che non amo condividere pubblicamente ciò che provo, quindi non andrò oltre la punta dell'iceberg.

Vorrei ringraziare il Fondo Sociale Europeo e l'Istituto Officina dei Materiali (IOM-CNR) per aver co-finanziato la mia borsa di dottorato e l'Università di Trieste per avermi accettato come dottorando.

Marcello, per la quantità (non numerabile) di cose che ho imparato da te in questi tre anni, per la passione che metti nel tuo lavoro la quale inevitabilmente viene trasmessa a chi ti circonda, per le risate, le discussioni, le prese in giro, per aver indicato senza mai obbligare, ma soprattutto per l'umanità con cui hai interpretato il ruolo di Supervisore, Grazie.

Prof. Alberto Morgante per avermi accettato come suo dottorando e per la pazienza con cui ha firmato ogni modulo.

Claudio, Grazie per avermi fatto capire che è la passione che regola questo mestiere, per aver alimentato la mia naturale inclinazione allo studio della materia condensata e per i continui confronti.

Monica, per l'accoglienza, la disponibilità, i suggerimenti e le revisioni e per tutti i pranzi in famiglia a Lokev, Grazie.

Un Ringraziamento speciale lo dedico a Fabio, per essersi spinto ben oltre i confini del suo ruolo, per la professionalità, per la pazienza, le battute e le risate, i caffè, la pazienza (si due volte, perché ne hai avuta tanta con me), l'amicizia, per tutte le flange strette e gli Swagelok serrati e per aver *sempre* teso la mano nel momento del bisogno.

Luca, per quella prima pizza, per aver condiviso con me gioie e frustrazioni, per tutte quelle foto di prime pagine, per le serate improvvisate e per quelle programmate, per aver contribuito a farmi sopportare i marciapiedi stretti, Grazie.

Un ringraziamento sincero va ad Alessandra, per tutti gli aperitivi, le discussioni filosofiche, le risate, il sostegno e tanto altro che non scriverò qui.

Grazie Valeria, per aver letto e corretto questa tesi, per esserci sempre stata per un consiglio, per un confronto e per un conforto e per tutte le serate passate insieme.

A tutti i miei amici "triestini".

Grazie Cesare e Michele per essere stati come fratelli maggiori per me, per tutte le serate, per i caffè scroccati e per avermi sempre fatto sentire con le spalle coperte. Michele, anche se ormai hai fatto carriera per me resti sempre *il miglior post-doc del mondo*.

Ci tengo a ringraziare tutto lo staff di LDM e GasPhase per aver messo sempre a disposizione le loro risorse, in particolare Carlo per l'amicizia instauratasi in questi anni.

Vorrei ringraziare Paolo, durante i beamtime insieme ho imparato tanto.

Ringrazio Mauro, Gian, Andrea e Erika, per il continuo supporto emotivo, per l'amicizia e per le serate disagio. Un particolare Grazie va a Mauro per avermi spinto ad essere un Cacciatorpediniere e non una barchetta a vela.

A Lorenzo e Diletta per essermi stati vicini.

Mamma, per esserti sempre presa cura di me anche a distanza, perché conosci il mio essere orso, per le parmigine, per avermi sempre incoraggiato e appoggiato, Grazie. Senza di te non ce l'avrei fatta.

Papà, per esserci sempre stato e perché so che ci sarai in ogni circostanza, per le tue idee geniali, per i bei film, per avermi sempre sostenuto, Grazie. Senza di te non ce l'avrei fatta.

Ele, sono cambiate tante cose in questi tre anni, ma anche se moto distanti geograficamente ti ho sempre sentita molto vicina, per non avermi giudicato e per avermi fatto sentire il tuo affetto anche nei momenti peggiori, per Leo, Grazie. Senza di te non ce l'avrei fatta.

Spero di avervi resi orgogliosi di me.

Volutamente per ultima, ringrazio te Francesca (si uso il nome completo perché è un'occasione importante). Grazie per esserti presa cura di me in questo ultimo anno, per pareggiare il mio livello di scemenza, per i sogni condivisi e per la capacità di rendere tangibile un futuro che non vedo l'ora di vivere insieme.

È stato un piacere suonare con voi,

Ale